Design, Modeling, and Nonlinear Dynamics of a Cantilever Beam-Rigid Body Microgyroscope

by

Seyed Amir Mousavi Lajimi

A thesis
presented to the University of Waterloo
in fulfillment of the
thesis requirement for the degree of
Doctor of Philosophy
in
Systems Design Engineering

Waterloo, Ontario, Canada, 2013

I hereby declare that I am the sole author of this thesis. This is a true copy of the thesis, including any required final revisions, as accepted by my examiners.

I understand that my thesis may be made electronically available to the public.

Abstract

A new type of cantilever beam gyroscope is introduced, modeled, and analyzed. The main structure includes a cantilever beam and a rigid body attached to the free end of the beam. The model accounts for the eccentricity, that is the offset of the center of mass of the rigid body relative to the beam's free end. The first and second moments of mass and the rotary inertia appear in the equations of motion and boundary conditions. The common mechanism of electrostatic actuation of microgyroscopes is used with the difference of computing the force at the center of mass resulting in the electrostatic force and moment in the boundary conditions. By using the extended Hamilton's principle, the method of assumed modes, and Lagrange's differential equations, the equations of motion, boundary conditions, and the discretized model are developed. The generalized model simplifies to other beam gyroscope models by setting the required parameters to zero.

Considering the DC and AC components of the actuating and sensing methods, the response is resolved into the static and dynamic components. The static configuration is studied for an increasing DC voltage. For the uncoupled system of equations, the explicit equation relating the DC load and the static configuration is computed and solved for the static configuration of the beam-rigid body in each direction. Including the rotation rate, the stationary analysis is performed, the stationary pull-in voltage is identified, and it is shown that the angular rotation rate does not affect the static configuration. The modal frequencies of the beam-rigid body gyroscope are studied and the instability region due to the rotation rate is computed. It is shown that the gyroscope can operate in the frequency modulation mode and the amplitude modulation mode. To operate the beam-rigid body gyroscope in the frequency modulation mode, the closed-form relation of the observed modal frequency split and the input rotation rate is computed. The calibration curves are generated for a variety of DC loads. It is shown that the scale factor improves by matching the zero rotation rate natural frequencies.

The method of multiple scales is used to study the reduced-order nonlinear dynamics of the oscillations around the static equilibrium. The modulation equations, the "slow" system, are derived and solved for the steady-state solutions. The computational shooting method is employed to evaluate the results of the perturbation method. The frequency response and force response plots are generated. For combinations of parameters resulting in a single-valued response, the two methods are in excellent agreement. The synchronization of the response occurs in the sense direction for initially mismatched natural frequencies. The global stability of the system is studied by drawing phase-plane diagrams and long-time integration of response trajectories. The separatrices are computed, the jump phenomena is numerically shown, and the dynamic pull-in of the response is demonstrated. The fold bifurcation points are identified and it is shown that the response jumps to the higher/lower branch beyond the bifurcation points in forward/backward sweep of the amplitude and the excitation frequency of AC voltage.

The mechanical-thermal (thermomechanical) noise effect on the sense response is characterized by using a linear approximation of the system and the nonlinear "slow" system obtained by using the method of multiple scales. To perform linear analysis, the negligible effect of Coriolis force on the drive amplitude is discarded. The second-order drive resonator is solved for the drive amplitude

and phase. Finding the sense response due to the thermal noise force and the Coriolis force and equating them computes the mechanical-thermal noise equivalent rotation rate in terms of system parameters and mode shapes. The noise force is included in the third-order equation of the perturbation and equation to account for that in the reduced-order nonlinear response. The numerical results of linear and reduced-order nonlinear thermal noise analyses agree. It is shown that higher quality factor, higher AC voltage, and operating at lower DC points result in better resolution of the microsensor.

Acknowledgements

Without the support of my supervisor, Professor Glenn Heppler, this thesis would have not been concluded successfully. I would like to thank Glenn for providing me with the necessary support and guidance to complete this thesis. I would like to thank my co-supervisor Professor Eihab Abdel-Rahman for his valuable advice on some parts of the thesis. I would like to express my gratitude to both my supervisors. Last but not least, I would like to thank Lena for her companionship.

Dedication

This thesis is dedicated to my late grandmother, “maman-bozorg.” She was the one who loved me unconditionally.

Table of Contents

List of Tables

List of Figures

Chapter 1

Introduction

1.1 Motivation

Position and orientation sensing are essential parts of various engineering systems such as vehicles, satellites, and aircrafts to correct possible errors in the system output. To identify the position and the orientation in space, three displacement components along the three axes of the coordinate system (the linear displacements) and the three rotations about the same axes (the angular displacements) are characterized. Inertial sensors are used to estimate the components of the displacement vector and the components of rotation. Accelerometers (displacement sensors) and gyroscopes (rotation rate sensors) constitute the inertial sensors.

The applications of accelerometers and gyroscopes have a long history in the design and engineering of reliable products. A mechanical accelerometer was introduced by Lanchester in 1889 to measure the acceleration in road and railway vehicles [1]. In the 1850s, Foucault performed a demonstration using a gyroscope to observe the rotation of the Earth [2]. Smaller, cheaper, and more accurate inertial sensors have been developed since then. The first automotive rotation rate sensor was put into mass production by Robert Bosch GmbH in 1995 and used in the electronic stability program (ESP) [3].

The angular rate sensor (yaw rate sensor) of Robert Bosch GmbH was a mechanical sensor including a steel cylinder which was actuated and sensed piezoelectrically. With the advancement of micro and nanotechnologies, new generations of accelerometers and gyroscopes have increasingly found more applications in various industries. Micromachined inertial sensors, microaccelerometers and microgyroscopes, are currently extensively incorporated in cars to, for instance, active the safety system, in consumer products such as camcorders to stabilize the picture, and in biomedical applications to capture the body motion for medical purposes as well as many other applications [4].

Inertial sensors are self-contained units which measure the displacements and rotations, that is no external reference is used to estimate the motion [5]. The measured signal is proportional

to the acceleration, vibration, and shock in accelerometers [6]. The elementary structure of an accelerometer consists of a support frame, a suspended mass or beam, a spring and a damper. Depending on the measurement mechanisms, the displacement of the mass relative to the frame or a secondary effect such as stress in the deformed suspension beam is related to the acceleration or other desired parameters [7].

Accelerometers have been present in the market for more than three decades and used in high volumes for more than two decades [8]. Inertial sensors continue to shrink in size to satisfy the market's demands. Therefore, new designs and trends are expected to appear in the future. The new generation of inertial units combines several sensors including accelerometers and gyroscopes in one package. Automakers are expected to include the new generation of inertial units in all new cars. It is expected to see an increase in the global revenue of inertial units from $90 million in 2012 to $160 million in 2013 [8].

Gyroscopes, used as rotation rate sensors, are the second largest class of inertial sensors and expected to be incorporated in the unified inertial sensor packages. In the current market, miniature gyroscopes present a major growing sensor market with various applications from consumer electronics, and robotics to automotive and navigation systems [9]. To satisfy the resolution and performance requirements of different applications, gyroscopes' designs constantly evolve. Gyroscopes are classified based on the underlying method to estimate the angular rate of rotation. To this end, gyroscopes are commonly divided into spinning mass gyroscopes, vibrating gyroscopes, and optical gyroscopes [10].

The rotating body is a part of spinning mass gyroscopes and therefore requires bearings and other components which are hard to realize and very expensive to build. Miniaturizing such a complex structure requires sophisticated tools and methods. The research on this type of gyroscope is in an early stage and no gyroscope is commercially accessible [11]. The two main groups of optical gyroscopes are fiber-optic gyroscopes and ring-laser gyroscopes. The underlying working principle of all optical gyroscopes is the Sagnac effect which infers the rotation rate based on the phase difference of two counter-rotating light/laser beams. Optical gyroscopes have no moving parts, however they require external laser sources, complex set-up, and larger units to achieve higher performance.

Vibratory gyroscopes have no rotating parts, but employ the Coriolis force to couple two modes of vibration, the drive mode and the sense mode. The vibratory micromachined gyroscopes constitute the most of in-use gyroscopes [4]. In principle, a rotating object under transverse motion experiences the Coriolis acceleration in the perpendicular direction to the directions of the linear motion and the rotation axis. Therefore, the energy transfer is controlled by the angular rate of rotation and the drive mode vibration. The drive mode is commonly actuated at a constant amplitude and frequency and a feature of the sense mode such as amplitude or frequency, depending on the operation mode, is measured.

Designs of vibratory gyroscopes are constantly evolving to achieve better performance and reliability. In current designs various vibrating elements including beams, plates [12, 13], tuning forks [14, 15], and shells [16, 17] are used [18]. Variations of these structures are under investigation to

achieve a high performance and reliable design with lower cost. Vibrating beams relatively, have a simpler structure reducing the complexity of fabrication and thus the fabrication cost.

1.2 Beam Gyroscopes

The variations of the beam gyroscopes are shown in Figures 1.1(a)-1.1(c). The beam gyroscopes are divided into beam gyroscopes, beam-mass gyroscopes, and beam-rigid body gyroscopes. The beam gyroscope comprises a cantilever beam, the beam-mass gyroscope comprises a beam carrying an end mass, and the beam-rigid body gyroscope comprises a cantilever beam carrying a rigid body (the subject of this thesis). The research on the first two types of beam gyroscopes has been going for some time. However, beam-rigid body gyroscope has not been designed, modeled, and investigated in the scholarly literature.

In 1983, O'Connor and Shupe's patent was published on the first vibrating silicon beam gyroscope [19]. An electrostatic force near the fundamental natural frequency of the cantilever beam was used to excite the beam and a piezoresistive element was used to measure the vibration of the cantilever in the transverse direction. Maenaka et al. investigated a vibrating cantilever beam rotation rate sensor with square cross-section [20]. They used a piezo-actuator to excite the drive mode and controlled the drive amplitude by the capacitance change between the beam and the drive electrodes. The sense mode was detected by capacitance change between the beam and the bottom electrode. Maenaka et al. concluded that vibratory beam gyroscopes were more sensitive than other types of gyroscopes.

Seok and Scarton derived the mathematical model of the cantilever beam under distributed (along the length) electrostatic actuation [21] and studied the eigenvalues of the system. Their study of the effect of quality factor on the response agrees with the second-order system in that the higher the quality factor is, the higher the amplitude and the lower the bandwidth are. Although, Li et al. studied the beam-mass gyroscope experimentally, the mathematical model did not reflect the presence of the large end mass [22]. Their model used two classic mass-spring oscillators coupled through the Coriolis term in the sense direction.

An elementary beam-mass gyroscope model was presented by Esmaili et al. [23]. They considered an Euler-Bernoulli beam under elastic deformation due to electrostatic actuation and the rotation about the longitudinal direction. However, the description of the electrostatic force was not given and its effects on the response were neglected. Bhadbhade et al. [24] developed the coupled flexural-torsional equations of motion for beam-mass system. The gyroscopic term couples the flexural and torsional equations of motion and gives rise to the torsional deflection. The end mass was included to enhance the gyroscope performance by amplifying the gyroscopic effect [24].

Mojahedi et al. [25] extended the earlier model of the flexural-flexural vibration of a beam-mass gyroscope by including the geometric nonlinearity. To derive the equations of motion, they included the axial deformation and the in-extensibility condition. Although the static behaviour of the system was studied by Mojahedi et al., the dynamic behaviour was not investigated. The same model as [23], was used in [26] including an extra electrode in the sense direction. The structural

equations of [26] were not different from those used in the previous literature, however the physical dimensions of the numerical example were in the order of $1 - 100\,\mu$m.

Current models become less accurate when increasing the size of the end mass. Various studies on the flexural vibration of the cantilever beam carrying a large end mass, called a rigid body now and then, have shown the effects of the first and second moment of the mass, $M\,e$ and $M\,e^2$, and the rotary inertia of the rigid body on the natural frequencies of the beam-rigid body system [27, 28, 29, 30]. Preliminary studies on the beam-rigid body gyroscope have demonstrated that the equations of motion and therefore statics, dynamics, and the nonlinear dynamics of the beam-rigid body gyroscope are modified by the presence of a rigid body [31, 32].

1.3 Operating Modes of Vibratory Gyroscopes

There are three different methods of operation of vibratory gyroscopes to measure the input angular rate of rotation: the amplitude modulation based method, the frequency modulation based method, and the direct angle measurement based method. Conventionally, the amplitude of the secondary vibration, sense axis, is used to estimate the rotation rate. The rotation rate modulates the primary oscillation and the modulated signal excites the sense motion [33]. As a result, determining the amplitude of the sense signal computes the angular rate of rotation. To increase the sensitivity of the gyroscope, which is proportional to the ratio of the variation in the sense amplitude to the variation in the rotation rate, the natural frequencies of the drive and sense directions are matched; however, mode matching has undesirable effects such as lowering the bandwidth [33, 34].

Eigenvalues of the gyroscopic systems evolve with the rotation rate in the rotating frame [35, 36]. Consequently, the rotation rate measurement can be performed by measuring the modal frequency split in the sense direction [36, 37, 38, 39]. The advantages of measuring the input angular rate of rotation based on the frequency modulation method includes the unlimited bandwidth [40]. Zotov et al. [37, 38, 39] showed the experimental results of the application of the frequency modulation method on a silicon MEMS quadruple mass gyroscope (QMG) with ultrahigh quality factor. And, Kline et al. [40] performed the preliminary analysis of the ring gyroscope operated in the frequency modulation mode.

The third method to estimate the angular rate of rotation is to measure the inclination angle [41]. The instantaneous inclination angle is determined utilizing the proper relation between the angle and the read-out signals including the sense and drive displacements [41]. Direct measurement of the inclination angle has some benefits including an unrestricted bandwidth. The research on the application of the method is in progress. It was experimentally proved that various modes of operation can be combined to improve the performance for quadruple mass vibratory gyroscopes [42, 43].

1.4 Mechanical-Thermal Noise

The thermal equilibrium of a mechanical resonator with its environment at a certain absolute temperature T, requires the presence of a fluctuating force creating thermodynamic fluctuations in the

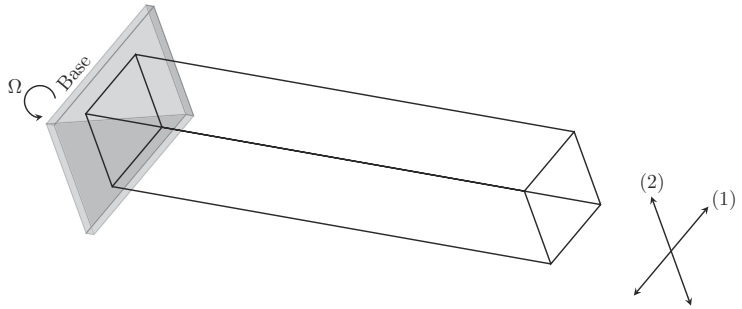

(a) Beam gyroscope

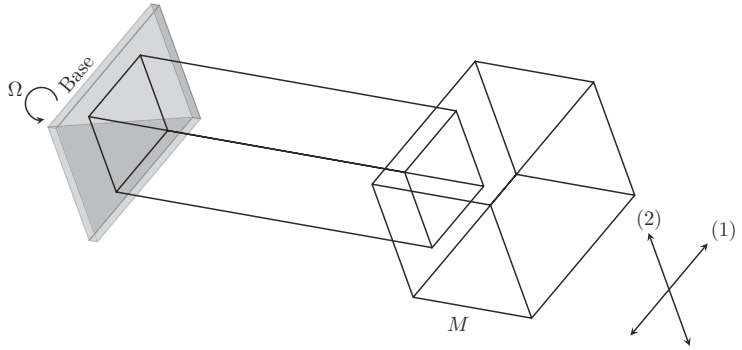

(b) Beam-mass gyroscope

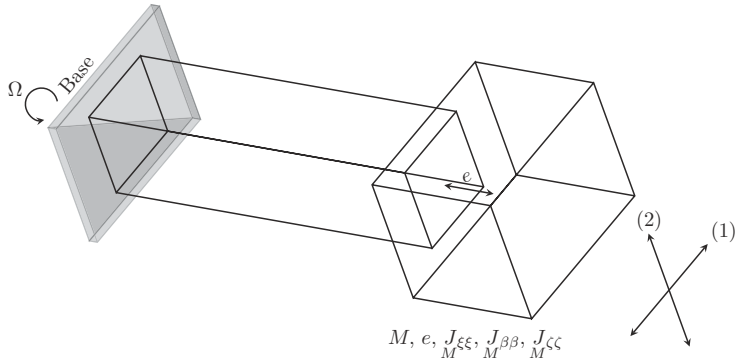

(c) Beam-rigid body gyroscope

Figure 1.1: The vibratory beam gyroscopes: (a) beam gyroscope, (b) beam-mass gyroscope, (c) beam-rigid body gyroscope. The primary oscillation is along direction (1) and the secondary Coriolis force induced motion is along direction (2). The figures are not drawn to scale.

motion of the oscillator [44]. The mechanical-thermal (thermomechanical) noise is caused by the molecular agitation through the structure and the Brownian motion where the molecules of the surrounding fluid interact with the structure [45]. Although other noise sources may surpass the

thermal noise in the macro-scale, for miniaturized sensors the mechanical-thermal noise reaches a higher noise floor and limits the sensitivity of the device [45, 46].

The mechanical-thermal noise for any mechanical resonator in thermal equilibrium with the surrounding fluid is studied by adding a root mean square (rms) force noise [45, 46, 47]

$$F_n = \sqrt{4\,k_B\,T\,c\,BW} \tag{1.1}$$

where k_B represents the Boltzman constant ($k_B = 1.38 \times 10^{-23}\,\mathrm{JK}^{-1}$, T the absolute temperature in Kelvin, c the damping coefficient in newton-seconds/meter, and BW the noise bandwidth defined by the mechanical resonator or the electronic filtering [46].

Annovazzi-Lodi and Merlo [46] considered the case of the vibratory mass gyroscope and computed the position fluctuation of the sense mode as the result of mechanical-thermal noise. To compute the noise equivalent angular velocity, Annovazzi-Lodi and Merlo computed the rotation rate for a unity signal to noise ratio. Bao [48] arrived at the similar noise equivalent angular velocity for the vibrating mass gyroscope by equating the Coriolis force with the fluctuating noise force. The noise equivalent rotation rate, MTNΩ is given by

$$\mathrm{MTN}\Omega = \frac{c^{3/2}\sqrt{4\,k_B\,T\,BW}}{2\,M\,F_e} \tag{1.2}$$

where M is the mass in kilogram and F_e the excitation force in newton.

Including the effect of frequency mismatch, Leland [49] studied the effects of the thermal noise employing the method of averaging. To this end, Leland derived the "slow" model based on the work of Lynch [50] on deriving the system of slowly varying variables of the vibratory gyroscope. Leland's single-mass vibratory gyroscope was a linear system of two oscillators with linear coupling through the Coriolis term. To derive the MTNΩ, Leland used the Laplace transform of the system of equations and solved the algebraic system for the rotation rate in terms of noise force components. According to Leland the MTNΩ is expressed in the form [49]

$$\mathrm{MTN}\Omega = \frac{\omega_y}{2\,A\,\omega_x\,Q_y}\sqrt{\frac{k_B\,T}{M}} \tag{1.3}$$

where ω_y and ω_x are the natural frequencies of the mass-spring system in the sense and drive directions respectively, A the maximum amplitude in the drive direction, and Q_y the quality factor in the drive direction. Currently, the microgyroscope industry requires the estimation of the thermal noise effect and consequent noise equivalent rotation rate.

1.5 The Thesis

The cantilever-based microgyroscope that carries an eccentric end rigid body experiences flexural-flexural deformation and rigid body rotation, see Figure 1.1(c). Two parallel plate capacitors provide the electrostatic actuation and sense mechanisms. The assumption is that the deformation is small and the stress-strain relation is linear following Hooke's law. The structural nonlinearity is discarded, but the nonlinearity by virtue of the electrostatic field is included in the nonlinear analysis of the system response. The objectives of the thesis are given in the following subsection.

1.5.1 The Objectives of the Thesis

The main objectives of the thesis are to:

- derive the mathematical model of the beam-rigid body gyroscope considering the properties of the end rigid body,
- study the static behaviour of the beam-rigid body microgyroscope,
- investigate the modal frequencies of the microgyroscope and demonstrate the operation of the microgyroscope in the frequency modulation mode,
- derive the "slow" system using a perturbation method, the method of multiple scales, and study the reduced-order nonlinear behaviour of the system,
- analyze the nonlinear behaviour using the computational shooting method and compare the results of the method with the perturbation results,
- and perform the mechanical-thermal (thermomechanical) noise analysis using the linear analysis and the nonlinear analysis.

1.5.2 Mathematical Methods

To develop the equations of motion, the extended Hamilton's principle is employed in the form of [51, 52]

$$\delta\mathcal{I} = \int_{t_i}^{t_f} \left(\delta\mathcal{K} - \delta\mathcal{P} + \overline{\delta\mathcal{W}}_{nc}\right) \mathrm{d}t = 0, \qquad \delta w(x,t) = 0, \qquad t = t_i, t_f \tag{1.4}$$

where $\delta\mathcal{K}$ and $\delta\mathcal{P}$ are the variation of the kinetic and potential energies of the system, and $\overline{\delta\mathcal{W}}_{nc}$ is the virtual work of the nonconservative forces. The kinetic and potential energies and the nonconservative works are computed in terms of the displacements, $w(x,t) = 0$ and $v(x,t) = 0$, inserted in equation (1.4) and the variations are computed. With the assumption that the variations of the displacements at the initial and final times, t_i and t_f, go to zero, the total variation, $\delta\mathcal{I}$, should go

to zero; therefore, the variation in the displacements, δv and δw, and their first spatial derivatives, $\delta v'$ and $\delta w'$, or their coefficients should go to zero at either boundary of the microstructure.

The assumed-mode method is used to derive the discretized system of equations of modal (generalized) coordinates. To this end, the solution (displacement) is described in the finite series of admissible functions, which satisfy the geometric boundary conditions, and the time-dependent generalized or modal coordinates [53]. The kinetic and potential energies are re-expressed in terms of generalized coordinates by the substitutions of the series approximation into them and the equations of motion are computed with the help of Lagrange's equation. The Lagrange's equation is given by [51]

$$\frac{\partial \mathcal{K}}{\partial \Theta_i} - \frac{\partial \mathcal{P}}{\partial \Theta_i} - \frac{\mathrm{d}}{\mathrm{d}t}\left(\frac{\partial \mathcal{K}}{\partial \dot{\Theta}_i}\right) + f_i = 0 \tag{1.5}$$

where Θ_i is replaced with the modal coordinates $p(t)$ and $q(t)$ to obtain the reduced-order model of the system. In equation (1.5), the $\mathcal{K}$ and $\mathcal{P}$ represent kinetic and potential energies in terms of the generalized coordinates and f_i the damping forces.

The reduced-order nonlinear analysis is performed using the method of multiple scales [54, 55, 56]. Employing the method of multiple scales the "slow" system is derived which is used for the frequency-response and force-response analyses of the systems. The Coriolis, damping, and the excitation terms are scaled such that they appear at the third order equations. To compute the steady-state response, the time derivative of the slowly varying variable are set to zero and the roots of the modulation equations are obtained. To determine the stability of solution, the eigenvalues of the Jacobian matrix are computed for the points along each branch of the solution.

If at least one eigenvalue of the Jacobian matrix becomes positive, then the equilibrium solution (the steady-state solution) loses its stability [57]. To plot frequency-response curves, the bifurcation diagram in the plane of the variables, the excitation frequency and the response amplitude, the excitation frequency is swept from below/above to the above/below the effective natural frequency and the amplitude of the steady-state response is computed. The turning point or fold bifurcation points appear where the branch loses its stability, that is an eigenvalue computes to zero, and the slope of the curve goes to infinity [54].

The full model including the second-order excitation, $V_{\mathrm{AC}}^2 \cos(\Omega_e\, t)^2$, the second-order rotation rate, Ω^2, and higher order nonlinearities is studied by using the numerical shooting method [58, 59, 60]. The algorithm converts searching for the periodic solutions to locating the fixed points (equilibrium points) of

$$P(x) := \Phi_{t_0+T}(x, t_0) - x \tag{1.6}$$

using the Newton-Raphson algorithm [59]. In equation (1.6), $\Phi_{t_0+T}(x, t_0)$ indicates the trajectory shoots from t_0 to $t_0 + T$. The stability of the solution is determined via computing Floquet multipliers, that is the eigenvalues of the "monodromay" matrix [58]. For a stable solution all eigenvalues

remain inside the unit circle on the complex plane. For the fold bifurcation points (the turning points) and the subsequent loss of stability, an eigenvalues crosses the unit circle through plus 1 on the real axis [58].

The global stability of the system is further investigated by long-time integration of the equations of motion, finding the homoclinic orbits (paths) and "separatrices", determining the basins of attraction, and plotting the phase-plane diagrams [57, 61, 62]. Various regions on the phase-plane are separated from each other by closed separatrices. Changing the main parameters of the system results in the appearance and disappearance of the center and focus on the phase-plane and construction or destruction of homoclinic and heteroclinic paths.

1.6 Outline of the Thesis

The thesis is divided into seven chapters and one appendix. The appendix includes the list of symbols. The contents of the chapters are described briefly as follows:

- Chapter one: The motivation and the relevant literature are summarized in this chapter. The subject and objectives of the thesis and the mathematical methods are explained. The synopsis of the thesis are briefly reviewed.

- Chapter two: The equations of motion are derived using the extended Hamilton's principle. The reduced-order model of generalized coordinates is obtained using Lagrange's differential equations. Simplified forms of the beam-rigid body model including the beam-mass system are presented. The electrostatic field is modeled and included in the moment and force boundary conditions.

- Chapter three: The static equations are derived by separating the response into the dynamic and static components. The solutions of the static equations, that is the static displacements, are computed for the DC load and the static pull-in voltage are estimated. The linearized dynamic equations are employed to compute the natural frequencies of the system. It is demonstrated that the natural frequencies are used to operate the microgyroscope in the frequency modulation mode.

- Chapter four: The method of multiple scales is used to derive the modulation equations, that is the "slow" system. The frequency-response and force-response plots are generated by increasing and decreasing the excitation frequency, Ω_e, and the excitation amplitude, V_{AC}, in the proper regions. The effects of the frequency matching, DC load matching, the damping, and the excitation amplitude on the reduced-order nonlinear behaviour are investigated.

- Chapter five: The frequency-response and the global stability of the full model including higher order nonlinearities, the second order excitation, and the second order angular rate of rotation are studied by using the computational shooting method. The validity of the perturbation solution is determined by comparing the results of the two methods. The global stability of the system is examined by computing the phase-plane diagrams. The jump and

hysteresis phenomena are investigated by long-time integration of the system near bifurcation points.

- Chapter six: The mechanical-thermal noise response of beam-rigid body vibratory gyroscope is characterized. The mechanical-thermal noise equivalent rotation rate is computed by using the linear approximation of the system response and the nonlinear "slow" system. The numerical results of the two methods are computed and compared to corroborate the conclusions.

- Chapter seven: The summary of the thesis and corresponding conclusions are outlined, some suggestions to improve the design are provided, and the future works are listed.

Chapter 2

Mathematical Models

2.1 Preview

In this chapter, the governing equations of motion of a cantilever beam carrying an end rigid body undergoing gyroscopic motion under transverse electrostatic forcing are derived. In the following sections, a variational approach based on the extended Hamilton's principle is used to obtain the governing differential equations of motion of the structure. To acquire the discretized equations of the motion, the method of assumed modes is employed. It is shown how the end rigid body modifies the dynamic equations of motion. Versions of the equations of motion for a point mass and a point mass located at a distance from the beam's end are presented. The equations are equivalently applicable to the macro-, micro-, and nano-scale problems.

2.2 Beam Kinematics

To derive the equations of motion and the discretized model, kinetic and potential energies are computed first. To this end, the velocity vector at each point on the cross section along the length of beam is derived. It is assumed that the cantilever beam does not undergo large deformations and nor does it experience large strains. Therefore, the geometric and material nonlinearities are not taken into consideration in the current mathematical formulation of the problem. Thus, it is assumed that the beam is a linear elastic structure; however, rotation is accounted for in computing the cross sectional angular rotation rate.

The beam is attached to a frame rotating with a constant angular velocity (rotation rate) which introduces gyroscopic and centripetal effects to the system dynamics. Therefore, the flexural deformations of the beam in two perpendicular directions are coupled via the rotational speed of the base. The end rigid body is a large mass which considerably affects the kinetic energy of the system. The kinematic variables and curvature do not vary along the length of the end rigid body. In Figure 2.1 a schematic of the system is presented.

To study the kinematics of the beam-rigid body system, three coordinate systems are introduced to

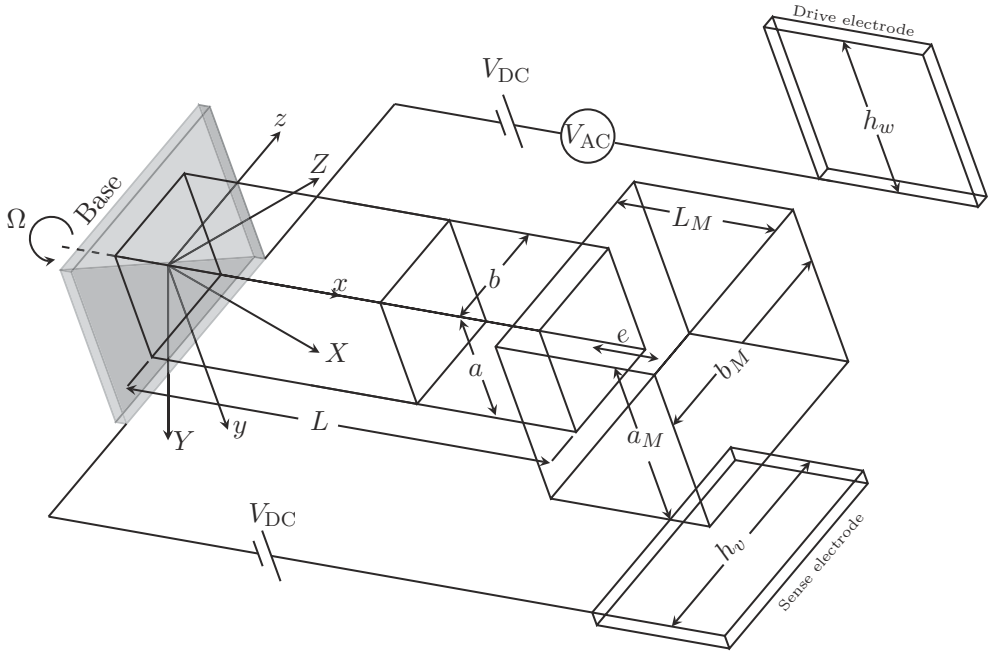

Figure 2.1: Schematic of the beam-rigid body microgyroscope and the electrodes. The figure is not drawn to scale

define the motion of the system: the inertial frame, the base frame, and the cross sectional frame. In Figure 2.2, all three frames are depicted in arbitrary positions. The base frame rotates relative to the inertial frame and the cross sectional frame follows the flexural motion of the beam. The

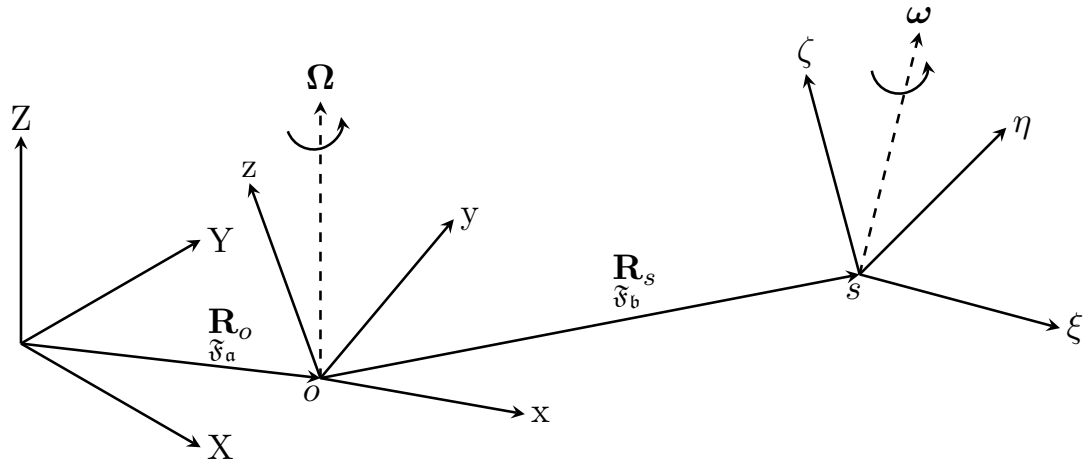

Figure 2.2: The inertial frame and auxiliary coordinate systems.

(X, Y, Z) denote the inertial frame with orthonormal unit vectors $(\mathbf{e}_X, \mathbf{e}_Y, \mathbf{e}_Z)$, (x, y, z) represents the base-attached coordinate system with orthonormal unit vectors $(\mathbf{e}_x, \mathbf{e}_y, \mathbf{e}_z)$ and $(\mathbf{e}_\xi, \mathbf{e}_\eta, \mathbf{e}_\zeta)$ describes the unit vectors of the sectional local coordinates (ξ, η, ζ).

The equation of motion and boundary conditions are described in the base coordinate system. For an arbitrary point p on the cross section, see Figure 2.3, the position vector relative to the local cross section coordinate frame $\mathfrak{F}_\mathfrak{s}$ is defined as

$$\underset{\mathfrak{F}_\mathfrak{s}}{\mathbf{R}}_p = \eta\, \mathbf{e}_\eta + \zeta\, \mathbf{e}_\zeta \tag{2.1}$$

where η and ζ denote the coordinates of p in cross sectional reference frame $\mathfrak{F}_\mathfrak{s}$, see Figure 2.3. The origin of base frame $\mathfrak{F}_\mathfrak{b}$ relative to the inertial frame is positioned at $\underset{\mathfrak{F}_\mathfrak{a}}{\mathbf{R}}_o$, see Figure 2.2, defined by

$$\underset{\mathfrak{F}_\mathfrak{a}}{\mathbf{R}}_o = X_o\, \mathbf{e}_X + Y_o\, \mathbf{e}_Y + Z_o\, \mathbf{e}_Z. \tag{2.2}$$

Upon deformation cross section initially positioned at $x = \ell$ moves to

$$\underset{\mathfrak{F}_\mathfrak{b}}{\mathbf{R}}_s = (\ell + u(\ell, t))\ \mathbf{e}_x + v(\ell, t)\ \mathbf{e}_y + w(\ell, t)\ \mathbf{e}_z \tag{2.3}$$

where $u(\ell, t)$, $v(\ell, t)$ and $w(\ell, t)$ describe the axial and flexural displacements relative to the base frame $\mathfrak{F}_\mathfrak{b}$ in the x, y and z directions. The beam has a uniform cross section and material properties along the length. Consequently, the center of mass and area centroids coincide along the beam length and the cross sectional coordinate system, (ξ, η, ζ), at any cross section is such that $\mathbf{e}_\xi$ is aligned with the neutral axis of the beam and points outward. Computing the velocity vec-

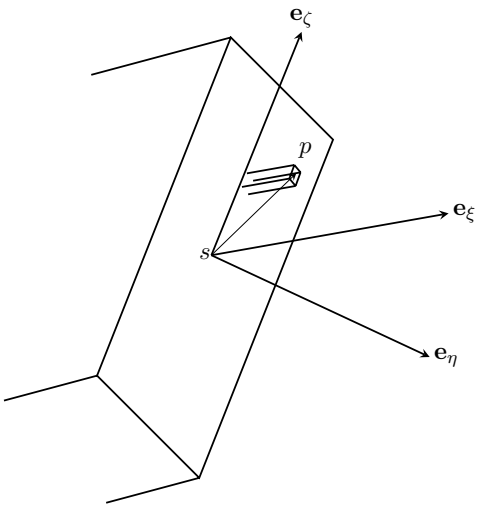

Figure 2.3: The sectional frame and the arbitrary point p on the cross section.

tor at the origin of cross sectional frame (coinciding with the centroid of cross sectional area) is accomplished through

$$\frac{\mathrm{d}}{\mathrm{d}t}\underset{\mathfrak{F}_\mathfrak{a}}{\mathbf{R}_s} = \frac{\mathrm{d}}{\mathrm{d}t}\underset{\mathfrak{F}_\mathfrak{a}}{\mathbf{R}_o} + \frac{\mathrm{d}}{\mathrm{d}t}\underset{\mathfrak{F}_\mathfrak{b}}{\mathbf{R}_s} + \Omega \times \underset{\mathfrak{F}_\mathfrak{b}}{\mathbf{R}_s} \tag{2.4}$$

where $\frac{\mathrm{d}}{\mathrm{d}t}\underset{\mathfrak{F}_\mathfrak{a}}{\mathbf{R}_s}$ represents the velocity vector for a point on the neutral axis of the beam's cross section relative to the inertial frame $\mathfrak{F}_\mathfrak{a}$, and Ω describes the angular velocity of the base coordinate system. In equation (2.4), $\frac{\mathrm{d}}{\mathrm{d}t}\underset{\mathfrak{F}_\mathfrak{a}}{\mathbf{R}_o}$ and $\frac{\mathrm{d}}{\mathrm{d}t}\underset{\mathfrak{F}_\mathfrak{b}}{\mathbf{R}_s}$, the time derivative of position vectors, are computed in $\mathfrak{F}_\mathfrak{a}$ and $\mathfrak{F}_\mathfrak{b}$, respectively. By setting $\underset{\mathfrak{F}_\mathfrak{a}}{\mathbf{R}_o} = 0$, we assume that the base frame and the inertial frame always coincide at their centers.

Similarly, for the arbitrary point p on the cross section, the velocity vector computes to

$$\frac{\mathrm{d}}{\mathrm{d}t}\underset{\mathfrak{F}_\mathfrak{a}}{\mathbf{R}_p} = \frac{\mathrm{d}}{\mathrm{d}t}\underset{\mathfrak{F}_\mathfrak{a}}{\mathbf{R}_s} + \frac{\mathrm{d}}{\mathrm{d}t}\underset{\mathfrak{F}_\mathfrak{s}}{\mathbf{R}_p} + \boldsymbol{\omega} \times \underset{\mathfrak{F}_\mathfrak{s}}{\mathbf{R}_p} \tag{2.5}$$

where $\boldsymbol{\omega}$ denotes the cross sectional angular velocity vector. The angular velocity vectors of the base and the cross section are given by:

$$\boldsymbol{\Omega} = \Omega_x\,\mathbf{e}_x + \Omega_y\,\mathbf{e}_y + \Omega_z\,\mathbf{e}_z \tag{2.6}$$

and

$$\boldsymbol{\omega} = \omega_x\,\mathbf{e}_x + \omega_y\,\mathbf{e}_y + \omega_z\,\mathbf{e}_z \tag{2.7}$$

in the base frame $\mathfrak{F}_b$ or

$$\boldsymbol{\omega} = \omega_\xi\,\mathbf{e}_\xi + \omega_\eta\,\mathbf{e}_\eta + \omega_\zeta\,\mathbf{e}_\zeta \tag{2.8}$$

in the cross sectional local frame $\mathfrak{F}_s$. Substituting equations (2.1), (2.3), (2.4) into equation (2.5), using equations (2.6) and (2.8), and assuming that $\mathfrak{F}_b$ does not translate, that is the base only rotates, the velocity vector at an arbitrary point p on the cross section is given by

$$\begin{aligned}\dot{\underset{\mathfrak{F}_\mathfrak{a}}{\mathbf{R}}}_p =& \dot{u}(\ell,t)\,\mathbf{e}_x + \dot{v}(\ell,t)\,\mathbf{e}_y + \dot{w}(\ell,t)\,\mathbf{e}_z \\ &+ \Big(\Omega_x\,\mathbf{e}_x + \Omega_y\,\mathbf{e}_y + \Omega_z\,\mathbf{e}_z\Big) \times \Big((\ell + u(\ell,t))\,\mathbf{e}_x + v(\ell,t)\,\mathbf{e}_y + w(\ell,t)\,\mathbf{e}_z\Big) \\ &+ \Big(\omega_\xi\,\mathbf{e}_\xi + \omega_\eta\,\mathbf{e}_\eta + \omega_\zeta\,\mathbf{e}_\zeta\Big) \times \Big(\eta\,\mathbf{e}_\eta + \zeta\,\mathbf{e}_\zeta\Big)\end{aligned} \tag{2.9}$$

where overdot ($\dot{}$) denotes differentiation with respect to time.

To compute the velocity vector, equation (2.9), the rotation vector $\boldsymbol{\omega}$ is computed first. Each cross section of the beam undergoes translation and rotation due to elastic deformation and rigid body motion. To characterize the rotation associated with the cross section, the 3-2-1 Euler angle

convention is used mapping the initial configuration to the final configuration.

Therefore, using the 3-2-1 body-fixed Euler angle convention, the first rotation ψ is about the current $\mathbf{e}_z$-axis, parallel to beam's transverse axis, and takes (x, y, z) to (x', y', z'), see Figure 2.4. The second rotation θ is about y' and maps (x', y', z') to (x'', y'', z''), and the final rotation ϕ is about x'' and takes (x'', y'', z'') to the $(x''', y''', z''') = (\xi, \eta, \zeta)$ coordinate system where the ξ-axis is aligned with the neutral axis of the beam and is perpendicular to the cross section of the beam. The four sets of unit vectors are related to each other through the transformation matrices as:

$$\begin{bmatrix} \mathbf{e}_{x'} \\ \mathbf{e}_{y'} \\ \mathbf{e}_{z'} \end{bmatrix} = \mathbb{T}_{\psi} \begin{bmatrix} \mathbf{e}_{x} \\ \mathbf{e}_{y} \\ \mathbf{e}_{z} \end{bmatrix} \tag{2.10}$$

where

$$\mathbb{T}_{\psi} = \begin{bmatrix} \cos_{\psi} & \sin_{\psi} & 0 \\ -\sin_{\psi} & \cos_{\psi} & 0 \\ 0 & 0 & 1 \end{bmatrix}, \tag{2.11}$$

$$\begin{bmatrix} \mathbf{e}_{x''} \\ \mathbf{e}_{y''} \\ \mathbf{e}_{z''} \end{bmatrix} = \mathbb{T}_{\theta} \begin{bmatrix} \mathbf{e}_{x'} \\ \mathbf{e}_{y'} \\ \mathbf{e}_{z'} \end{bmatrix} \tag{2.12}$$

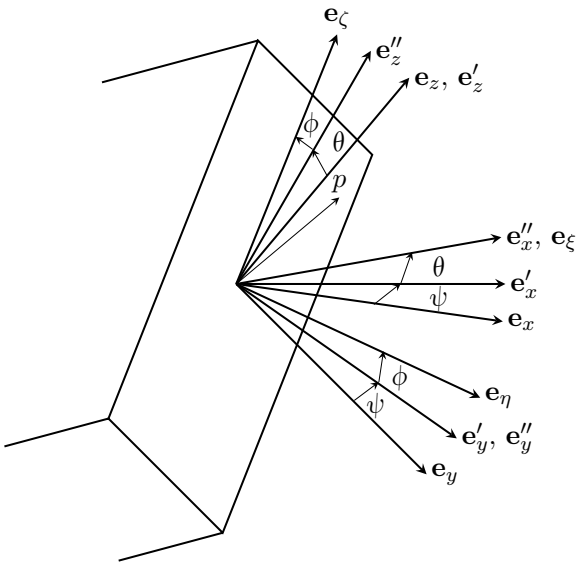

Figure 2.4: Representation of the Euler angles and the cross sectional frame.

where

$$\mathbb{T}_\theta = \begin{bmatrix} \cos_\theta & 0 & -\sin_\theta \\ 0 & 1 & 0 \\ \sin_\theta & 0 & \cos_\theta \end{bmatrix} \tag{2.13}$$

Thus,

$$\begin{bmatrix} \mathbf{e}_{x''} \\ \mathbf{e}_{y''} \\ \mathbf{e}_{z''} \end{bmatrix} = \mathbb{T}_\theta \, \mathbb{T}_\psi \begin{bmatrix} \mathbf{e}_x \\ \mathbf{e}_y \\ \mathbf{e}_z \end{bmatrix} \tag{2.14}$$

And the final rotation about x''-axis is defined by

$$\begin{bmatrix} \mathbf{e}_{x'''} \\ \mathbf{e}_{y'''} \\ \mathbf{e}_{z'''} \end{bmatrix} = \mathbb{T}_\phi \begin{bmatrix} \mathbf{e}_{x''} \\ \mathbf{e}_{y''} \\ \mathbf{e}_{z''} \end{bmatrix} \tag{2.15}$$

where

$$\mathbb{T}_\phi = \begin{bmatrix} 1 & 0 & 0 \\ 0 & \cos_\phi & \sin_\phi \\ 0 & -\sin_\phi & \cos_\phi \end{bmatrix} \tag{2.16}$$

Therefore,

$$\begin{bmatrix} \mathbf{e}_{x'''} \\ \mathbf{e}_{y'''} \\ \mathbf{e}_{z'''} \end{bmatrix} = \mathbb{T}_\phi \, \mathbb{T}_\theta \, \mathbb{T}_\psi \begin{bmatrix} \mathbf{e}_x \\ \mathbf{e}_y \\ \mathbf{e}_z \end{bmatrix} \tag{2.17}$$

or

$$\begin{bmatrix} \mathbf{e}_\xi \\ \mathbf{e}_\eta \\ \mathbf{e}_\zeta \end{bmatrix} = \mathbb{T} \begin{bmatrix} \mathbf{e}_x \\ \mathbf{e}_y \\ \mathbf{e}_z \end{bmatrix} \tag{2.18}$$

where

$$\begin{aligned} \mathbb{T} =& \mathbb{T}_\phi \, \mathbb{T}_\theta \, \mathbb{T}_\psi \\ =& \begin{bmatrix} \cos_\theta \cos_\psi & \cos_\theta \sin_\psi & -\sin_\theta \\ \sin_\phi \sin_\theta \cos_\psi - \cos_\phi \sin_\psi & \sin_\phi \sin_\theta \sin_\psi + \cos_\phi \cos_\psi & \sin_\phi \cos_\theta \\ \cos_\phi \sin_\theta \cos_\psi + \sin_\phi \sin_\psi & \cos_\phi \sin_\theta \sin_\psi - \sin_\phi \cos_\psi & \cos_\phi \cos_\theta \end{bmatrix} \end{aligned} \tag{2.19}$$

The cross sectional angular velocity vector $\boldsymbol{\omega}$ is expressed in the form

$$\begin{aligned}\boldsymbol{\omega} =&\Omega_x\,\mathbf{e}_x + \Omega_y\mathbf{e}_y + \Omega_z\,\mathbf{e}_z + \dot{\psi}\mathbf{e}_z + \dot{\theta}\mathbf{e}_{y'} + \dot{\phi}\mathbf{e}_{x''}\\ =&\omega_\xi\,\mathbf{e}_\xi + \omega_\eta\,\mathbf{e}_\eta + \omega_\zeta\,\mathbf{e}_\zeta\end{aligned} \tag{2.20}$$

Substituting for $\mathbf{e}_x, \mathbf{e}_y$ and $\mathbf{e}_z$ in equation (2.20) using equations (2.14) and (2.18), the following relations for sectional angular velocity in the local frame are obtained:

$$\omega_\xi = \Omega_x \cos_\theta \cos_\psi + \Omega_y \cos_\theta \sin_\psi - \Omega_z \sin_\theta - \dot{\psi}\ \sin_\theta + \dot{\phi} \tag{2.21}$$

$$\begin{aligned}\omega_\eta =& \Omega_x\left(\sin_\phi \sin_\theta \cos_\psi - \cos_\phi \sin_\psi\right) + \Omega_y\left(\sin_\phi \sin_\theta \sin_\psi + \cos_\phi \cos_\psi\right)\\ &+ \Omega_z \sin_\phi \cos_\theta + \dot{\psi}\ \sin_\phi \cos_\theta + \dot{\theta}\ \cos_\phi\end{aligned} \tag{2.22}$$

$$\begin{aligned}\omega_\zeta =& \Omega_x\left(\cos_\phi \sin(\theta) \cos_\psi + \sin_\phi \sin_\psi\right) + \Omega_y\left(\cos_\phi \sin_\theta \sin_\psi - \sin_\phi \cos_\psi\right)\\ &+ \Omega_z \cos_\phi \cos_\theta + \dot{\psi}\ \cos_\phi \cos_\theta - \dot{\theta} \sin_\phi\end{aligned} \tag{2.23}$$

Substituting equations (2.21)-(2.23) into equation (2.9) and using equations (2.18)-(2.19), the velocity vector of the point p on the cross section is expressed in the form

$$\begin{aligned}\underset{\mathfrak{F}_a}{\dot{\mathbf{R}}}_p =& \Big(\dot{v}\ \cos_\theta \sin_\psi + \left(\Omega_y w - \Omega_z v\right)\cos_\theta \cos_\psi - \dot{w}\ \sin_\theta - \left(\Omega_x v - \Omega_y(\ell + u)\right)\sin_\theta\\ &+ \Big(\Omega_x\left(\sin_\phi \sin_\theta \cos_\psi - \cos_\phi \sin_\psi\right) + \Omega_y\left(\sin_\phi \sin_\theta \sin_\psi + \cos_\phi \cos_\psi\right) + \Omega_z \sin_\phi \cos_\theta\\ &+ \dot{\psi}\ \sin_\phi \cos_\theta + \dot{\theta}\ \cos_\phi\Big)\zeta - \Big(\Omega_x\left(\cos_\phi \sin_\theta \cos_\psi + \sin_\phi \sin_\psi\right) + \Omega_y\left(\cos_\phi \sin_\theta \sin_\psi - \sin_\phi \cos_\psi\right)\\ &+ \Omega_z \cos_\phi \cos_\theta + \dot{\psi}\ \cos_\phi \cos_\theta - \dot{\theta}\ \sin_\phi\Big)\eta + \left(\Omega_z(s + u) - \Omega_x w\right)\cos_\theta \sin_\psi + \dot{u}\ \cos_\theta \cos_\psi\Big)\mathbf{e}_\xi\\ &\Big(\ell\Big(\dot{u}\ \left(\sin_\phi \sin_\theta \cos_\psi - \cos_\phi \sin_\psi\right) - \left(\Omega_x \cos_\theta \cos_\psi + \Omega_y \cos_\theta \sin_\psi - \Omega_z \sin_\theta - \dot{\psi}\ \sin_\theta + \dot{\phi}\right)\zeta\\ &+ \left(\Omega_y w - \Omega_z v\right)\left(\sin_\phi \sin_\theta \cos_\psi - \cos_\phi \sin_\psi\right) + \dot{w}\ \sin_\phi \cos_\theta + \left(\Omega_z(\ell + u) - \Omega_x w\right)\left(\cos_\phi \cos_\psi\right.\\ &\left.+ \sin_\phi \sin_\theta \sin_\psi\right) + \dot{v}\ \left(\sin_\phi \sin_\theta \sin_\psi + \cos_\phi \cos_\psi\right) + \left(\Omega_x v - \Omega_y(\ell + u)\right)\sin_\phi \cos_\theta\Big)\Big)\mathbf{e}_\eta\\ &\Big(\ell\Big(\dot{u}\ \left(\cos_\phi \sin_\theta \cos_\psi + \sin_\phi \sin_\psi\right) + \dot{w}\ \cos_\phi \cos_\theta + \left(\Omega_x \cos_\theta \cos_\psi + \Omega_y \cos_\theta \sin_\psi - \Omega_z \sin_\theta\right.\\ &\left.- \dot{\psi}\ \sin_\theta + \dot{\phi}\right)\eta + \dot{v}\ \left(\cos_\phi \sin_\theta \sin_\psi - \sin_\phi \cos_\psi\right) + \left(\Omega_y w - \Omega_z v\right)\left(\cos_\phi \sin_\theta \cos_\psi + \sin_\phi \sin_\psi\right)\\ &+ \left(\Omega_z(\ell + u) - \Omega_x w\right)\left(\cos_\phi \sin_\theta \sin_\psi - \sin_\phi \cos_\psi\right) + \left(\Omega_x v - \Omega_y(\ell + u)\right)\cos_\phi \cos_\theta\Big)\Big)\mathbf{e}_\zeta\end{aligned} \tag{2.24}$$

which gives the full description of the velocity vector at any point on the cross section of the beam along its length. However, substitution of equation (2.22) in the kinetic energy expression and applying the extended Hamilton's principle or Lagrange's equations results in the nonlinear transcendental equations of motion which hardly present any analytical solution and suffer from

instability in numerical solution. Therefore, the rotation angles are described in terms of displacements and trigonometric terms replaced with their equivalent Taylor's expansion.

An element of the beam's neutral axis in the undeformed and deformed positions are shown in Figure 2.5. Displacement vectors in general are described with

$$\underset{\mathfrak{F}_b}{\mathbf{r}}_{\ell} = u(\ell,t)\,\mathbf{e}_x + v(\ell,t)\,\mathbf{e}_y + w(\ell,t)\,\mathbf{e}_z \tag{2.25}$$

$$\underset{\mathfrak{F}_b}{\mathbf{r}}_{\ell+\delta\ell} = u(\ell+\delta\ell,t)\,\mathbf{e}_x + v(\ell+\delta\ell,t)\,\mathbf{e}_y + w(\ell+\delta\ell,t)\,\mathbf{e}_z \tag{2.26}$$

Bending about z-axis translates the element $\delta\ell$ to $\hat{\delta\ell}$, thus the rotation angle ψ is computed to

$$\begin{aligned}\psi &= \arctan\frac{v(\ell+\delta\ell,t)-v(\ell,t)}{\delta\ell+u(\ell+\delta\ell,t)-u(\ell,t)}\\ &\approx \arctan\frac{v'(\ell,t)}{1+u'(\ell,t)}\end{aligned} \tag{2.27}$$

where higher order terms are negelected upon expanding $v(\ell+\delta\ell,t)$ and $u(\ell+\delta\ell,t)$ in a Taylor series. A second transformation carries $\hat{\delta\ell}$ to $\hat{\hat{\delta\ell}}$ which is obtained from

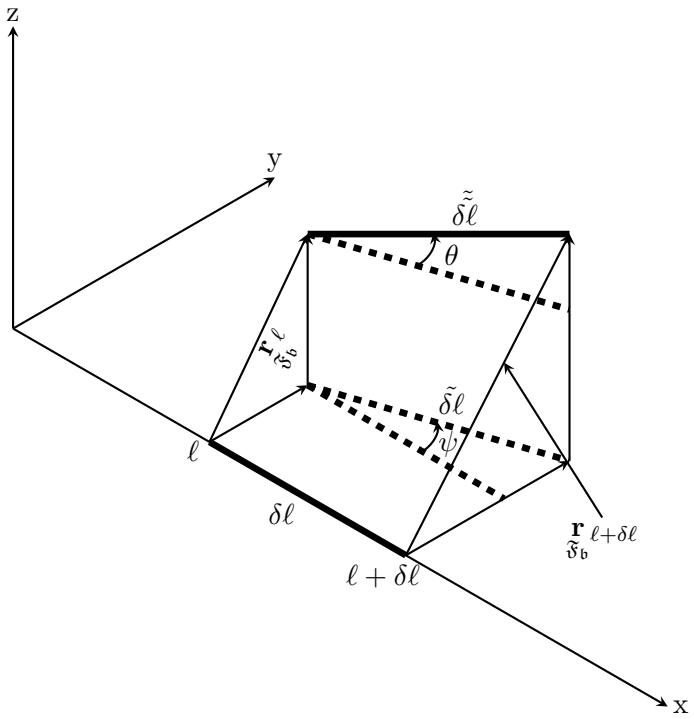

Figure 2.5: An element of the beam's neutral axis in the undeformed and deformed configurations.

$$
\begin{aligned}
\theta &= \arctan \frac{w(\ell+\delta\ell,t)-w(\ell,t)}{\hat{\delta\ell}} \\
&= \arctan \frac{w(\ell+\delta\ell,t)-w(\ell,t)}{\sqrt{\left(\delta\ell+u(\ell+\delta\ell,t)-u(\ell,t)\right)^2+\left(v(\ell+\delta\ell,t)-v(\ell,t)\right)^2}} \\
&\approx \arctan \frac{w'(\ell,t)}{\left(1+u'(\ell,t)\right)^2+v'(\ell,t)^2}.
\end{aligned} \tag{2.28}
$$

Equations (2.27) and (2.28) are used to reduce the trigonometric terms in equation (2.24) to polynomials in the spatial derivatives of the displacements. To this end, the following expansions about the undeformed position up to the fourth order are employed

$$\sin_\psi = v' - v'\,u' - \frac{1}{2}\,v'^3 + v'\,u'^2 + \frac{3}{2}\,v'^3u' - v'\,u'^3 \tag{2.29}$$

$$\cos_\psi = 1 - \frac{1}{2}\,v'^2 + v'^2u' - \frac{3}{2}\,v'^2u'^2 + \frac{3}{8}\,v'^4 \tag{2.30}$$

$$\sin_\theta = -w' + w'\,u' - w'\,u'^2 + \frac{1}{2}\,w'^3 + \frac{1}{2}\,w'\,v'^2 + w'\,u'^3 - \frac{3}{2}\,w'^3u' - \frac{3}{2}\,w'\,v'^2u' \tag{2.31}$$

$$\cos_\theta = 1 - \frac{1}{2}\,w'^2 + w'^2u' - \frac{3}{2}\,w'^2u'^2 + \frac{1}{2}\,w'^2v'^2 + \frac{3}{8}\,w'^4 \tag{2.32}$$

$$\sin_\phi = \phi - \frac{1}{6}\,\phi^3 \tag{2.33}$$

$$\cos_\phi = 1 - \frac{1}{2}\,\phi^2 + \frac{1}{24}\,\phi^4 \tag{2.34}$$

As a side note, replacing the trigonometric expressions in equation (2.19) with their polynomial counterparts, equations (2.29)-(2.34), results in the transformation matrix in terms of axial, flexural, and torsional displacements.

Substitution of equations (2.29)-(2.34) in equation (2.24) and neglecting terms of order four and higher results in the velocity expression

$$
\begin{aligned}
\dot{\mathbf{R}}_{\mathfrak{F}_a p} =& \Big(\big((w' - w'\,u' - \varphi\,v')\,\eta - (v' - v'\,u' + \varphi\,w')\,\zeta - w\,v' + v\,w'\big)\,\Omega_x \\
&+ \Big((w'\,v' + \varphi)\,\eta + \Big(1 - \frac{1}{2}\,\varphi^2 - \frac{1}{2}\,v'^2\Big)\,\zeta + (\ell+u)\,(u'-1)\,w' + w\Big)\,\Omega_y \\
&+ \Big(\Big(\frac{1}{2}\,\varphi^2 + \frac{1}{2}\,w'^2 - 1\Big)\,\eta + (\ell+u)\,(1-u')\,v' - v + \varphi\zeta\Big)\,\Omega_z \\
&+ \big(\dot{v}'\,u' - \varphi\,\dot{w}' + v'\,\dot{u}' - \dot{v}'\big)\,\eta + \big(\dot{w}'\,u' + \varphi\,\dot{v}' + w'\,\dot{u}' - \dot{w}'\big)\,\zeta + \dot{u} + \dot{w}\,w' + \dot{v}\,v'\Big)\,\mathbf{e}_\xi
\end{aligned}
$$

$$
\begin{aligned}
&+\left(\left(\left(\frac{1}{2}\,v'^{\,2}+\frac{1}{2}\,w'^{\,2}-1\right)\zeta-w+\varphi\,v\right)\Omega_x+\left((v'\,u'-v')\,\zeta-(\ell+u)\,\varphi-w\,v'\right)\Omega_y\right.\\
&+\left((w'\,u'-w')\,\zeta+(\ell+u)\left(1-\frac{1}{2}\,v'^{\,2}-\frac{1}{2}\,\varphi^2\right)+v\,v'\right)\Omega_z\\
&\left.-(\dot{\varphi}+\dot{v}'\,w')\,\zeta+\dot{v}-\dot{u}\,v'+\dot{w}\,\varphi\right)\mathbf{e}_\eta\\
&+\left(\left(\left(1-\frac{1}{2}\,w'^{\,2}-\frac{1}{2}\,v'^{\,2}\right)\eta+w\varphi+v\right)\Omega_x\right.\\
&+\left((v'-v'\,u')\,\eta+(\ell+u)\left(\frac{1}{2}w'^{\,2}+\frac{1}{2}\,\varphi^2-1\right)w\,w'\right)\Omega_y\\
&\left.+\left((w'-w'\,u')\,\eta-(\ell+u)\,(\varphi+v'\,w')+v\,w'\right)\Omega_z+(\dot{\varphi}+\dot{v}'\,w')\,\eta-\dot{u}\,w'+\dot{v}\,(1-\varphi)\right)\mathbf{e}_\zeta
\end{aligned}
\tag{2.35}
$$

For a beam under uniaxial rotation about its longitudinal direction, Ω_y and Ω_z are zero, resulting in

$$
\begin{aligned}
\underset{\mathfrak{F}_a}{\dot{\mathbf{R}}}_p=&\left(\left((w'-w'\,u'-\varphi\,v')\,\eta-(v'-v'\,u'+\varphi\,w')\,\zeta-w\,v'+v\,w'\right)\Omega_x\right.\\
&\left.+(\dot{v}'\,u'-\varphi\,\dot{w}'+v'\,\dot{u}'-\dot{v}')\,\eta+(\dot{w}'\,u'+\varphi\,\dot{v}'+w'\,\dot{u}'-\dot{w}')\,\zeta+\dot{u}+\dot{w}\,w'+\dot{v}\,v'\right)\mathbf{e}_\xi\\
&+\left(\left(\left(\frac{1}{2}\,v'^{\,2}+\frac{1}{2}\,w'^{\,2}-1\right)\zeta-w+\varphi\,v\right)\Omega_x-(\dot{\varphi}+\dot{v}'\,w')\,\zeta+\dot{v}-\dot{u}\,v'+\dot{w}\,\varphi\right)\mathbf{e}_\eta\\
&+\left(\left(\left(1-\frac{1}{2}\,w'^{\,2}-\frac{1}{2}\,v'^{\,2}\right)\eta+w\varphi+v\right)\Omega_x+(\dot{\varphi}+\dot{v}'\,w')\,\eta-\dot{u}\,w'+\dot{v}\,(1-\varphi)\right)\mathbf{e}_\zeta
\end{aligned}
\tag{2.36}
$$

Additionally, it is assumed that the torsional and axial rigidity is as high such that the frequency of excitation cannot excite the torsional and axial modes. Therefore, we set u and φ and their derivatives to zero and find that

$$
\begin{aligned}
\underset{\mathfrak{F}_a}{\dot{\mathbf{R}}}_p=&\left((w'\,\eta-v'\,\zeta-w\,v'+v\,w')\,\Omega_x-\dot{v}'\,\eta-\dot{w}'\,\zeta+\dot{w}\,w'+\dot{v}\,v'\right)\mathbf{e}_\xi\\
&+\left(\left(\left(\frac{1}{2}\,v'^{\,2}+\frac{1}{2}\,w'^{\,2}-1\right)\zeta-w\right)\Omega_x-\dot{v}'\,w'\,\zeta+\dot{v}\right)\mathbf{e}_\eta\\
&+\left(\left(\left(1-\frac{1}{2}\,w'^{\,2}-\frac{1}{2}\,v'^{\,2}\right)\eta+v\right)\Omega_x+\dot{v}'\,w'\,\eta+\dot{v}\right)\mathbf{e}_\zeta
\end{aligned}
\tag{2.37}
$$

which describes the velocity at an arbitrary point on the section along the length of the beam providing the negligibility of axial and torsional deformations and the uni-axiality of rotation vector.

2.3 Kinetic Energy

The kinetic energy has two components; that of the beam $\underset{B}{\mathcal{K}}$ and that of the end rigid body $\underset{M}{\mathcal{K}}$. The kinetic energy of beam is defined as

$$\overline{\underset{B}{\mathcal{K}}} = \int_0^L m \, \underset{\mathfrak{F}_a}{\dot{\mathbf{R}}}_p \cdot \underset{\mathfrak{F}_a}{\dot{\mathbf{R}}}_p \, \mathrm{d}x \tag{2.38}$$

where m represents the mass per unit length of the beam with units of $\mathrm{kg\,m^{-1}}$. Substituting for $\underset{\mathfrak{F}_a}{\dot{\mathbf{R}}}_p$ in equation (2.38) using equation (2.37) gives the kinetic energy per unit length of the beam

$$\begin{aligned}\underset{B}{\mathcal{K}} =& \frac{1}{2} m \Omega^2 \left(v^2 + w^2\right) + m \Omega \left(v \dot{w} - w \dot{v}\right) + \frac{1}{2} m \left(\dot{w}^2 + \dot{v}^2\right) - \frac{1}{2} \Omega^2 \left(\underset{B}{J}_{\eta\eta} \left(w'^2 - 1\right) + \underset{B}{J}_{\zeta\zeta} \left(v'^2 - 1\right)\right) \\ &+ \underset{B}{J}_{\eta\eta} \Omega \left(\dot{v}' w' + \dot{w}' v'\right) + \frac{1}{2} \underset{B}{J}_{\eta\eta} \dot{w}'^2 + \frac{1}{2} \underset{B}{J}_{\zeta\zeta} \dot{v}'^2\end{aligned} \tag{2.39}$$

where

$$\underset{B}{J}_{\eta\eta} = \int_{-a/2}^{a/2} \int_{-b/2}^{b/2} \rho \zeta^2 \, \mathrm{d}\zeta \, \mathrm{d}\eta \tag{2.40}$$

$$\underset{B}{J}_{\zeta\zeta} = \int_{-b/2}^{b/2} \int_{-a/2}^{a/2} \rho \eta^2 \, \mathrm{d}\eta \, \mathrm{d}\zeta \tag{2.41}$$

represent rotary inertia of beam and ρ represents the volume mass density in units of $\mathrm{kg\,m^{-3}}$, and a and b denote the thickness and width of beam's cross section respectively. The subscript x is eliminated from Ω_x in the interest of clarity of notation.

The kinetic energy of the end rigid body is given by

$$\underset{M}{\mathcal{K}} = \frac{1}{2} M \, \dot{\mathbf{R}} \cdot \dot{\mathbf{R}} + \dot{\mathbf{R}} \cdot \left(\boldsymbol{\omega}(L,t) \times \int_M \boldsymbol{\beta} \, \mathrm{d}M\right) + \frac{1}{2} \boldsymbol{\omega}(L,t) \cdot \int_M \boldsymbol{\beta} \times (\boldsymbol{\omega}(L,t) \times \boldsymbol{\beta}) \, \mathrm{d}M \tag{2.42}$$

where M is the total mass of the end body, $\mathbf{R}$ the position vector of an arbitrary reference point on the body chosen to coincide with the end of the beam relative to the base frame, that is $\underset{\mathfrak{F}_a}{\dot{\mathbf{R}}}_p$ evaluated at $\ell = L$, $\boldsymbol{\omega}(L,t)$ the angular velocity of the end rigid body obtained from the angular velocity of the beam at L, and $\boldsymbol{\beta}$ the position vector of an arbitrary point in the end rigid body drawn from the end of the beam to the point.

Substitution of equations (2.29)-(2.34) in equations (2.21)-(2.23) and the resulting equation and equation (2.37) in equation (2.42) gives the final form of the kinetic energy of the end rigid body as

$$\underset{M}{\mathcal{K}} = \frac{1}{2} M \left(\dot{w}^2 + \dot{v}^2 + 2\, e \left(\dot{w} \, w' + \dot{v} \, v'\right) + e^2 \Omega^2 \left(w'^2 + v'^2\right) + \Omega^2 \left(v^2 + w^2\right) + e^2 \left(\dot{w}'^2 + \dot{v}'^2\right)\right.$$

$$-2\,\Omega\,(w\,\dot{v} - v\,\dot{w}) + 2\,e\,\Omega^2\,(w\,w' + v\,v') + 2\,e\,\Omega\,(v\,\dot{w}' - w\,\dot{v}') + 2\,\Omega e^2\,(v'\,\dot{w}' - w'\,\dot{v}')$$
$$-2\,e\,\Omega\,(\dot{v}\,w' - \dot{w}\,v')\Big) + \frac{1}{2}\,\underset{M}{J}_{\eta\eta}\left(\dot{w}'^2 + \Omega^2 v'^2 + 2\,\Omega \dot{w}'\,v'\right) + \frac{1}{2}\,\underset{M}{J}_{\zeta\zeta}\left(\dot{v}'^2 + \Omega^2 w'^2 - 2\,\Omega\,\dot{v}' w'\right)$$
$$-\frac{1}{2}\,\underset{M}{J}_{\xi\xi}\left(\Omega^2\,w'^2 + \Omega^2 v'^2 - \Omega^2 - 2\,\Omega\,\dot{v}'\,w'\right). \tag{2.43}$$

In equation (2.43) $\underset{M}{J}_{\xi\xi}$, $\underset{M}{J}_{\eta\eta}$, and $\underset{M}{J}_{\zeta\zeta}$ represent the principal mass moments of inertia of the end rigid body relative to the center of mass of the body and are given by

$$\underset{M}{J}_{\xi\xi} = \iiint_V \rho\left(\zeta^2 + \eta^2\right) \mathrm{d}v \tag{2.44}$$

$$\underset{M}{J}_{\eta\eta} = \iiint_V \rho\left(\xi^2 + \zeta^2\right) \mathrm{d}v \tag{2.45}$$

$$\underset{M}{J}_{\zeta\zeta} = \iiint_V \rho\left(\xi^2 + \eta^2\right) \mathrm{d}v \tag{2.46}$$

where integrations are performed on the volume of the end rigid body V. By setting Ω equal to zero in equations (2.39) and (2.43) the form of the kinetic energy for a beam carrying an eccentric end rigid body experiencing flexural-flexural, but not gyroscopic motion, are obtained:

$$\underset{B}{\mathcal{K}} = \frac{1}{2}\,m\left(\dot{w}^2 + \dot{v}^2\right) + \frac{1}{2}\,\underset{B}{J}_{\eta\eta}\,\dot{w}'^2 + \frac{1}{2}\,\underset{B}{J}_{\zeta\zeta}\,\dot{v}'^2 \tag{2.47}$$

and

$$\underset{M}{\mathcal{K}} = \frac{1}{2}M\left(\dot{w}^2 + \dot{v}^2 + 2\,e\,(\dot{w}\,\dot{w}' + \dot{v}\,\dot{v}') + e^2\left(\dot{w}'^2 + \dot{v}'^2\right)\right) + \frac{1}{2}\,\underset{M}{J}_{\eta\eta}\,\dot{w}'^2 + \frac{1}{2}\,\underset{M}{J}_{\zeta\zeta}\,\dot{v}'^2. \tag{2.48}$$

Furthermore, to obtain the kinetic energy for the in-plane flexural displacement, one bending motion is set to zero, that is $v \equiv 0$ or $w \equiv 0$, in equations (2.47) and (2.48). To compute the kinetic energy expressions for a beam carrying an end point mass, a common configuration of microgyroscopes, the eccentricity e and the mass moment of inertias are set to zero in equation (2.43) obtaining

$$\underset{M}{\mathcal{K}} = \frac{1}{2}M\left(\dot{w}^2 + \dot{v}^2 + \Omega^2\left(v^2 + w^2\right) - 2\,\Omega\,(w\,\dot{v} - v\,\dot{w})\right). \tag{2.49}$$

Conceptually the end mass can be placed further away from the end of the beam and connected to the beam's end via a massless element. For this particular case, equation (2.43) simplifies to

$$\underset{M}{\mathcal{K}} = \frac{1}{2}M\left(\dot{w}^2 + \dot{v}^2 + 2\,e\,(\dot{w}\,\dot{w}' + \dot{v}\,\dot{v}') + e^2\,\Omega^2\left(w'^2 + v'^2\right) + \Omega^2\left(v^2 + w^2\right) + e^2\left(\dot{w}'^2 + \dot{v}'^2\right)\right.$$
$$-2\,\Omega\,(w\,\dot{v} - v\,\dot{w}) + 2\,e\,\Omega^2\,(w\,w' + v\,v') + 2\,e\,\Omega\,(v\,\dot{w}' - w\,\dot{v}') + 2\,\Omega e^2\,(v'\,\dot{w}' - w'\,\dot{v}')$$
$$\left.-2\,e\,\Omega\,(\dot{v}\,w' - \dot{w}\,v')\right). \tag{2.50}$$

In the following analysis, the general form of kinetic energy expressions in equations (2.39) and (2.43) are employed to derive the equations of motion, boundary conditions, and the discretized system of equations of the beam-rigid body gyroscope.

2.4 Potential Energy

The potential energies of the system include the elastic potential energy due to flexural-flexural deformation of the beam and the electrostatic potential energy of the electrostatic field between the pairs of drive and sense electrodes and the end rigid body where the electrostatic force acts. The elastic energy is given by

$$\underset{B}{\mathcal{P}} = -\frac{1}{2}\int_0^L E\, I_{\zeta\zeta}\, v''^2\, \mathrm{d}x \; - \frac{1}{2}\int_0^L E\, I_{\eta\eta}\, w''^2\, \mathrm{d}x, \tag{2.51}$$

where $I_{\zeta\zeta}$ and $I_{\eta\eta}$ respectively represent the cross sectional second moment of area about ζ and η axes and E represents the Young's modulus. Indicating the electrodes' width in the sense and drive directions by h_v and h_w, the electrostatic potential energy is defined as

$$\underset{E}{\mathcal{P}} = \frac{1}{2}\epsilon\; e_v\, h_v\, \frac{{V_v}^2}{g_v - v(L,t) - e\, v'(L,t)} + \frac{1}{2}\epsilon\; e_w\, h_w\, \frac{{V_w}^2}{g_w - w(L,t) - e\, w'(L,t)}, \tag{2.52}$$

where e_v and e_w denote the length of sense and drive electrodes, V_v and V_w denote the voltage differences in the sense and drive directions, g_v and g_w represent the initial distances between the body and sense and drive electrodes, and ϵ represents the permittivity coefficient in units of Fm^{-1}.

2.5 Equations of Motion and Boundary Conditions

By using the extended Hamilton's principle, the governing differential equations of motion and boundary conditions are developed, see Section 1.5.2. In the definition of the functional, equation (1.4), $\mathcal{K}$ and $\mathcal{P}$ are the kinetic and potential energies of the system, $\mathcal{W}_{nc}$ is the work function of the nonconservative forces. The total kinetic energy is given by $\mathcal{K} = \underset{B}{\mathcal{K}} + \underset{M}{\mathcal{K}}$ and the total potential energy by $\mathcal{P} = \underset{B}{\mathcal{P}} + \underset{E}{\mathcal{P}}$.

Equations (2.39), (2.43), (2.51), and the work of nonconservative damping force are substituted into the equation (1.4) and the variations are computed. For the total variation, $\delta\mathcal{I}$, going to zero, the variation in the displacements, δv and δw, and their first spatial derivatives, $\delta v'$ and $\delta w'$, or their coefficients should go to zero at either boundary of the structure. Therefore, the equations of motion become

$$EI_{\eta\eta}\, w'''' + m\,\ddot{w} + 2\,m\,\Omega\,\dot{v} + m\,\dot{\Omega}\,v - m\,\Omega^2 w + c_w\,\dot{w} - \underset{B}{J_{\eta\eta}}\,\Omega^2 w'' - \underset{B}{J_{\eta\eta}}\,\dot{\Omega}\,v'' - \underset{B}{J_{\eta\eta}}\,\ddot{w}'' = 0 \tag{2.53}$$

$$EI_{\zeta\zeta}\, v'''' + m\,\ddot{v} - 2\,m\,\Omega\,\dot{w} - m\,\dot{\Omega}\,w - m\,\Omega^2\,v + c_v\,\dot{v} - \underset{B}{J_{\zeta\zeta}}\,\Omega^2\,v'' - \underset{B}{J_{\eta\eta}}\,\dot{\Omega}\,w'' - \underset{B}{J_{\zeta\zeta}}\,\ddot{v}'' = 0. \tag{2.54}$$

The geometric boundary conditions at $\ell = 0$, are given by

$$w = 0,\ w' = 0,\ v = 0,\ \text{and}\ v' = 0. \tag{2.55}$$

The moment and shear boundary conditions at $\ell = L$ are

$$\begin{aligned} &EI_{\eta\eta}\, w'' - M\, e\, \left(\Omega^2\,(w + e\, w') - \dot{\Omega}\,\,(v + e\, v') - 2\,\Omega\,(\dot{v} + e\,\dot{v}') - (\ddot{w} + e\ddot{w}')\right) + \underset{M}{J}_{\eta\eta}\left(\dot{\Omega}v' + \Omega\dot{v}' + \ddot{w}'\right) \\ &\quad + \underset{M}{J}_{\xi\xi}\left(\Omega^2\, w' - \Omega\,\dot{v}'\right) - \underset{M}{J}_{\zeta\zeta}\left(\Omega^2\, w' - \Omega\,\dot{v}'\right) = \frac{\epsilon\, e\, A_w\, V_w^2}{2\,(g_w - w - e\, w')^2} \end{aligned} \tag{2.56}$$

$$\begin{aligned} &EI_{\zeta\zeta}\, v'' - M\, e\, \left(\Omega^2\,(v + e\, v') + \dot{\Omega}\,\,(w + e\, w') + 2\,\Omega\,(\dot{w} + e\,\dot{w}') - (\ddot{v} + e\ddot{v}')\right) + \underset{M}{J}_{\zeta\zeta}\left(\ddot{v}' - \dot{\Omega}w' - \Omega\,\dot{w}'\right) \\ &\quad - \underset{M}{J}_{\eta\eta}\left(\Omega^2\, v' + \Omega\,\dot{w}'\right) + \underset{M}{J}_{\xi\xi}\left(\Omega^2\, v' + \Omega\,\dot{w}' + \dot{\Omega}w'\right) = \frac{\epsilon\, e\, A_v\, V_v^2}{2\,(g_v - v - e\, v')^2} \end{aligned} \tag{2.57}$$

$$\begin{aligned} &EI_{\eta\eta}\, w''' + M\left(\Omega^2\,\,(w + ew') - \dot{\Omega}\,\,(v + ev') - 2\Omega\,\,(\dot{v} + e\,\dot{v}') - (\ddot{w} + e\ddot{w}')\right) \\ &\quad - \underset{B}{J}_{\eta\eta}\left(\dot{\Omega}v' + \Omega^2 w' + \ddot{w}'\right) = -\frac{\epsilon\, A_w\, V_w^2}{2\,(g_w - w - e\, w')^2} \end{aligned} \tag{2.58}$$

$$\begin{aligned} &EI_{\zeta\zeta}\, v''' + M\left(\Omega^2\,\,(v + ev') + \dot{\Omega}\,\,(w + ew') + 2\Omega\,\,(\dot{w} + e\,\dot{w}') - (\ddot{v} + e\ddot{v}')\right) \\ &\quad - \underset{B}{J}_{\zeta\zeta}\left(\Omega^2 v' + \ddot{v}'\right) - \underset{B}{J}_{\eta\eta}\,\dot{\Omega}\,w' = -\frac{\epsilon\, A_v\, V_v^2}{2\,(g_v - v - e\, v')^2} \end{aligned} \tag{2.59}$$

where A_w and A_v denote the electrostatic forcing area in the drive and sense directions respectively. Therefore, for a beam-point mass gyrsocope where the point mass is placed at distance e relative to the beam's end, the following boundary conditions are obtained (the equations of motion (2.53) and (2.54), equations of forced boundary conditions (2.55), and the equations of shear force boundary conditions (2.58) and (2.59) remain unchanged):

$$EI_{\eta\eta}\, w'' - M\, e\, \left(\Omega^2\,(w + e\, w') - \dot{\Omega}\,\,(v + e\, v') - 2\,\Omega\,(\dot{v} + e\,\dot{v}') - (\ddot{w} + e\ddot{w}')\right) = \frac{\epsilon\, e\, A_w\, V_w^2}{2\,(g_w - w - e\, w')^2} \tag{2.60}$$

and

$$EI_{\zeta\zeta}\, v'' - M\, e\, \left(\Omega^2\,(v + e\, v') + \dot{\Omega}\,\,(w + e\, w') + 2\,\Omega\,(\dot{w} + e\,\dot{w}') - (\ddot{v} + e\ddot{v}')\right) = \frac{\epsilon\, e\, A_v\, V_v^2}{2\,(g_v - v - e\, v')^2}. \tag{2.61}$$

To obtain the shear and moment boundary conditions for the beam-tip mass case, the eccentricity e and the mass moment of inertias $J_{M^{\xi\xi}}$, $J_{M^{\eta\eta}}$, and $J_{M^{\zeta\zeta}}$ are set to zero. Therefore, the moment boundary conditions compute to

$$EI_{\eta\eta}\, w'' = 0, \text{ and } EI_{\zeta\zeta}\, v'' = 0. \tag{2.62}$$

and the shear boundary conditions simplify to

$$EI_{\eta\eta}\, w''' + M\left(\Omega^2\, w - \dot{\Omega}\, v - 2\Omega\,\dot{v} - \ddot{w}\right) = -\frac{\epsilon\, A_w\, V_w^2}{2\,(g_w - w)^2} \tag{2.63}$$

$$EI_{\zeta\zeta}\, v''' + M\left(\Omega^2\, v + \dot{\Omega}\, w + 2\Omega\,\dot{w} - \ddot{v}\right) = -\frac{\epsilon\, A_v\, V_v^2}{2\,(g_v - v)^2} \tag{2.64}$$

In agreement with Euler-Bernoulli beam theory, one can neglect the mass moment of inertia of beam's cross section $J_{B^{\xi\xi}}$, $J_{B^{\eta\eta}}$ and $J_{B^{\zeta\zeta}}$, further simplifying the equations of motion (2.53) and (2.54) and equations of boundary conditions (2.55)-(2.59). For the purpose of this research, equations (2.53)-(2.59) are considered and studied.

Considering electrodes of equal width in the drive and sense directions ($h_w = h_v = h$), and introducing the nondimensional variables

$$\hat{w} = \frac{w}{g_w},\ \hat{v} = \frac{v}{g_v},\ \hat{\ell} = \frac{\ell}{L},\ \hat{t} = \frac{t}{\kappa},\ \hat{\Omega} = \kappa\,\Omega,\ \kappa^2 = \frac{12\,\rho\, L^4}{E\, b^2},\ \Delta = \frac{a_B}{b_B},\ \text{and } \alpha = \frac{b_B^2}{12L^2}, \tag{2.65}$$

and the nondimensional parameters in the form

$$\nu = \frac{6\,\epsilon\, h\, L^4}{E\, b^4\, g^3},\ \hat{M} = \frac{M}{m\, L},\ \hat{e} = \frac{e}{L},\ \hat{J}_{M^{\xi\xi}} = \frac{J_{M^{\xi\xi}}}{mL^3},\ \hat{J}_{M^{\eta\eta}} = \frac{J_{M^{\eta\eta}}}{mL^3},\ \text{and } \hat{J}_{M^{\zeta\zeta}} = \frac{J_{M^{\zeta\zeta}}}{mL^3}, \tag{2.66}$$

the nondimensional equations of motion are expressed in the form

$$\hat{w}'''' + \ddot{\hat{w}} + \hat{c}_w\,\dot{\hat{w}} - \alpha\,\dot{\hat{\Omega}}\,\hat{v}'' + \dot{\hat{\Omega}}\,\hat{v} + 2\,\hat{\Omega}\,\dot{\hat{v}} - \alpha\hat{\Omega}^2\hat{w}'' - \alpha\ddot{\hat{w}}'' - \hat{\Omega}^2\,\hat{w} = 0 \tag{2.67}$$

$$\Delta^2\,\hat{v}'''' + \ddot{\hat{v}} + c_v\,\dot{\hat{v}} - \alpha\,\Delta^2\,\hat{\Omega}^2\,\hat{v}'' - \alpha\,\Delta^2\,\ddot{\hat{v}}'' - \hat{\Omega}^2\,\hat{v} - \alpha\,\dot{\hat{\Omega}}\,\hat{w}'' - \dot{\hat{\Omega}}\,\hat{w} - 2\,\hat{\Omega}\,\dot{\hat{w}} = 0 \tag{2.68}$$

The geometric boundary conditions at $\hat{\ell} = 0$ are

$$\hat{w} = 0,\ \hat{w}' = 0,\ \hat{v} = 0,\ \text{and}\ \hat{v}' = 0 \tag{2.69}$$

and the natural boundary conditions at $\hat{\ell} = 1$ are

$$\begin{aligned}\hat{\Omega}\left(2\Delta\hat{e}^2\,\hat{M}\,\dot{\hat{v}}' + \Delta\dot{\hat{v}}'\left(\hat{J}_{\zeta\zeta} + \hat{J}_{\eta\eta} - \hat{J}_{\xi\xi}\right)\right) + \hat{\Omega}^2\left(\Delta\left(\hat{J}_{\xi\xi} - \hat{J}_{\zeta\zeta}\right)\hat{w}' - \Delta\hat{e}\,\hat{M}\,(\hat{e}\hat{w}' + \hat{w})\right)\\ + 2\Delta\hat{e}\,\hat{M}\,\hat{\Omega}\,\dot{\hat{v}} + \Delta\hat{e}\,\hat{M}\left(\dot{\hat{\Omega}}\,(\hat{e}\hat{v}' + \hat{v}) + \hat{e}\ddot{\hat{w}}' + \ddot{\hat{w}}\right)\\ + \Delta\hat{J}_{\eta\eta}\left(\dot{\hat{\Omega}}\,\hat{v}' + \ddot{\hat{w}}'\right) + \Delta\hat{w}'' = \frac{\hat{e}^2\nu V_w^2}{(\hat{e}\hat{w}' + \hat{w} - 1)^2}\end{aligned} \tag{2.70}$$

$$\begin{aligned}\hat{\Omega}\left(\Delta\dot{\hat{w}}'\left(\hat{J}_{\xi\xi} - \hat{J}_{\zeta\zeta} - \hat{J}_{\eta\eta}\right) - 2\Delta\hat{e}^2\,\hat{M}\,\dot{\hat{w}}'\right) + \hat{\Omega}^2\left(\Delta\left(\hat{J}_{\xi\xi} - \hat{J}_{\eta\eta}\right)\hat{v}' - \Delta\hat{e}\,\hat{M}\,(\hat{e}\hat{v}' + \hat{v})\right)\\ + \Delta\hat{e}\,\hat{M}\left(\hat{e}\ddot{\hat{v}}' - \dot{\hat{\Omega}}\,(\hat{e}\hat{w}' + \hat{w}) + \ddot{\hat{v}}\right) - 2\Delta\hat{e}\,\hat{M}\,\hat{\Omega}\,\dot{\hat{w}}\\ + \Delta\left(\hat{J}_{\zeta\zeta}\ddot{\hat{v}}' + \left(\hat{J}_{\xi\xi} - \hat{J}_{\zeta\zeta}\right)\dot{\hat{\Omega}}\,\hat{w}' + \Delta^2\hat{v}''\right) = \frac{\nu\,\hat{e}^2\,V_v^2}{(1 - \hat{e}\hat{v}' - \hat{v})^2},\end{aligned} \tag{2.71}$$

$$\begin{aligned}\hat{\Omega}^2\left(\Delta\,\hat{M}\,(\hat{e}\hat{w}' + \hat{w}) - \alpha\Delta\hat{w}'\right) - 2\Delta\hat{e}\,\hat{M}\,\hat{\Omega}\,\dot{\hat{v}}' - \Delta\,\hat{M}\left(\dot{\hat{\Omega}}\,(\hat{e}\hat{v}' + \hat{v}) + \hat{e}\ddot{\hat{w}}' + \ddot{\hat{w}}\right) - 2\Delta\,\hat{M}\,\hat{\Omega}\,\dot{\hat{v}}\\ + \Delta\left(\hat{w}''' - \alpha\left(\dot{\hat{\Omega}}\,\hat{v}' + \ddot{\hat{w}}'\right)\right) = -\frac{\hat{e}\nu V_w^2}{(\hat{e}\hat{w}' + \hat{w} - 1)^2}\end{aligned} \tag{2.72}$$

$$\begin{aligned}\hat{\Omega}^2\left(\Delta\,\hat{M}\,(\hat{e}\hat{v}' + \hat{v}) - \alpha\Delta^3\hat{v}'\right) + \Delta\,\hat{M}\left(-\hat{e}\ddot{\hat{v}}' + \dot{\hat{\Omega}}\,(\hat{e}\hat{w}' + \hat{w}) - \ddot{\hat{v}}\right) + 2\Delta\hat{e}\,\hat{M}\,\hat{\Omega}\,\dot{\hat{w}}' + 2\Delta\,\hat{M}\,\hat{\Omega}\,\dot{\hat{w}}\\ + \Delta^3\left(\hat{v}''' - \alpha\ddot{\hat{v}}'\right) - \alpha\Delta\,\dot{\hat{\Omega}}\,\hat{w}' = -\frac{\hat{e}\nu V_v^2}{(\hat{e}\hat{v}' + \hat{v} - 1)^2}\end{aligned} \tag{2.73}$$

where the under-script M in $\hat{J}_{\xi\xi}$, $\hat{J}_{\eta\eta}$, and $\hat{J}_{\zeta\zeta}$ has been removed for the clarity of notation. It is noted that the effects of the moments of inertia and area of the beam are reflected in the cross sectional ratio Δ which is defined as the ratio of the width to the thickness of the beam's cross section in equation (2.63). Nondimensional equations concerning the beam-point mass systems are obtained by setting the parameters associated to the end rigid body equal to zero.

2.6 Discretized Mathematical Model

Computing the dynamic response of a complex system of equations using the reduced-order model (discretized model), is less prone to error and more efficient computationally. The method of assumed modes, see Section 1.5.2, is applied to the system in hand and two second-order ordinary modal equations are obtained. To this end, the response of system in the drive and sense directions, that is w and v, are described in the form

$$w(\ell,t) = q(t)\,\psi(\ell), \quad \text{and} \quad v(\ell,t) = p(t)\,\phi(\ell) \tag{2.74}$$

where $\psi(\ell)$ and $\phi(\ell)$ represent mode shapes (eigenfunctions) satisfying the geometric boundary conditions of the structure, and $q(t)$ and $p(t)$ indicate the generalized (modal) coordinates of the structures' response in the drive and sense directions, respectively.

Substituting equations (2.39), (2.43), (2.51) and (2.52) into Lagrange's differential equations, see Section 1.5.2, using equation (2.74), and adding a Rayleigh dissipation function in terms of the modal coordinates the nondimensional reduced-order (discretized) model is obtained in the form

$$\begin{aligned}
&\Delta\left(\Gamma+\alpha\,\Gamma'+\underset{M}{\hat{J}}_{\eta\eta}\,\psi'(1)^2+\hat{M}\,\left(\psi(1)+\hat{e}\,\psi'(1)\right)^2\right)\ddot{\hat{q}}(t)+\hat{c}_q\,\dot{\hat{q}}(\hat{t}) \\
&+\Delta\,\hat{\Omega}(\hat{t})\left(2\,\Pi-\left(\underset{M}{\hat{J}}_{\xi\xi}-\underset{M}{\hat{J}}_{\eta\eta}-\underset{M}{\hat{J}}_{\zeta\zeta}\right)\phi'(1)\psi'(1)+2\,\hat{M}\,\left(\phi(1)+\,\hat{e}\,\phi'(1)\right)\left(\psi(1)+\hat{e}\,\psi'(1)\right)\right)\dot{\hat{p}}(\hat{t}) \\
&+\Delta\,\dot{\hat{\Omega}}(\hat{t})\left(\Pi+\alpha\Pi'+\underset{M}{\hat{J}}_{\eta\eta}\,\psi'(1)\,\phi'(1)+\,\hat{M}\,\left(\phi(1)+\,\hat{e}\,\phi'(1)\right)\left(\psi(1)+\hat{e}\,\psi'(1)\right)\right)\hat{p}(\hat{t}) \\
&+\Delta\left(\Gamma''-\hat{\Omega}^2\left(\Gamma-\alpha\,\Gamma'+M\,\left(\psi(1)+\,\hat{e}\,\psi'(1)\right)^2-\underset{M}{\hat{J}}_{\xi\xi}\,\psi'(1)^2+\underset{M}{\hat{J}}_{\zeta\zeta}\,\psi'(1)^2\right)\right)\hat{q}(\hat{t})= \\
&\frac{\nu\,\hat{e}\,(\psi(1)+\hat{e}\psi'(1))\,V_w^2}{\left(1-\,\hat{q}(\hat{t})\,\psi(1)-\hat{e}\,\hat{q}(\hat{t})\psi'(1)\right)^2}
\end{aligned} \tag{2.75}$$

and

$$\begin{aligned}
&\Delta\left(\Lambda+\alpha\,\Delta^2\,\Lambda'+\underset{M}{\hat{J}}_{\zeta\zeta}\,\phi'(1)^2+M\,\left(\phi(1)+\hat{e}\,\phi'(1)\right)^2\right)\ddot{\hat{p}}(\hat{t})+\hat{c}_p\,\dot{\hat{p}}(\hat{t}) \\
&-\Delta\,\hat{\Omega}(t)\left(2\,\Pi+\left(\underset{M}{\hat{J}}_{\eta\eta}+\underset{M}{\hat{J}}_{\zeta\zeta}-\underset{M}{\hat{J}}_{\xi\xi}\right)\phi'(1)\psi'(1)+2\hat{M}\,\left(\psi(1)+\hat{e}\,\psi'(1)\right)\left(\phi(1)+\hat{e}\,\phi'(1)\right)\right)\dot{\hat{q}}(\hat{t}) \\
&-\Delta\,\dot{\hat{\Omega}}(\hat{t})\left(\Pi-\alpha\Pi'+\left(\underset{M}{\hat{J}}_{\zeta\zeta}-\underset{M}{\hat{J}}_{\xi\xi}\right)\psi'(1)\,\phi'(1)+\,\hat{M}\,\left(\phi(1)+\,\hat{e}\,\phi'(1)\right)\left(\psi(1)+\hat{e}\,\psi'(1)\right)\right)\hat{q}(\hat{t}) \\
&+\Delta\left(\Delta^2\,\Lambda''-\hat{\Omega}^2\left(\Lambda-\alpha\,\Delta^2\,\Lambda'+\hat{M}\,\left(\phi+\hat{e}\,\phi'(1)\right)^2-\underset{M}{\hat{J}}_{\xi\xi}\,\phi'(1)^2+\underset{M}{\hat{J}}_{\eta\eta}\,\phi'(1)^2\right)\right)\hat{p}(\hat{t})= \\
&\frac{\nu\,\hat{e}\,(\phi(1)+\hat{e}\phi'(1))\,V_v^2}{\left(1-\,\hat{p}(\hat{t})\phi(1)-\hat{e}\,\hat{p}(\hat{t})\phi'(1)\right)^2}
\end{aligned} \tag{2.76}$$

where

$$\Gamma = \int_0^1 \psi(\hat{\ell})^2 d\hat{\ell},\ \Gamma' = \int_0^1 \psi'(\hat{\ell})^2 d\hat{\ell},\ \Gamma'' = \int_0^1 \psi''(\hat{\ell})^2 d\hat{\ell},$$
$$\Lambda = \int_0^1 \phi(\hat{\ell})^2 d\hat{\ell},\ \Lambda' = \int_0^1 \phi'(\hat{\ell})^2 d\hat{\ell},\ \Lambda'' = \int_0^1 \phi''(\hat{\ell})^2 d\hat{\ell},\ \Pi = \int_0^1 \psi(\hat{\ell})\phi(\hat{\ell}) d\hat{\ell} \tag{2.77}$$

Equations (2.75) and (2.76) describe the single-mode approximation of the response of the beam carrying the eccentric end rigid body undergoing gyroscopic motion actuated by the electrostatic force in the sense and drive directions. Centrifugal and Coriolis forces are proportional to the angular displacement rate in the ordinary differential equations (2.76) and (2.77).

If the rotary inertia of the end mass is proved to be insignificant, that is to say the system is modeled as beam-eccentric point mass, then the equations of motion become

$$\begin{aligned}
&\Delta \left(\Gamma + \alpha\,\Gamma' + \hat{M}\,(\psi(1) + \hat{e}\,\psi'(1))^2\right) \ddot{\hat{q}}(t) + \hat{c}_q\ \dot{\hat{q}}(\hat{t}) \\
&+ \Delta\,\hat{\Omega}(\hat{t}) \left(2\,\Pi + 2\,\hat{M}\,(\phi(1) + \hat{e}\,\phi'(1))\,(\psi(1) + \hat{e}\,\psi'(1))\right) \dot{\hat{p}}(\hat{t}) \\
&+ \Delta\,\dot{\hat{\Omega}}(\hat{t}) \left(\Pi + \alpha\Pi' + \hat{M}\,(\phi(1) + \hat{e}\,\phi'(1))\,(\psi(1) + \hat{e}\,\psi'(1))\right) \hat{p}(\hat{t}) \\
&+ \Delta \left(\Gamma'' - \hat{\Omega}^2 \left(\Gamma - \alpha\,\Gamma' + M\,(\psi(1) + \hat{e}\,\psi'(1))^2\right)\right) \hat{q}(\hat{t}) = \\
&\frac{\nu\,\hat{e}\,(\psi(1) + \hat{e}\psi'(1))\,V_w^2}{\left(1 - \hat{q}(\hat{t})\,\psi(1) - \hat{e}\,\hat{q}(\hat{t})\psi'(1)\right)^2}
\end{aligned} \tag{2.78}$$

and

$$\begin{aligned}
&\Delta \left(\Lambda + \alpha\,\Delta^2\,\Lambda' + M\,(\phi(1) + \hat{e}\,\phi'(1))^2\right) \ddot{\hat{p}}(\hat{t}) + \hat{c}_p\ \dot{\hat{p}}(\hat{t}) \\
&- \Delta\,\hat{\Omega}(t) \left(2\,\Pi + 2\hat{M}\,(\psi(1) + \hat{e}\,\psi'(1))\,(\phi(1) + \hat{e}\,\phi'(1))\right) \dot{\hat{q}}(\hat{t}) \\
&- \Delta\,\dot{\hat{\Omega}}(\hat{t}) \left(\Pi - \alpha\Pi' + \hat{M}\,(\phi(1) + \hat{e}\,\phi'(1))\,(\psi(1) + \hat{e}\,\psi'(1))\right) \hat{q}(\hat{t}) \\
&+ \Delta \left(\Delta^2\,\Lambda'' - \hat{\Omega}^2 \left(\Lambda - \alpha\,\Delta^2\,\Lambda' + \hat{M}\,(\phi + \hat{e}\,\phi'(1))^2\right)\right) \hat{p}(\hat{t}) = \\
&\frac{\nu\,\hat{e}\,(\phi(1) + \hat{e}\phi'(1))\,V_v^2}{\left(1 - \hat{p}(\hat{t})\phi(1) - \hat{e}\,\hat{p}(\hat{t})\phi'(1)\right)^2}
\end{aligned} \tag{2.79}$$

If the dimensions of end rigid body is proved to be insignificant in defining the mechanics of the system, that is to say only the mass of the proof end mass affects the systems dynamics, the reduced-order model is given by

$$\begin{aligned}
&\Delta\ (\Gamma\ + \alpha\,\Gamma' + \hat{M}\,(\psi(1) + \hat{e}\,\psi'(1))^2) \ddot{\hat{q}}(t) + \hat{c}_q\ \dot{\hat{q}}(\hat{t}) + \Delta\,\hat{\Omega}(\hat{t}) \left(2\,\Pi + 2\,\hat{M}\,\phi(1)\,\psi(1)\right) \dot{\hat{p}}(\hat{t}) \\
&\quad + \Delta\,\dot{\hat{\Omega}}(\hat{t}) \left(\Pi + \alpha\Pi' + \hat{M}\,\phi(1)\,\psi(1)\right) \hat{p}(\hat{t}) + \Delta \left(\Gamma'' - \hat{\Omega}^2 \left(\Gamma - \alpha\,\Gamma' + M\,\psi(1)^2\right)\right) \hat{q}(\hat{t})
\end{aligned}$$

$$= \frac{\nu\,\hat{e}\,(\psi(1) + \hat{e}\psi'(1))\,V_w^2}{\left(1 - \hat{q}(\hat{t})\,\psi(1) - \hat{e}\,\hat{q}(\hat{t})\psi'(1)\right)^2} \tag{2.80}$$

and

$$\begin{aligned}
&\Delta\,(\Lambda + \alpha\,\Delta^2\,\Lambda' + M\,\phi(1)^2)\,\ddot{\hat{p}}(\hat{t}) + \hat{c}_p\,\dot{\hat{p}}(\hat{t}) - \Delta\,\hat{\Omega}(t)\left(2\,\Pi + 2\hat{M}\,\psi(1)\,\phi(1)\right)\dot{\hat{q}}(\hat{t}) \\
&\quad - \Delta\,\dot{\hat{\Omega}}(\hat{t})\left(\Pi - \alpha\Pi' + \hat{M}\,\phi(1)\,\psi(1)\right)\hat{q}(\hat{t}) + \Delta\left(\Delta^2\,\Lambda'' - \hat{\Omega}^2\left(\Lambda - \alpha\,\Delta^2\,\Lambda' + \hat{M}\,\phi^2\right)\right)\hat{p}(\hat{t}) \\
&= \frac{\nu\,\hat{e}\,(\phi(1) + \hat{e}\phi'(1))\,V_v^2}{\left(1 - \hat{p}(\hat{t})\phi(1) - \hat{e}\,\hat{p}(\hat{t})\phi'(1)\right)^2}
\end{aligned} \tag{2.81}$$

The electrostatic force introduces nonlinearity into the differential equations of motion. Upon multiplying each equation by the denominator of the respective electrostatic force, quadratic and cubic nonlinearities appear in the system of governing differential equations. Therefore, the study of instability and bifurcation of system response is a must. In the following chapters, a thorough analysis of the static response, modal frequencies, linear dynamics, and nonlinear dynamics of the system are performed. In operating micromachined gyroscopes, the mechanical-thermal noise is one of the most significant parameters affecting the performance of the microsensor. Therefore, the noise response of the system is systematically studied using the linear dynamics and the nonlinear perturbation analysis.

2.7 Summary

In this chapter, the mathematical models of a beam with a rectangular cross section carrying an end rigid body undergoing three dimensional motion in the space has been derived. The models consider a single-axis rigid body rotation representing a single-axis gyroscope, however can be extended to the three-axis rotation following the same pattern as discussed in this writing. The equations of motion and boundary conditions and the reduced-order (discretized) model have been obtained by using the extended Hamilton's principle and the method of assumed modes. The models of other but simpler systems have also been obtained and presented for the sake of completeness of the discussion.

Chapter 3

Statics, Modal Frequencies, and the Computation of Rotation Rate

3.1 Preview

The static configuration of the structure, beam and the end rigid body, is determined by computing the response of the system under the bias voltage including the angular rotation rate. This chapter consists of analyzing the static configuration of the microstructure, computing the free response of the structure under angular rotation rate including the natural frequencies and mode shapes, and calculating the effects of DC loading on the otherwise unforced response of the structure.

The mode shapes (eigenfunctions) and natural (modal) frequencies of the uncoupled system of equations are the basis of computations in the following sections and calculated in the first step. The next part focuses on the computation of the exact static deformation with and without angular rotation rate. The natural frequencies in the presence of an input angular rotation rate are computed in the next part. The region of instability due to input angular rate is identified. The input angular rotation rate is computed in terms of the difference of the modal frequencies which is the basis for the rotation rate estimation in the frequency modulation method.

3.2 The Analysis of Uncoupled System

The uncoupled system of governing differential equations and boundary conditions are obtained by removing the terms associated with the angular rotation rate. Thus, setting $\hat{\Omega} = 0$ in equations (2.67)-(2.73) yields two governing equations,

$$w'''' + \ddot{w} + c_w \dot{w} - \alpha \ddot{w}'' = 0 \tag{3.1}$$

$$\Delta^2 v'''' + \ddot{v} + c_v \dot{v} - \alpha \Delta^2 \ddot{v}'' = 0, \tag{3.2}$$

four geometric boundary conditions at $\ell = 0$

$$w = 0,\ w' = 0,\ v = 0,\ \text{and}\ v' = 0, \tag{3.3}$$

and four natural boundary conditions at $\ell = 1$

$$\Delta w'' + \Delta e\ M\ (e\,\ddot{w}' + \ddot{w}) + \Delta J_{\eta\eta}\ddot{w}' = \frac{\nu\, e^{\,2} V_w^2}{(1 - e\,w' - w)^2} \tag{3.4}$$

$$\Delta^3 v'' + \Delta e\ M\ (e\,\ddot{v}' + \ddot{v}) + \Delta\, J_{\zeta\zeta}\ddot{v}' = \frac{\nu\, e^{\,2}\, V_v^2}{(1 - e\,v' - v)^2}, \tag{3.5}$$

$$\Delta\, w''' - \Delta\, M\ (\ddot{w} + e\,\ddot{w}') + \Delta\,\alpha\ddot{w}' = -\frac{\nu\, e\, V_w^2}{(1 - e\,w' - w)^2} \tag{3.6}$$

$$\Delta^3\, v''' + \Delta\, M\ (-e\,\ddot{v}' - \ddot{v}) - \alpha\,\Delta^3\,\ddot{v}' = -\frac{\nu\, e\, V_v^2}{(1 - e\,v' - v)^2}, \tag{3.7}$$

where the over symbol (ˆ) has been removed from the nondimensional quantities for the clarity of notation. The preceding set of equations for the uncoupled system, (3.1)- (3.7), are initially investigated to compute the required fundamental results for the analysis of beam-rigid body gyroscope.

3.2.1 Static Analysis

The static analysis of the equations in the drive and sense directions follow similar steps. Therefore, the analysis is presented for the drive direction. To this end, the displacement w is separated into the static and dynamic components, that is

$$w(\ell, t) = w_s(\ell) + w_d(\ell, t) \tag{3.8}$$

Substituting equation (3.8) into (3.1)- (3.7), and dropping damping and dynamic terms, that is $c_w = 0$ and $w_d(\ell, t) = 0$, results in the static governing equation

$$w_s'''' = 0,\ 0 < \ell < 1, \tag{3.9}$$

and the boundary conditions as

$$w_s = 0,\ w_s' = 0,\ \text{at}\ \ell = 0, \tag{3.10}$$

$$\Delta w_s'' = \frac{\nu\, e^{\,2}\, V_w^2}{\left(1 - e\, w_s' - w_s\right)^2},\ \Delta\, w_s''' = -\frac{\nu\, e\, V_w^2}{\left(1 - e\, w_s' - w_s\right)^2},\ \text{at}\ \ell = 1. \tag{3.11}$$

The solution of ordinary differential equation (3.9) is expressed in the form

$$w_s(\ell) = C_1 + C_2\,\ell + C_3\,\ell^2 + C_4\,\ell^3 \tag{3.12}$$

where C_1, C_2, C_3, and C_4 are found by applying the boundary conditions, equations (3.10)-(3.11). Applying the essential boundary conditions, equations (3.10), C_1 and C_2 vanish. Thus, the displacement at beam's tip is expressed in terms of two other constants. Differentiating equation (3.12) with respect to the spatial variable, once, twice, and three times, gives the slope and higher order terms in the natural boundary conditions along the beam's length. Therefore,

$$w_s(1) = C_3 + C_4 \tag{3.13}$$
$$w_s'(1) = 2\,C_3 + 3\,C_4 \tag{3.14}$$
$$w_s''(1) = 2\,C_3 + 6\,C_4 \tag{3.15}$$
$$w_s'''(1) = 6\,C_4 \tag{3.16}$$

Substituting equations (3.13)-(3.16) into equations (3.11), multiplying the second equation by e, and adding the equations together results in

$$2\Delta(C_3 + 3(1+e)C_4) = 0 \tag{3.17}$$

which is solved for one of the coefficients and gives

$$C_3 = -3\,C_4\,(1 + e) \tag{3.18}$$

Substituting equation (3.18) into (3.13), gives

$$C_4 = -\frac{w_s(1)}{2 + 3e} \tag{3.19}$$

and

$$C_3 = 3\,\frac{w_s(1)}{2 + 3\,e}(1 + e) \tag{3.20}$$

Substituting equations (3.13), (3.14), and (3.15) into the second equation in (3.11), and replacing C_3 and C_4 with their equivalents from equations (3.19) and (3.20), multiplying through by the denominator of the electrostatic force results in the closed-form relation of the static displacement-DC voltage as

$$\Delta\left(216e^4 + 432e^3 + 360e^2 + 144e + 24\right) w_s(1)^3$$
$$-\,\Delta\left(216e^3 - 360e^2 + 216e + 48\right) w_s(1)^2$$

$$+\Delta\left(54e^2+72e+24\right)w_s(1)=\nu\,e\left(27e^3+54e^2+36e+8\right)V_w^2 \tag{3.21}$$

Following a similar procedure and describing the constants, C_3 and C_4, in terms of the slope $w_s'(1)$, the corresponding cubic algebraic equation to compute the slope at beam's tip $w_s'(1)$ is found

$$\begin{aligned}&\Delta\left(72e^4+144e^3+120e^2+48e+8\right)w_s'(1)^3\\&-\Delta\left(144e^3+216e^2+120e+24\right)w_s'(1)^2\\&+\Delta\left(72e^2+72e+18\right)w_s'(1)=\nu\,e\left(72e^3+108e^2+54e+9\right)V_w^2\end{aligned} \tag{3.22}$$

Computing and substituting the solutions of equations (3.21) and (3.22), that is displacement $w_s(1)$ and slope $w_s'(1)$, in $w_s(1)+e\,w_s'(1)$ gives the displacement at the center of mass of the end rigid body. The displacement at any point along the rigid body is computed by replacing e with the proper length from the end of the beam. By solving equation (3.21) for displacement $w_s(1)$ and equation (3.22) for the slope versus the bias voltage V_w, the corresponding displacement-voltage curve is computed and the onset of static instability is identified.

Following the same procedure for the flexural displacement in the sense direction, similar equations are found for the displacement and slope in that direction. Specifically,

$$\begin{aligned}&\Delta^3\left(216e^4+432e^3+360e^2+144e+24\right)v_s(1)^3\\&-\Delta^3\left(-216e^3+360e^2+216e+48\right)v_s(1)^2\\&+\Delta^3\left(54e^2+72e+24\right)v_s(1)=e\,\nu\left(27e^3+54e^2+36e+8\right)V_v^2\end{aligned} \tag{3.23}$$

and

$$\begin{aligned}&\Delta^3\left(72e^4+144e^3+120e^2+48e+8\right)v_s'(1)^3\\&-\Delta^3\left(144e^3+216e^2+120e+24\right)v_s'(1)^2\\&+\Delta^3\left(72e^2+72e+18\right)v_s'(1)=e\,\nu\left(72e^3+108e^2+54e+9\right)V_v^2\end{aligned} \tag{3.24}$$

are solved for the displacement $v_s(1)$ and slope $v_s'(1)$ in the sense direction versus the bias DC voltage. Equations (3.21), (3.22), (3.23) and (3.24) indicate that the static-voltage curve is affected by the eccentricity e and the cross-sectional ratio Δ. The cross-sectional ratio, see equation (2.65), represents the rigidity of beam in each direction and the eccentricity the mass effects on the moment and shear boundary conditions.

Figures 3.1(a)-3.1(f) show the variation in the nondimensional displacement at the center of rigid body versus the bias voltage in the sense and drive directions ($w_c=1$ and $v_c=1$ indicate displacements are equal to the full gap sizes). Dashed and solid lines indicate, unstable and stable static equilibrium positions. Noting that the electrostatic and elastic fields act in opposite directions, the stability of the state is determined by perturbing the state around the equilibrium, expanding

Table 3.1: Basic system specification

L (μm)	b (μm)	b_M (μm)	h (μm)	g_w (μm)	g_v (μm)	E (GPa)	ρ (kg/m^3)	ϵ (F/m)
400	10	10	10	2	2	160	2330	8.854×10^{-12}

the electrostatic force around the equilibrium position, and computing the first-order term in the Taylor's expansion.

The dotted-dashed horizontal lines in Figures 3.1(a)-3.1(f) represent the critical points where the tip of the structure strikes the substrate. To obtain the limit, the displacement at the tip of the structure, that is $w_s(1) + 2\,e\,w_s'(1)$, is set to unity, the dimensional displacement as large as initial gap size, and compute the corresponding voltage. For that voltage, the displacement at the center of mass, w_c, indicates the critical displacement. The specification of the example of the microscale gyroscope is given in Table 3.1.

The static pull-in voltage is the point where there is no solution beyond it. According to the results, the static deflection curves are in the drive and sense direction are affected by the ratio Δ; the larger the cross-sectional ratio Δ is, the larger the static pull-in voltage. On the other hand, eccentricity has an opposite effect on the pull-in voltage. The limit, the horizontal dashed-dot line, appears at a smaller displacement because an increasing eccentricity affects the geometry of the end body as well as the first moment of the end mass.

3.2.2 Modal Frequencies and Mode Shapes

The eigenfunctions (mode shapes) of the beam carrying the eccentric end body are computed for the admissible functions of the assumed-modes method. Therefore, the natural (modal) frequencies of the uncoupled system of equations are determined by obtaining the eigenvalue problem. To this end, dropping damping, linearizing the electrostatic forcing terms around the static equilibrium positions, w_s and v_s, and substituting equation (3.8) into equations (3.1)-(3.7) and considering static equilibrium equations (3.9)-(3.11), the dynamic equations become

$$w_d'''' + \ddot{w}_d - \alpha\,\ddot{w}_d'' = 0 \tag{3.25}$$

with the essential boundary conditions at $\ell = 0$

$$w_d = 0,\; w_d' = 0, \tag{3.26}$$

and natural boundary conditions at $\ell = 1$

$$\Delta w_d'' + \Delta e\; M\left(e\,\ddot{w}_d' + \ddot{w}_d\right) + \Delta J_{\eta\eta}\ddot{w}_d' = \frac{2\,\nu\,e^2\,V_w^2\left(w_d + e\,w_d'\right)}{\left(1 - w_s - e\,w_s'\right)^3} \tag{3.27}$$

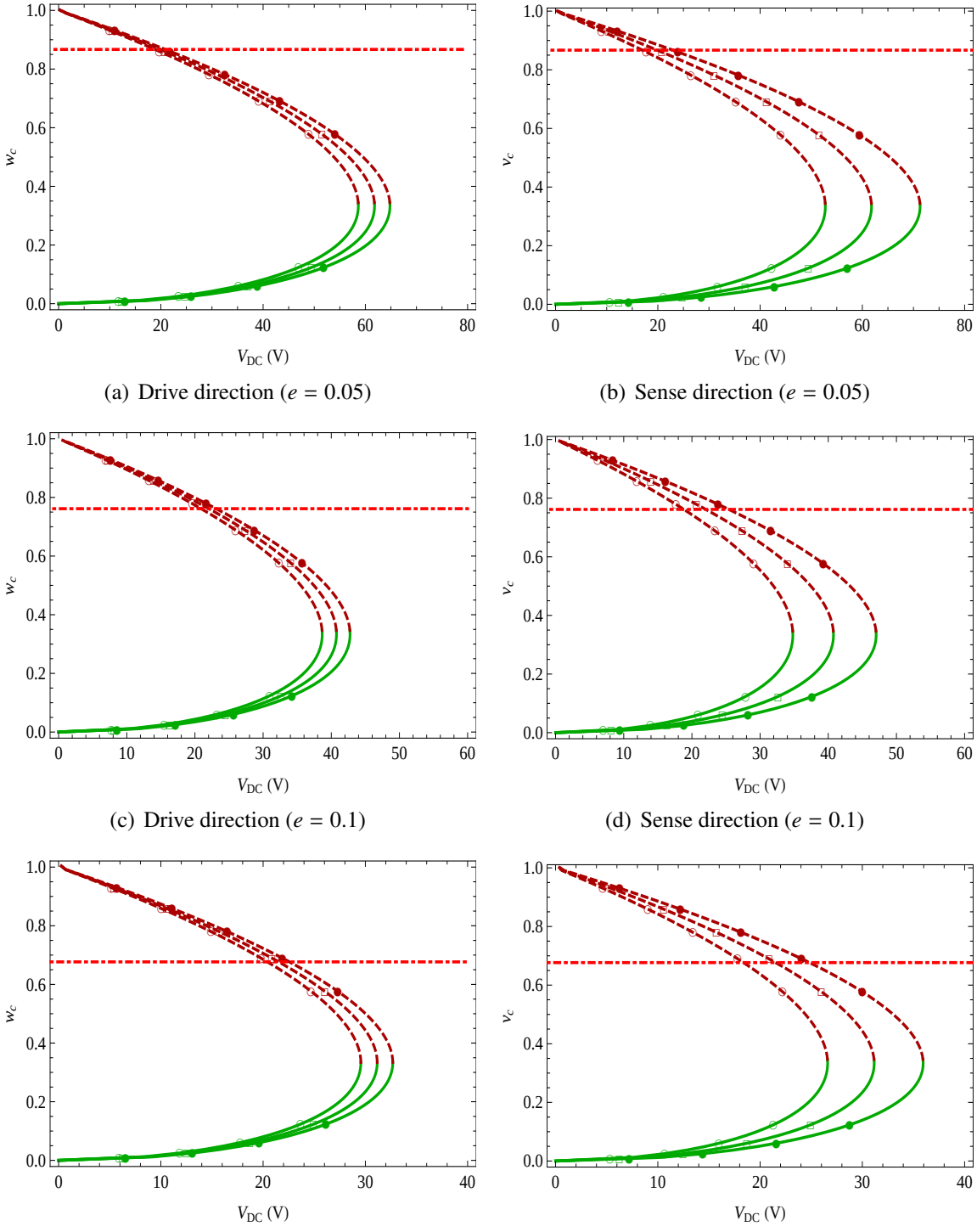

(a) Drive direction ($e = 0.05$)

(b) Sense direction ($e = 0.05$)

(c) Drive direction ($e = 0.1$)

(d) Sense direction ($e = 0.1$)

(e) Drive direction ($e = 0.15$)

(f) Sense direction ($e = 0.15$)

Figure 3.1: Variation in the static displacement at the center of mass of the end rigid body versus the bias DC voltage; $-\circ-$ for $\Delta = 0.9$, and $-\square-$ for $\Delta = 1$, and $-\bullet-$ for $\Delta = 1.1$, the dashed line denotes the unstable branch while the solid line indicates the stable branch of the static equilibrium position.

$$\Delta\, w_d''' \;-\Delta\, M\,\left(\ddot{w}_d + e\,\ddot{w}_d'\right) + \Delta\,\alpha\ddot{w}_d' \;= -\frac{2\,\nu\,e\,V_w^2\left(w_d + e\,w_d'\right)}{\left(1 - w_s - e\,w_s'\right)^3} \tag{3.28}$$

in the drive direction and similarly in the sense direction we have

$$\Delta^2\, v_d'''' \;+ \ddot{v}_d - \alpha\,\Delta^2\,\ddot{v}_d'' = 0, \tag{3.29}$$

with the boundary conditions at $\ell = 0$

$$v_d = 0,\; v_d' = 0, \tag{3.30}$$

and at $\ell = 1$

$$\Delta^3 v_d'' \;+ \Delta e\;M\,\left(e\,\ddot{v}_d' \;+\; \ddot{v}_d\right) + \Delta\, J_{\zeta\zeta}\ddot{v}_d' \;= \frac{2\,\nu\,e^{\,2}\,V_v^2\left(v_d + e\,v_d'\right)}{\left(1 \;- v_s - e\,v_s'\right)^3}, \tag{3.31}$$

$$\Delta^3\, v_d''' - \Delta\, M\,\left(\ddot{v}_d \;+ e\,\ddot{v}_d'\right) - \alpha\,\Delta^3\,\ddot{v}_d' = -\frac{2\,\nu\,e\,V_v^2\left(v_d + e\,v_d'\right)}{\left(1 - v_s - e\,v_s'\right)^3} \tag{3.32}$$

in the sense direction. Assuming solutions of the form

$$w_d(\ell, t) = \psi(\ell)\exp^{i\omega_w t},\; v_d(\ell, t) = \phi(\ell)\exp^{i\omega_v t} \tag{3.33}$$

for equations (3.26)-(3.32), results in the following uncoupled eigenvalue problems

$$\psi^{(4)}(\ell) - \omega_w^2\psi(\ell) + \alpha\omega_w^2\psi''(\ell) = 0, \tag{3.34}$$

$$\begin{aligned}
&\psi(0) = 0,\\
&\psi'(0) = 0,\\
&\Delta\psi''(1) - e\,\Delta\,M\,\omega_w^2\,\left(\psi(1) + e\psi'(1)\right) - \Delta J_{22}\omega_w^2\psi'(1) = \frac{2\nu e^2\,\left(\psi(1) + e\psi'(1)\right)\,V_w^2}{\left(1 - ew_s'(1) - w_s(1)\right)^3},\\
&\Delta\psi^{(3)}(1) + \Delta\,M\,\omega_w^2\,\left(\psi(1) + e\psi'(1)\right) + \alpha\Delta\omega_w^2\psi'(1) = -\frac{2\nu e\,\left(\psi(1) + e\psi'(1)\right)\,V_w^2}{\left(1 - ew_s'(1) - w_s(1)\right)^3}
\end{aligned} \tag{3.35}$$

for the drive direction and

$$\Delta^2\phi^{(4)}(\ell) - \omega_v^2\phi(\ell) + \alpha\Delta^2\omega_v^2\phi''(\ell) = 0, \tag{3.36}$$

$$\phi(0) = 0,$$
$$\phi'(0) = 0,$$
$$\Delta^3\phi''(1) - e\,\Delta\,M\,\omega_v^2\left(\phi(1) + e\phi'(1)\right) - \Delta J_{33}\omega_v^2\phi'(1) = \frac{2\nu e^2\left(\phi(1) + e\phi'(1)\right)V_v^2}{\left(1 - ev_s'(1) - v_s(1)\right)^3},$$
$$\Delta^3\phi^{(3)}(1) + \Delta\,M\,\omega_v^2\left(\phi(1) + e\phi'(1)\right) + \alpha\Delta^3\omega_v^2\phi'(1) = -\frac{2\nu e\left(\phi(1) + e\phi'(1)\right)V_v^2}{\left(1 - ev_s'(1) - v_s(1)\right)^3} \tag{3.37}$$

for the sense direction. Following the standard procedure of solving an eigenvalue problem, the characteristic equations are obtained and solved for the modal frequencies ω_v and ω_w. Solutions of equations (3.34) and (3.36) are given by

$$\psi(\ell) = A_1 \sin\lambda_w^+ + A_2\cos\lambda_w^+ + A_3\sinh\lambda_w^- + A_4\cosh\lambda_w^- \tag{3.38}$$

where

$$\lambda_w^+ = \ell\sqrt{\left(\omega_w\sqrt{\alpha^2\omega_w^2 + 4} + \alpha\omega_w^2\right)/2},\ \text{and}\ \lambda_w^- = \ell\sqrt{\left(\omega_w\sqrt{\alpha^2\omega_w^2 + 4} - \alpha\omega_w^2\right)/2}$$

and

$$\phi(\ell) = B_1 \sin\lambda_v^+ + B_2\cos\lambda_v^+ + B_3\sinh\lambda_v^- + B_4\cosh\lambda_v^- \tag{3.39}$$

where

$$\lambda_v^+ = \ell\sqrt{\left(\omega_v\sqrt{\alpha^2\Delta^2\omega_v^2 + 4} + \alpha\Delta\omega_v^2\right)/(2\Delta)},\ \text{and}\ \lambda_v^+ = \ell\sqrt{\left(\omega_v\sqrt{\alpha^2\Delta^2\omega_v^2 + 4} - \alpha\Delta\omega_v^2\right)/(2\Delta)}$$

Applying the boundary conditions in the equation (3.35) to the general solution in equation (3.38), a system of four homogeneous equations are obtained. To find nontrivial solutions of that system of equations, the determinant of the coefficients matrix is set to zero. As a result the characteristic equation is obtained and solved for the natural frequencies ω_w. Similarly, the natural frequencies in the transverse direction, ω_v, are obtained.

In Figures 3.2(a)-3.2(f), the fundamental (first) natural frequency of the uncoupled system is plotted. The natural frequency is affected by both the distance of beam's free end from the center of the rigid body and the ratio of beam's thickness to width Δ. The voltages V_w and V_v are increased up to the onset of pull-in where the DC voltages suddenly drop to zero as the rigid body strikes the electrode. Increasing the eccentricity, reduces the natural frequency by virtue of increasing the first and second moment of end mass, that is $e\,M$ and $e^2\,M$. The ratio of cross-section Δ changes the elastic rigidity and therefore increases or decreases the natural frequency. The sectional ratio Δ appears in linear and cubic forms in the drive and sense directions, equations (3.25)-(3.28) and (3.29)-(3.32), and distinguishes the frequency-voltage curves in Figures 3.2(a)-3.2(f).

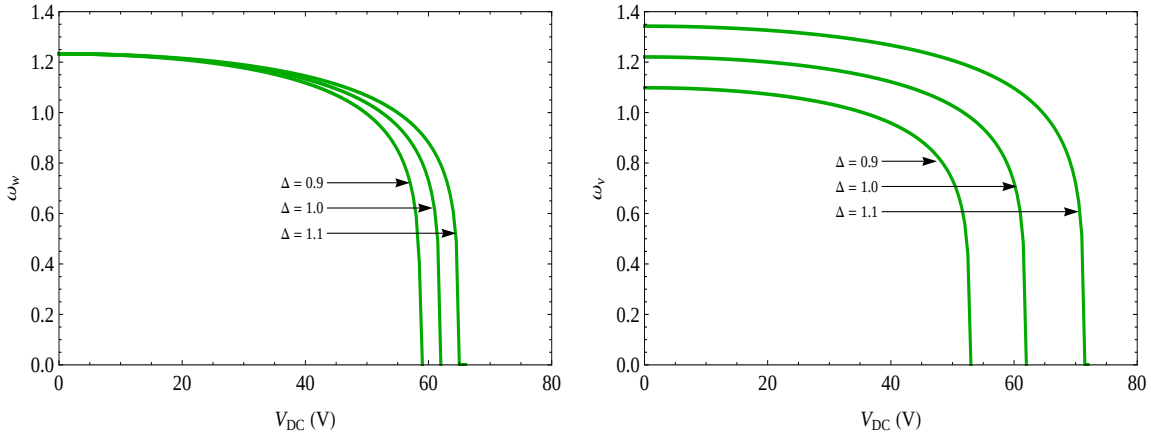

(a) Drive direction (e = 0.05)

(b) Sense direction (e = 0.05)

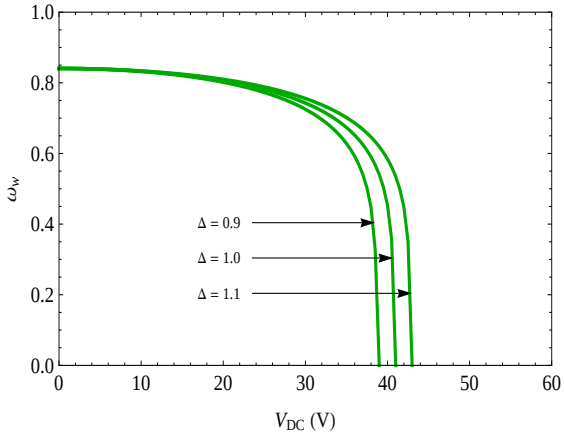

(c) Drive direction (e = 0.1)

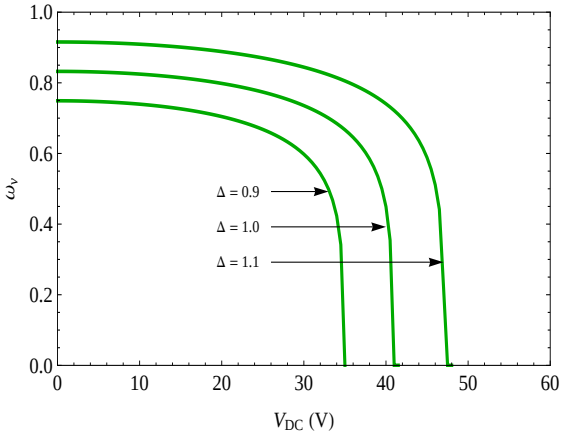

(d) Sense direction (e = 0.1)

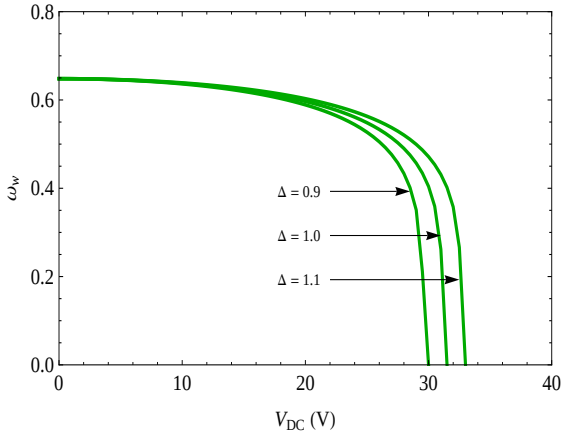

(e) Drive direction (e = 0.15)

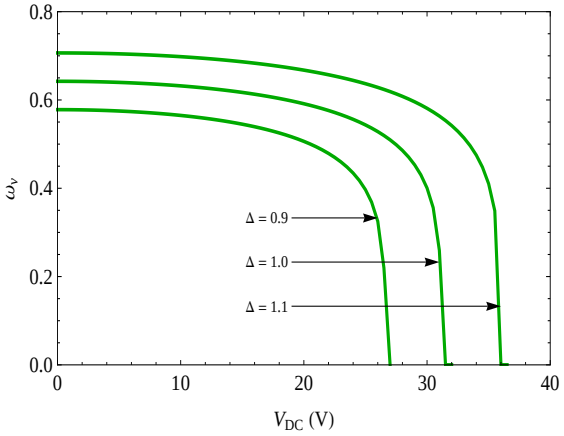

(f) Sense direction (e = 0.15)

Figure 3.2: Variation in the first natural frequency of the uncoupled system in the drive and sense directions versus the bias DC voltage as the eccentricity e and the cross-sectional ratio Δ increase.

To use the assumed-mode method for the analysis of beam-rigid body gyroscope, the mode shapes of (eigenfunctions) of the uncoupled system of equations are obtained. To this end, the bias DC loadings in equations (3.35) and (3.37) are set to zero, and the natural frequencies are obtained. Applying boundary conditions, that is equations (3.35) and (3.37), unknown coefficients A_i and B_i, $i = 1, 2, 3, 4$, are determined. Eigenfunctions are normalized such that $\int_0^1 \psi(\ell)^2 \, \mathrm{d}\ell = 1$ and $\int_0^1 \phi(\ell)^2 \, \mathrm{d}\ell = 1$. Normalized mode shapes are used as the basis functions in the assumed-mode method to obtain the reduced-order model of the system.

3.3 The Analysis of Beam-Rigid Body Gyroscope

3.3.1 Stationary Analysis

Two approaches are followed to investigate the stationary behavior of the beam-rigid body gyroscope. In the first method, the stationary problem is derived from the equations of motion (2.67) and (2.68) and boundary conditions (2.69)-(2.73). Therefore, substituting $w(\ell, t) = w_s(\ell) + w_d(\ell, t)$ into (2.67) and eliminating dynamic terms results in

$$w_s{}^{(4)}(\ell) - \Omega^2 \left(\alpha w_s''(\ell) + w_s(\ell) \right) = 0 \tag{3.40}$$

subject to

$$\begin{aligned}
&w_s(0) = 0, \\
&w_s'(0) = 0, \\
&\Delta w_s''(1) - e\,\Delta\, M\,\Omega^2 \left(w_s(1) + e w_s'(1) \right) + \Delta\Omega^2 \left(J_{11} - J_{33} \right) w_s'(1) = \frac{\nu\, e^2\, V_w^2}{\left(1 - w_s(1) - e w_s'(1) \right)^2}, \\
&\Delta w_s{}^{(3)}(1) + \Delta\Omega^2 (eM - \alpha) w_s'(1) + \Delta M \Omega^2 w_s(1) = -\frac{\nu\, e\, V_w^2}{\left(1 - w_s(1) - e w_s'(1) \right)^2},
\end{aligned} \tag{3.41}$$

and

$$\Delta^2 v_s{}^{(4)}(\ell) - \Omega^2 \left(\alpha \Delta^2 v_s''(\ell) + v_s(\ell) \right) = 0 \tag{3.42}$$

subject to

$$\begin{aligned}
&v_s(0) = 0, \\
&v_s'(0) = 0, \\
&\Delta^3 v_s''(1) - e\,\Delta\, M\,\Omega^2 \left(v_s(1) + e v_s'(1) \right) + \Delta\Omega^2 \left(J_{11} - J_{22} \right) v_s'(1) = \frac{\nu\, e^2\, V_v^2}{\left(1 - v_s(1) - e v_s'(1) \right)^2}, \\
&\Delta^3 v_s{}^{(3)}(1) + \Omega^2 v_s'(1) \left(\Delta e M - \alpha \Delta^3 \right) + \Delta M \Omega^2 v_s(1) = -\frac{\nu\, e\, V_v^2}{\left(1 - v_s(1) - e v_s'(1) \right)^2}
\end{aligned} \tag{3.43}$$

Table 3.2: Pull-in voltages for increasing angular rotation rate

$\Omega =$	18°/s	180°/s	1800°/s	18000°/s	180000°/s
$V_{\mathrm{P}} =$	40.7649 V	40.7649 V	40.7649 V	40.7648 V	40.7531 V

By solving equations (3.40) and (3.42) subject to (3.41) and (3.43), the exact static equilibrium position in the drive and sense directions are computed. Alternately, the equations of reduced-order model (2.75) and (2.76) are used to derive the single-mode approximation of the stationary system of equations. To this end, the response of the system in each direction is described with

$$q(t) = q_s + q_d(t), \quad \text{and} \quad p(t) = p_s + p_d(t) \tag{3.44}$$

where the mode shapes, $\psi(\ell)$ and $\phi(\ell)$ were computed in the preceding section, and the generalized static and dynamic coordinates of the structures' response in the drive and sense directions are represented by q_s, $q_d(t)$, p_s, and $p_d(t)$. Inserting equations (3.44) in (2.75) and (2.76) and separating the dynamic and static components of the results in the following static equations

$$\begin{aligned} &\Delta\Gamma'' q_s + \Delta\Omega^2 \Big(\alpha\Gamma' - \Gamma - M\left(e\psi'(1) + \psi(1)\right)^2 + \psi'(1)^2 \left(J_{\xi\xi} - J_{\zeta\zeta}\right)\Big) q_s \\ &\qquad = \frac{\nu\, e\, V_w^2 \left(\psi(1) + e\,\psi'(1)\right)}{\Big(1 - \left(\psi(1) - e\psi'(1)\right) q_s\Big)^2} \end{aligned} \tag{3.45}$$

$$\begin{aligned} &\Delta^3\Lambda'' p_s + \Delta\Omega^2 \Big(\alpha\Delta^2\Lambda' - \Lambda - M\left(e\phi'(1) + \phi(1)\right)^2 + \phi'(1)^2 \left(J_{\xi\xi} - J_{\eta\eta}\right)\Big) p_s \\ &\qquad = \frac{\nu\, e\, V_v^2 \left(\phi(1) + e\,\phi'(1)\right)}{\Big(1 - \left(\phi(1) - e\phi'(1)\right) p_s\Big)^2} \end{aligned} \tag{3.46}$$

where the total displacement is computed from

$$w(\ell, t) = \left(q_s + q_d(t)\right)\psi(\ell), \quad \text{and} \quad v(\ell, t) = \left(p_s + p_d(t)\right)\phi(\ell), \tag{3.47}$$

To compute static displacement, $q_d(t)$ and $p_d(t)$ are set to zero. By computing the stationary response using equations (3.40)-(3.43) and equations (3.45) and (3.46) the accuracy of a single-mode approximation and the effect of angular rotation rate Ω on the stationary response are determined.

For the micro-scale numerical example of Table 3.1, the results of the stationary analysis are plotted in Figures 3.3(a)-3.3(d). The rotation rate Ω is increased up to 18000°/s. It is realized that the single-mode approximation fully agrees with the exact analysis up to $\Omega = 180000$°/s. In Table 3.1, the stationary pull-in voltages are given for an increasing angular rotation rate up to 180000°/s. All desired applications of micro- and nano-gyroscopes cover an input rate of less than 180000°/s or 500 cycles per second.

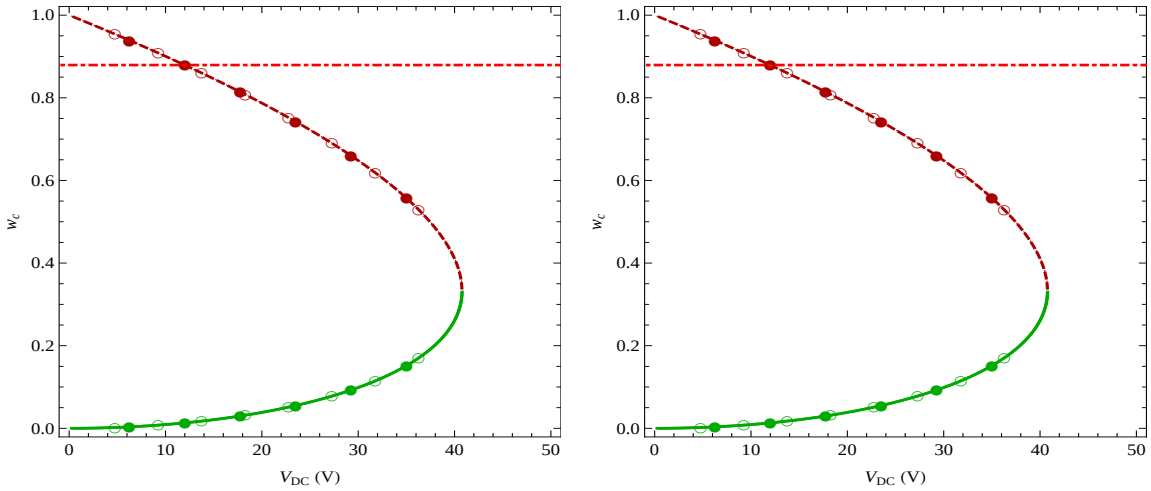

(a) $\Omega = 18°/s$ (b) $\Omega = 180°/s$

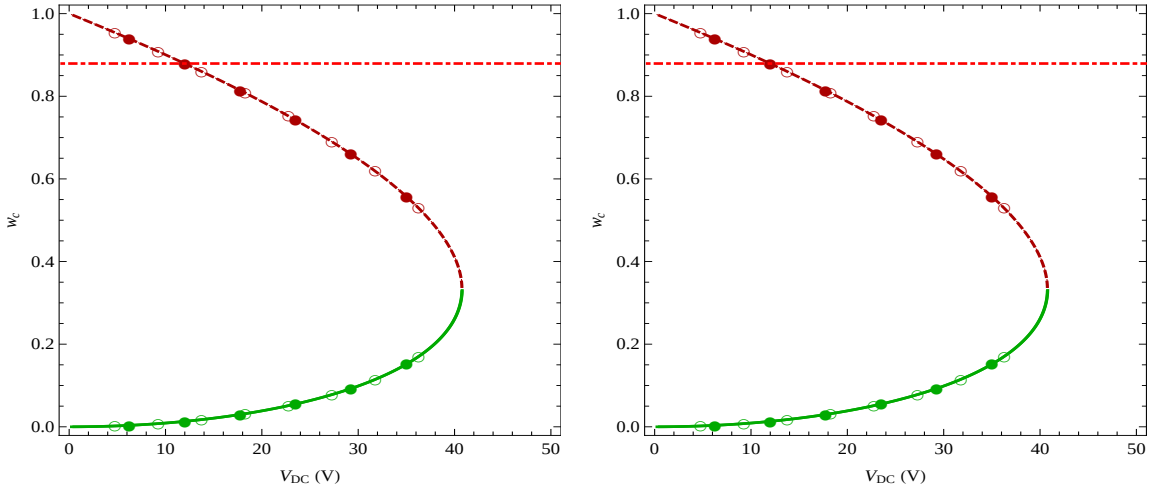

(c) $\Omega = 1800°/s$ (d) $\Omega = 18000°/s$

Figure 3.3: Stationary analysis of the beam-rigid body microgyroscope, filled circles indicate the exact solution and circles represent the solution of the single-mode model ($e = 0.1$, $\frac{a_M}{a_B} = 15$, $V_{\text{DC}} = V_w$).

3.3.2 Modal Frequencies

To calculate the angular rotation rate using the natural frequencies of the system in the rotating frame, modal frequencies are computed in this section. Results of this analysis are used to compute the input angular rotation rate employing the frequency modulation method. The frequency modulation method can be used by employing either the free vibration or the forced vibration of the structure. In the following sections, the free vibration of the structure is characterized to demonstrate the method for the beam-rigid body gyroscope. Therefore, for beam-mass gyroscopes the

same approach is applicable to compute the angular rate of rotation based on the modal frequency split in the rotating frame.

3.3.3 Undamped Modal Frequencies

Substituting equations (3.44) into (2.75) and (2.76), separating the dynamic and static components of the results, dropping the terms associated with damping coefficients, linearizing the equations about the static modal coordinates q_s and p_s, and using equations (3.45) and (3.46), gives the following dynamic equations

$$\begin{aligned}
&\Delta\left(\alpha\Gamma' + \Gamma + M\left(e\psi'(1) + \psi(1)\right)^2 + J_{\eta\eta}\psi'(1)^2\right)\ddot{q}_d(t) \\
&+ \Delta\Omega\left(2M\left(e\psi'(1) + \psi(1)\right)\left(e\phi'(1) + \phi(1)\right) + \psi'(1)\phi'(1)\left(J_{\zeta\zeta} + J_{\eta\eta} - J_{\xi\xi}\right) + 2\Pi\right)\dot{p}_d(t) \\
&+ \Delta\left(\Gamma'' + \Omega^2\left(\alpha\Gamma' - \Gamma - M\left(e\psi'(1) + \psi(1)\right)^2 + \psi'(1)^2\left(J_{\xi\xi} - J_{\zeta\zeta}\right)\right)\right)q_d(t) \\
&= \frac{2\,e\,\nu\,\left(e\psi'(1) + \psi(1)\right)^2\,V_w^2}{\left(1 - q_s\left(\psi(1) + e\psi'(1)\right)\right)^3}q_d(t)
\end{aligned} \tag{3.48}$$

and

$$\begin{aligned}
&\Delta\left(\alpha\Delta^2\Lambda' + \left(M\left(e\phi'(1) + \phi(1)\right)^2 + J_{\zeta\zeta}\phi'(1)^2 + \Lambda\right)\right)\ddot{p}_d(t) \\
&- \Delta\Omega\left(2M\left(e\psi'(1) + \psi(1)\right)\left(e\phi'(1) + \phi(1)\right) + \psi'(1)\phi'(1)\left(J_{\zeta\zeta} + J_{\eta\eta} - J_{\xi\xi}\right) + 2\Pi\right)\dot{q}_d(t) \\
&+ \left(\Delta^3\left(\alpha\Omega^2\Lambda' + \Lambda''\right) + \Delta\Omega^2\left(-M\left(e\phi'(1) + \phi(1)\right)^2 + \phi'(1)^2\left(J_{\xi\xi} - J_{\eta\eta}\right) - \Lambda\right)\right)p_d(t) \\
&= \frac{2\,e\,\nu\,\left(e\phi'(1) + \phi(1)\right)^2\,V_v^2}{\left(1 - p_s\left(\phi(1) + e\phi'(1)\right)\right)^3}p_d(t)
\end{aligned} \tag{3.49}$$

Alternatively, substituting the response in the form

$$w(\ell, t) \;=\; w_s(\ell) + \;\psi(\ell)\,q_d(t), \quad v(\ell, t) \;=\; v_s(\ell) + \;\phi(\ell)\,p_d(t) \tag{3.50}$$

into equations (2.75) and (2.76) results in

$$\begin{aligned}
&\left(\Gamma \;+ \alpha\,\Gamma' \;+ M\left(\psi(1) + e\,\psi'(1)\right)^2 + J_{22}\psi'(1)^2\right)\ddot{q}_d(t) \\
&+ \left(2\,\Pi + 2M\left(\phi(1) + e\,\phi'(1)\right)\left(\psi(1) + e\,\psi'(1)\right) - \left(J_{11} - J_{22} - J_{33}\right)\phi'(1)\psi'(1)\right)\Omega\dot{p}_d(t) \\
&+ \left(\Gamma'' \;- \Omega^2\left(\Gamma \;- \alpha\Gamma'\right) - M\Omega^2\left(\psi(1) + e\,\psi'(1)\right)^2 + J_{11}\Omega^2\psi'(1)^2 - J_{33}\Omega^2\psi'(1)^2\right)q_d(t) = \\
&- \int_0^1 w_s''(\xi)\psi''(\xi)\;\mathrm{d}\xi + \Omega^2\left(\int_0^1 w_s(\xi)\psi(\xi)\;\mathrm{d}\xi - \alpha\int_0^1 w_s'(\xi)\psi'(\xi)\;\mathrm{d}\xi\right)
\end{aligned}$$

$$+ M\Omega^2\left(w_s(1) + e\,w_s'(1)\right)\psi(1) - \left(e\,M\left(w_s(1) + e\,w_s'(1)\right) - (J_{11} - J_{33})\;w_s'(1)\right)\psi'(1)\Omega^2$$
$$+ \frac{e\,\nu\,V_w^2\;(\psi(1) + e\,\psi'(1))}{\left(1 - w_s(1) - e\,w_s'(1)\right)^2} + \frac{2\,\nu\,e\,V_w^2\,(\psi(1) + e\,\psi'(1))^2}{\left(1 - w_s(1) - e\,w_s'(1)\right)^3} q_d(t) \tag{3.51}$$

and

$$\left(\Lambda\; + \alpha\,\Lambda'\; + M\,(\phi(1) + e\,\phi'(1))^2 + J_{33}\phi'(1)^2\right)\ddot{p}_d(t)$$
$$- \left(2\,\Pi + 2\,M\,(\phi(1) + e\,\phi'(1))\,(\psi(1) + e\,\psi'(1)) - (J_{11} - J_{22} - J_{33})\,\phi'(1)\psi'(1)\right)\Omega\,\dot{q}_d(t)$$
$$+ \left(\Lambda''\; + \Omega^2\;(\alpha\,\Lambda'\; -\; \Lambda) - M\Omega^2\,(\phi(1) + e\,\phi'(1))^2 + J_{11}\Omega^2\phi'(1)^2 - J_{22}\Omega^2\phi'(1)^2\right)p_d(t) =$$
$$- \int_0^1 v_s''(\hat{\xi})\phi''(\xi)\;\mathrm{d}\xi + \Omega^2\left(\int_0^1 v_s(\xi)\phi(\xi)\;\mathrm{d}\xi - \alpha\;\int_0^1 v_s'(\xi)\phi'(\xi)\;\mathrm{d}\xi\right)$$
$$+ M\,\Omega^2\left(v_s(1) + e\,v_s'(1)\right)\phi(1) + \Omega^2\left(eM\left(v_s(1) + e\,v_s'(1)\right) - J_{11}v_s'(1) + J_{22}\,v_s'(1)\right)\phi'(1)$$
$$+ \frac{e\,\nu\,V_v^2}{\left(1 - v_s(1) - ev_s'(1)\right)^2}\,(\phi(1) + e\phi'(1)) + \frac{2\,e\,\nu\,V_v^2\,(\phi(1) +\; e\,\phi'(1))^2}{\left(1 - v_s(1) -\; e\,v_s'(1)\right)^3} p_d(t) \tag{3.52}$$

which are computationally more demanding but are equivalent to equations (3.48) and (3.49). Equations (3.48) and (3.49) are employed to derive the characteristic equation of the system. The bias DC voltage is removed and therefore the static deflections are set to zero to compute the fundamental natural frequency of the structure about the undeformed position. To this end it is assumed that

$$q_d(t) \;=\; s\,e^{\lambda t},\;\text{ and }\;p_d(t) \;=\; r\,e^{\lambda t} \tag{3.53}$$

where s, r, and λ indicate the eigenvectors and the eigenvalue. Substituting equation (3.53) into equations (3.48) and (3.49), multiplying through by $e^{-\lambda t}$ and collecting eigenvectors, s and r, a system of homogeneous equations is obtained. To compute nontrivial eigenvalues, λ, the determinant of the coefficient matrix is set to zero and the characteristic equation for the undamped unloaded system is computed as follows:

$$h_4\,\lambda^4 \;+\; h_2\,\lambda^2 \;+\; c_4\,\Omega^4 \;+\; c_2\,\Omega^2 \;+\; c_0 = 0 \tag{3.54}$$

where

$$h_4 \;= \Delta^2\left(\alpha\Gamma' + \Gamma + M\,(e\psi'(1) + \psi(1))^2 + J_{\eta\eta}\psi'(1)^2\right)\left(\alpha\Delta^2\Lambda' + M\,(e\phi'(1) + \phi(1))^2 + J_{\zeta\zeta}\phi'(1)^2 + \Lambda\right) \tag{3.55}$$

$$h_2 \;= \Delta^2\Gamma''\left(\alpha\Delta^2\Lambda' + M\,(e\phi'(1) + \phi(1))^2 + J_{\zeta\zeta}\phi'(1)^2 + \Lambda\right)$$
$$+ \Delta^4\Lambda''\left(\alpha\Gamma' + \Gamma + M\,(e\psi'(1) + \psi(1))^2 + J_{\eta\eta}\psi'(1)^2\right)$$

$$
\begin{aligned}
&+\Delta^2\Omega^2\left(-\left(-\alpha\Gamma'+\Gamma+M\left(e\psi'(1)+\psi(1)\right)^2+\psi'(1)^2\left(J_{\zeta\zeta}-J_{\xi\xi}\right)\right)\right.\\
&\left(\alpha\Delta^2\Lambda'+M\left(e\phi'(1)+\phi(1)\right)^2+J_{\zeta\zeta}\phi'(1)^2+\Lambda\right)\\
&-\left(\alpha\Gamma'+\Gamma+M\left(e\psi'(1)+\psi(1)\right)^2+J_{\eta\eta}\psi'(1)^2\right)\\
&\left(-\alpha\Delta^2\Lambda'+M\left(e\phi'(1)+\phi(1)\right)^2+\phi'(1)^2\left(J_{\eta\eta}-J_{\xi\xi}\right)+\Lambda\right)\\
&\left.+\left(2M\left(e\psi'(1)+\psi(1)\right)\left(e\phi'(1)+\phi(1)\right)+\psi'(1)\phi'(1)\left(J_{\zeta\zeta}+J_{\eta\eta}-J_{\xi\xi}\right)+2\Pi\right)^2\right) \qquad (3.56)
\end{aligned}
$$

$$
\begin{aligned}
c_4 =&\ \Delta^2\left(-\alpha\Gamma'+\Gamma+M\left(e\psi'(1)+\psi(1)\right)^2+\psi'(1)^2\left(J_{\zeta\zeta}-J_{\xi\xi}\right)\right)\\
&\left(-\alpha\Delta^2\Lambda'+M\left(e\phi'(1)+\phi(1)\right)^2+\phi'(1)^2\left(J_{\eta\eta}-J_{\xi\xi}\right)+\Lambda\right) \qquad (3.57)
\end{aligned}
$$

$$
\begin{aligned}
c_2 =&\ \Delta^2\Gamma''\left(\alpha\Delta^2\Lambda'-M\left(e\phi'(1)+\phi(1)\right)^2+\phi'(1)^2\left(J_{\xi\xi}-J_{\eta\eta}\right)-\Lambda\right)\\
&-\Delta^4\Lambda''\left(-\alpha\Gamma'+\Gamma+M\left(e\psi'(1)+\psi(1)\right)^2+\psi'(1)^2\left(J_{\zeta\zeta}-J_{\xi\xi}\right)\right) \qquad (3.58)
\end{aligned}
$$

$$
c_0 = \Delta^4\Gamma''\Lambda'' \qquad (3.59)
$$

where h_4, h_2, c_4, c_2 and c_0 are functions of the dimensions, system parameters and mode shapes, ϕ and ψ, of the uncoupled governing equations of motion ($\Omega = 0$). Solving equation (3.54) for λ computes the undamped eigenvalues or natural frequencies of the system in the rotating base frame.

In Figures 3.4(a)-3.4(f) the eigenfrequencies are plotted as the rotation increases from zero to 36000°/s or 100 revolutions per second (100Hz) for the micro-scale numerical example of Table 3.1 with $\Delta = 1$. The width ratio represents the ratio of the rigid body's width to the beam's and the nondimensional eccentricity is given in equation (2.64). In agreement with previous analyses in section 3.2, increasing the eccentricity decreases the fundamental natural frequency in each direction identified by the initial mismatch of natural frequencies for $\Omega = 0$ (uncoupled system). On the other hand, by reducing the width of the end rigid body, a stronger symmetry in the microstructure results in the lower initial mismatch of uncoupled natural frequencies.

A very high angular rotation rate is not common; however, if it occurs, an extremely large rotation rate affects the stability of the system. Solving equation (3.54) for eigenvalues, it is realized that one root squared is negative while the other one is positive when

$$
c_4\Omega^4 + c_2\Omega^2 + c_0 < 0 \qquad (3.60)
$$

For instance if $\lambda_1^2 > 0$, then λ_1^+ is positive while λ_1^- is negative. A positive real root indicates the instability of the system. Otherwise, that is if Ω never satisfies equation (3.60), system never experiences instability by virtue of rotation rate. The onset of instability is obtained by solving

inequality in equation (3.60) when the left hand side evaluates to zero, therefore

$$\Omega = \left| \sqrt{-\frac{c_2 + \sqrt{c_2^2 - 4c_0c_4}}{2c_4}} \right|, \text{ and } \Omega = \left| \sqrt{\frac{\sqrt{c_2^2 - 4c_0c_4} - c_2}{2c_4}} \right| \tag{3.61}$$

where $|\cdot|$ gives the positive root and coefficients are given in equations (3.57)-(3.59). Therefore, for the rotation rates between two roots in equation (3.61), the vibration amplitude becomes large and the system becomes unstable. However, for the rotation rate gyroscopic sensors the input angular rotation rate is normally several orders of magnitude smaller than the onset of instability. To indicate the instability region, the rotation rate is increased to 10800000°/s and the modal frequencies are plotted in Figure 3.5(a). The instability region is identified by following the real positive eigenvalue, Figure 3.5(d). As a result, the response grows unboundedly while the rotation rate lies in the critical range.

Modal frequencies, roots of equation (3.54), are the natural frequencies in the rotating frame attached to the base coordinate system, see Figure 2.1. Relative to the inertial frame, the base frame rotates with the angular velocity Ω, thus the absolute position of each point is given by

$$\tilde{w} = w\cos\Omega t + v\sin\Omega t \tag{3.62}$$

$$\tilde{v} = -w\sin\Omega t + v\cos\Omega t \tag{3.63}$$

Substituting the free vibration solution, equation (3.53), into equation (3.62) and performing some algebraic manipulations, the pseudo-modal frequencies, the free vibration frequencies in the inertial frame, computes to $\lambda \pm \Omega$.

3.3.4 The Computation of Angular Rotation Rate

In an amplitude modulation (AM) gyroscope, the amplitude of vibration in the sense direction is employed to measure angular rotation rate. The presented beam-based gyroscope can operate in the frequency modulation (FM) mode. To operate in an FM based approach, the characteristic of the gyroscopic system in changing the observed modal frequencies in the rotating frame is used. To this end, equation (3.54) is solved for the modal frequencies which are the positive roots of the equation. Therefore,

$$\lambda_{1,1} = \sqrt{\frac{h_2 - \sqrt{h_2^2 - 4h_4\left(c_4\,\Omega^4 + c_2\,\Omega^2 + c_0\right)}}{2\,h_4}}, \tag{3.64}$$

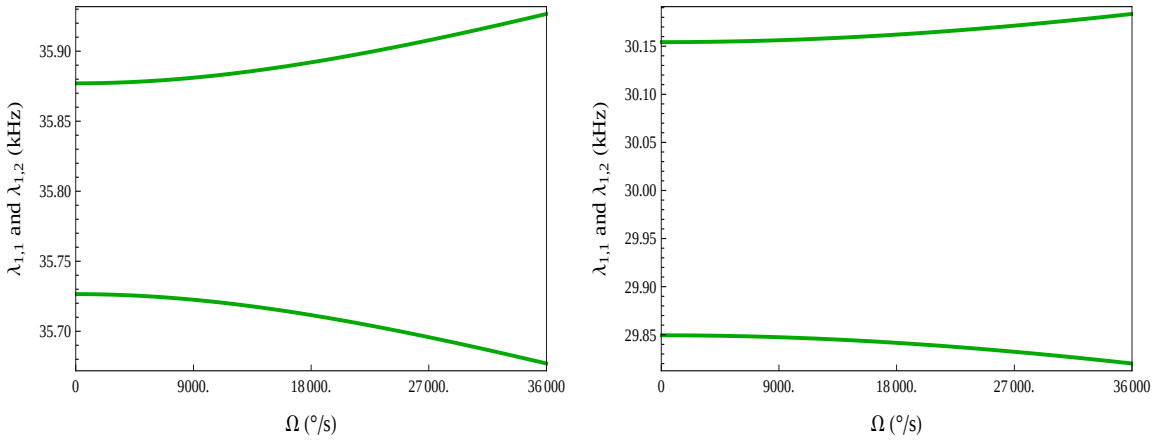

(a) $e = 0.05$ and $\frac{a_M}{a_B} = 10$

(b) $e = 0.05$ and $\frac{a_M}{a_B} = 15$

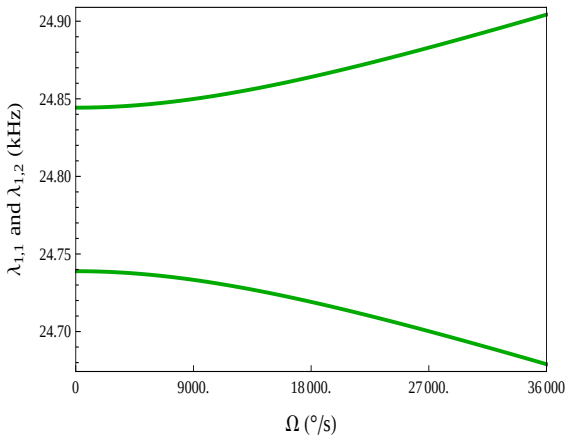

(c) $e = 0.1$ and $\frac{a_M}{a_B} = 10$

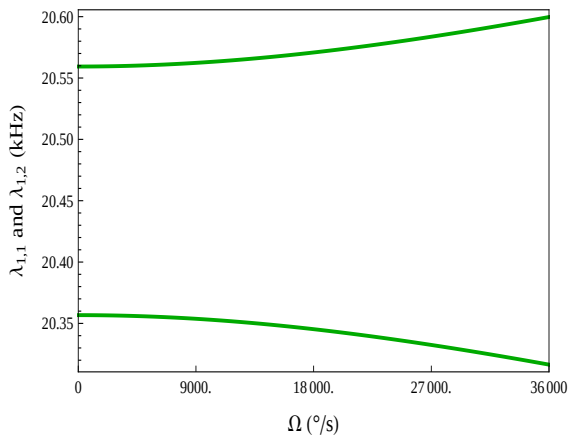

(d) $e = 0.1$ and $\frac{a_M}{a_B} = 15$

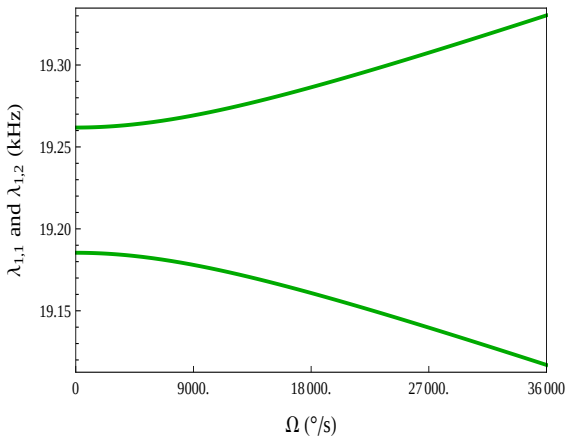

(e) $e = 0.15$ and $\frac{a_M}{a_B} = 10$

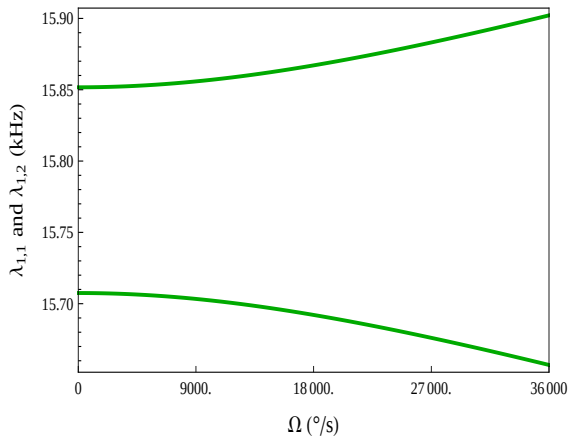

(f) $e = 0.15$ and $\frac{a_M}{a_B} = 15$

Figure 3.4: The variation in the modal frequencies in the rotating frame for the variation in the width ratio and the eccentricity ($\Delta = 1$, $V_w = 0$, $V_v = 0$).

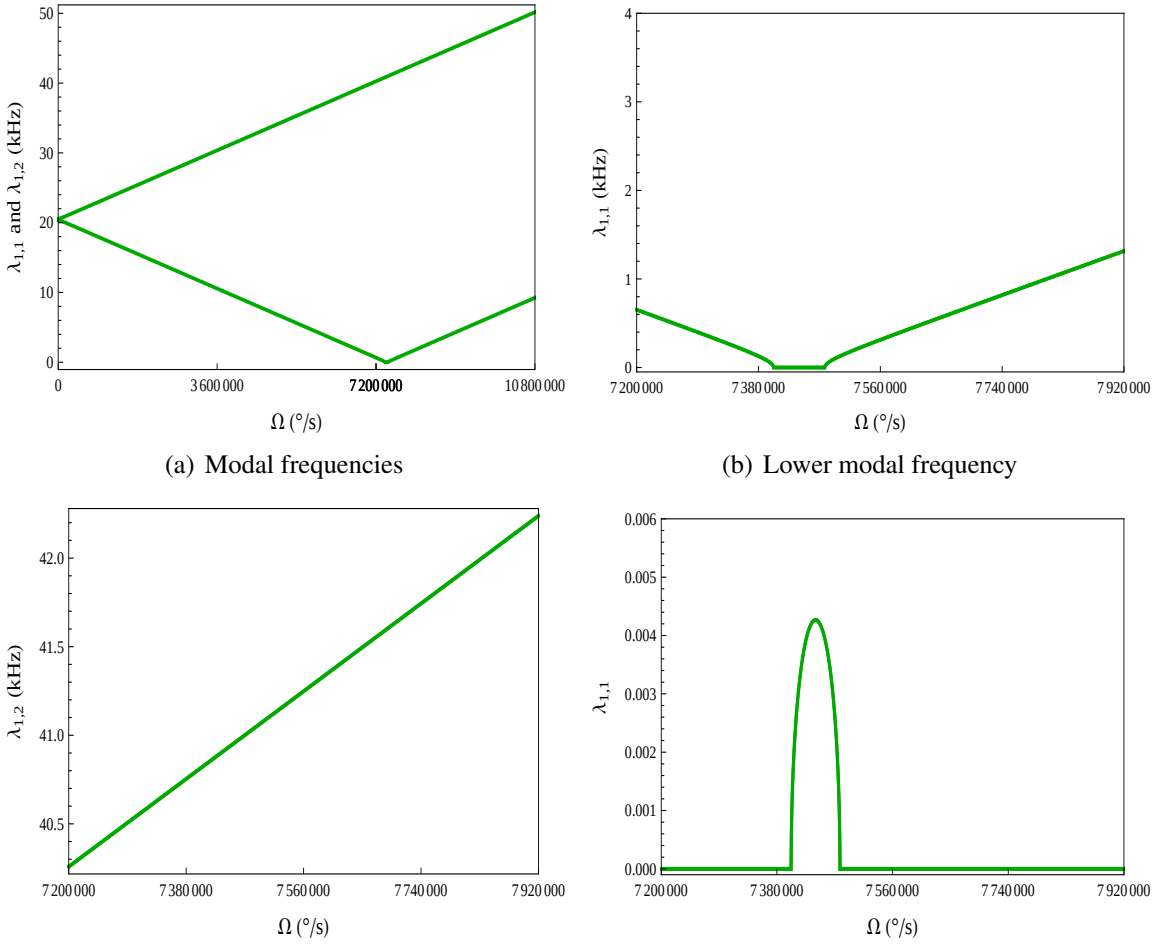

(a) Modal frequencies

(b) Lower modal frequency

(c) Higher modal frequency

(d) Eigenvalue

Figure 3.5: The variation in the eigenvalues for $e = 0.1$, $\frac{a_M}{a_B} = 15$, and $\Delta = 1$ in the rotating frame and the corresponding instability region due to rotation rate ($V_w = 0$, $V_v = 0$).

and

$$\lambda_{1,2} = \sqrt{\frac{h_2 + \sqrt{h_2^2 - 4h_4\left(c_4\Omega^4 + c_2\Omega^2 + c_0\right)}}{2\,h_4}} \tag{3.65}$$

Solving equations (3.64) and (3.65) for the rotation rate Ω and using equations (3.55)-(3.59) results in

$$\Omega = \sqrt{\frac{\beta_3 + \beta_2(\lambda_{1,1} - \lambda_{1,2})^2}{\beta_1} - \frac{1}{2\beta_1\sqrt{\beta_6 + \beta_4(\lambda_{1,1} - \lambda_{1,2})^4 + \beta_5(\lambda_{1,1} - \lambda_{1,2})^2}}} \tag{3.66}$$

where

$$\beta_1 = \Delta^4\left(\beta_{1,6}^4 - 2\beta_{1,3}\beta_{1,5}\beta_{1,6}^2 + 2\beta_{1,2}\beta_{1,7}\beta_{1,6}^2 + \beta_{1,1}^2\beta_{1,2}^2 + \beta_{1,3}^2\beta_{1,5}^2 + 2\beta_{1,1}\beta_{1,2}\beta_{1,3}\beta_{1,4}\right) \tag{3.67}$$

$$\beta_2 = \Delta^4\left(\beta_{1,2}\beta_{1,3}\left(-\beta_{1,1}\beta_{1,2} - \beta_{1,3}\beta_{1,5} + \beta_{1,6}^2\right)\right) \tag{3.68}$$

$$\begin{aligned}\beta_3 =& \Delta^4\left(\beta_{1,5}\beta_{1,3}^2 - \beta_{1,6}^2\beta_{1,3} - \beta_{1,1}\beta_{1,2}\beta_{1,3}\right)\Gamma'' \\ &+ \Delta^4\Lambda''\left(\Delta^2\left(-\beta_{1,2}\right)\beta_{1,6}^2 - \Delta^2\beta_{1,2}\beta_{1,3}\beta_{1,5} - \Delta^2\beta_{1,2}^2\beta_{1,7}\right)\end{aligned} \tag{3.69}$$

$$\beta_4 = -\Delta^8\beta_{1,2}^3\beta_{1,3}^3\beta_{1,5}\beta_{1,7} \tag{3.70}$$

$$\begin{aligned}\beta_5 =& \Delta^8\beta_{1,2}^2\beta_{1,3}^2\left(\beta_{1,2}\beta_{1,1}^2 + \beta_{1,3}\beta_{1,4}\beta_{1,1} + \beta_{1,6}^2\beta_{1,7}\right)\Gamma'' \\ &+ \Delta^8\beta_{1,2}^2\beta_{1,3}^2\Lambda''\left(\Delta^2\beta_{1,3}\beta_{1,5}^2 - \Delta^2\beta_{1,5}\beta_{1,6}^2 + \Delta^2\beta_{1,2}\beta_{1,5}\beta_{1,7}\right)\end{aligned} \tag{3.71}$$

$$\begin{aligned}\beta_6 =& \Delta^{12}\beta_{1,2}^2\beta_{1,3}\beta_{1,5}\beta_{1,6}^2\left(\Lambda''\right)^2 - \Delta^6\beta_{1,2}\beta_{1,3}\beta_{1,6}^2\Gamma''\Lambda''\left(\Delta^4\left(-\beta_{1,6}^2\right) + \Delta^4\beta_{1,3}\beta_{1,5} - \Delta^4\beta_{1,2}\beta_{1,7}\right) \\ &- \Delta^8\beta_{1,2}\beta_{1,3}^2\beta_{1,6}^2\beta_{1,7}\left(\Gamma''\right)^2\end{aligned} \tag{3.72}$$

and the coefficients of equations (3.67)-(3.72) are as follows

$$\beta_{1,1} = -\alpha\Delta^2\Lambda' + M\left(e\phi'(1) + \phi(1)\right)^2 + \phi'(1)^2\left(J_{\eta\eta} - J_{\xi\xi}\right) + \Lambda, \tag{3.73}$$

$$\beta_{1,2} = \alpha\Gamma' + \Gamma + M\left(e\psi'(1) + \psi(1)\right)^2 + J_{\eta\eta}\psi'(1)^2, \tag{3.74}$$

$$\beta_{1,3} = \alpha\Delta^2\Lambda' + M\left(e\phi'(1) + \phi(1)\right)^2 + J_{\zeta\zeta}\phi'(1)^2 + \Lambda, \tag{3.75}$$

$$\beta_{1,4} = \alpha\Gamma' - \Gamma - M\left(e\psi'(1) + \psi(1)\right)^2 + \psi'(1)^2\left(J_{\xi\xi} - J_{\zeta\zeta}\right), \tag{3.76}$$

$$\beta_{1,5} = -\alpha\Gamma' + \Gamma + M\left(e\psi'(1) + \psi(1)\right)^2 + \psi'(1)^2\left(J_{\zeta\zeta} - J_{\xi\xi}\right), \tag{3.77}$$

$$\beta_{1,6} = 2M\left(e\psi'(1) + \psi(1)\right)\left(e\phi'(1) + \phi(1)\right) + \psi'(1)\phi'(1)\left(J_{\zeta\zeta} + J_{\eta\eta} - J_{\xi\xi}\right) + 2\Pi, \tag{3.78}$$

$$\beta_{1,7} = \alpha\Delta^2\Lambda' - M\left(e\phi'(1) + \phi(1)\right)^2 + \phi'(1)^2\left(J_{\xi\xi} - J_{\eta\eta}\right) - \Lambda \tag{3.79}$$

Using equation (3.66) and differential measurement of modal frequencies, that is $\lambda_{1,1} - \lambda_{1,2}$, the input angular rotation rate Ω is computed. A design parameter for MEMS gyroscopes is the mechanical scale factor. Defining the scale factor as the absolute difference between λ_1 and λ_2 for $\Omega = 1^\circ/\text{sec}$, the scale factor is computed from equation (3.66) solving for $\lambda_{1,1} - \lambda_{1,2}$.

Figures 3.6(a)-3.6(f) represent the frequency split versus the rotation rate for a similar set of dimensions as previous results, see Figures 3.4(a)-3.4(f). The lower the initial mismatch is, the higher the resolution is in that the slope of the curve is higher. Therefore, measuring the modal frequency difference in a gyroscope with high quality factor (low damping) is transformed into the angular rotation rate. This method presents an unlimited bandwidth with the instability limitation presented in the previous section. Consequently, in practice there is no limitation in terms of quality factor, while in conventional amplitude modulation based gyroscopes an ultra high quality factor results in a very limited bandwidth.

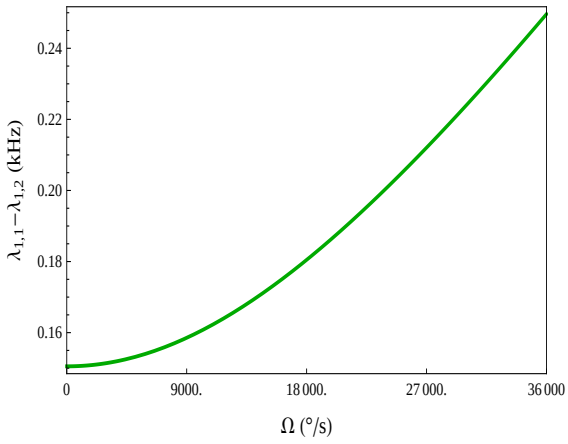

(a) $e = 0.05$ and $\frac{a_M}{a_B} = 10$

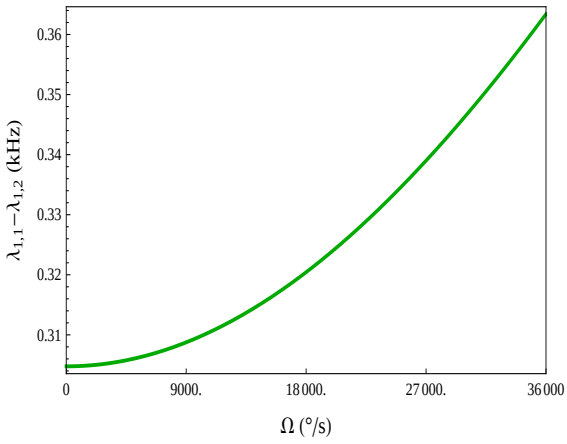

(b) $e = 0.05$ and $\frac{a_M}{a_B} = 15$

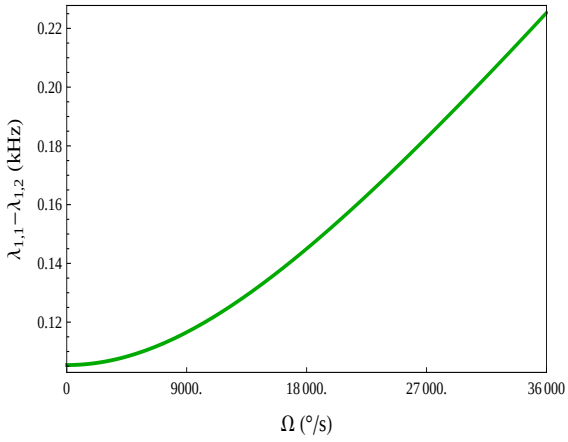

(c) $e = 0.1$ and $\frac{a_M}{a_B} = 10$

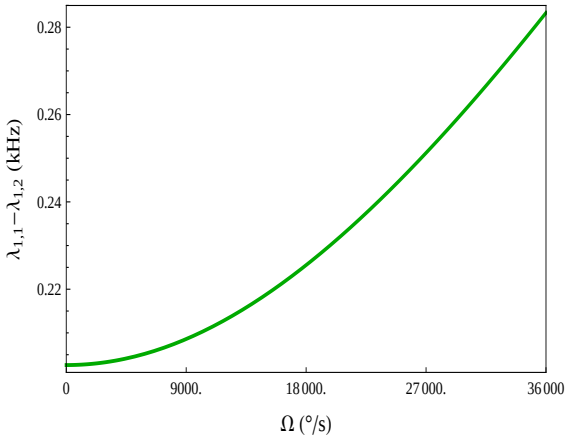

(d) $e = 0.1$ and $\frac{a_M}{a_B} = 15$

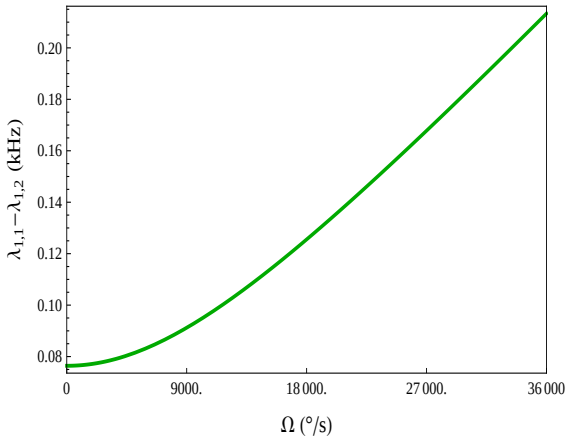

(e) $e = 0.15$ and $\frac{a_M}{a_B} = 10$

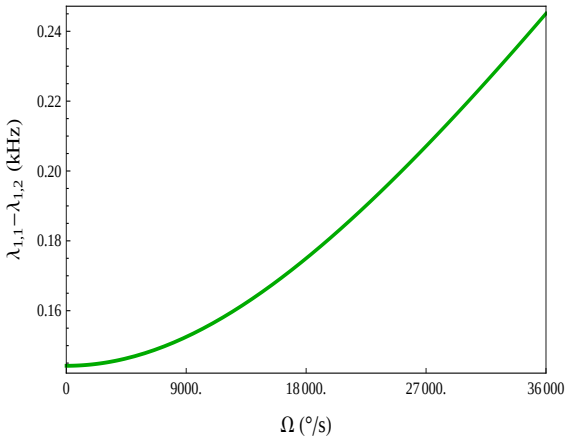

(f) $e = 0.15$ and $\frac{a_M}{a_B} = 15$

Figure 3.6: The modal frequency split (the difference between fundamental gyroscopic frequencies) in the rotating frame for the variation in the width ratio and the eccentricity.

3.3.5 Modal Frequencies under the DC Loading

Manufacturing errors or excitation requirements affect the design. To remove or increase or decrease the initial mismatch of natural frequencies in the drive and sense directions, the bias DC voltages are used, see Figure 3.2(a)-3.2(f). Inserting equation (3.53) into equations (3.48) and (3.49), dropping the damping terms but keeping DC voltages results in the characteristic equation in the form of equation (3.54) where the modified coefficients are given as

$$
\begin{aligned}
h_2 =& \Delta\Bigg(\Delta\Omega^2\Bigg(-\Big(-\alpha\Gamma' + \Gamma + M\left(e\psi'(1)+\psi(1)\right)^2 + \psi'(1)^2\left(J_{\zeta\zeta} - J_{\xi\xi}\right)\Big) \\
&\left(\alpha\Delta^2\Lambda' + M\left(e\phi'(1)+\phi(1)\right)^2 + J_{\zeta\zeta}\phi'(1)^2 + \Lambda\right) \\
&-\left(\alpha\Gamma' + \Gamma + M\left(e\psi'(1)+\psi(1)\right)^2 + J_{\eta\eta}\psi'(1)^2\right) \\
&\left(-\alpha\Delta^2\Lambda' + M\left(e\phi'(1)+\phi(1)\right)^2 + \phi'(1)^2\left(J_{\eta\eta} - J_{\xi\xi}\right) + \Lambda\right) \\
&+\Big(2M\left(e\psi'(1)+\psi(1)\right)\left(e\phi'(1)+\phi(1)\right) + \psi'(1)\phi'(1)\left(J_{\zeta\zeta} + J_{\eta\eta} - J_{\xi\xi}\right) + 2\Pi\Big)^2\Bigg) \\
&+\left(\alpha\Gamma' + \Gamma + M\left(e\psi'(1)+\psi(1)\right)^2 + J_{\eta\eta}\psi'(1)^2\right)\left(\Delta^3\Lambda'' + \frac{2e\nu V_w^2\left(e\phi'(1)+\phi(1)\right)^2}{\left(p_s\left(e\phi'(1)+\phi(1)\right)-1\right)^3}\right) \\
&+\left(\alpha\Delta^2\Lambda' + M\left(e\phi'(1)+\phi(1)\right)^2 + J_{\zeta\zeta}\phi'(1)^2 + \Lambda\right)\left(\Delta\Gamma'' + \frac{2e\nu V_v^2\left(e\psi'(1)+\psi(1)\right)^2}{\left(q_s\left(e\psi'(1)+\psi(1)\right)-1\right)^3}\right)\Bigg)
\end{aligned} \tag{3.80}
$$

$$
c_2 = Q_2\left(\Delta^3\Lambda'' + \frac{2e\nu V_w^2\left(e\phi'(1)+\phi(1)\right)^2}{\left(p_s\left(e\phi'(1)+\phi(1)\right)-1\right)^3}\right) + P_2\left(\Delta\Gamma'' + \frac{2e\nu V_v^2\left(e\psi'(1)+\psi(1)\right)^2}{\left(q_s\left(e\psi'(1)+\psi(1)\right)-1\right)^3}\right) \tag{3.81}
$$

$$
\begin{aligned}
c_0 =& \frac{\left(\Delta^3\Lambda''\left(p_s\left(e\phi'(1)+\phi(1)\right)-1\right)^3 + 2e\nu V_w^2\left(e\phi'(1)+\phi(1)\right)^2\right)}{\left(p_s\left(e\phi'(1)+\phi(1)\right)-1\right)^3} \\
&\frac{\left(\Delta\Gamma''\left(q_s\left(e\psi'(1)+\psi(1)\right)-1\right)^3 + 2e\nu V_v^2\left(e\psi'(1)+\psi(1)\right)^2\right)}{\left(q_s\left(e\psi'(1)+\psi(1)\right)-1\right)^3}
\end{aligned} \tag{3.82}
$$

Other coefficients, h_4 and c_4, remain similar to as given in equations (3.55) and (3.57). Furthermore, the input rotation rate Ω is computed by measuring the modal frequency split using equation (3.66). For the data set provided in Table 3.1, the modal frequencies and calibration curves are plotted in Figures 3.7(a)-3.8(f). Matching the modal frequencies reduces the nonlinearity of the Ω-modal frequencies relation. Consequently, the gyroscope output in terms of modal frequency split becomes almost linear, see Figure 3.8(f).

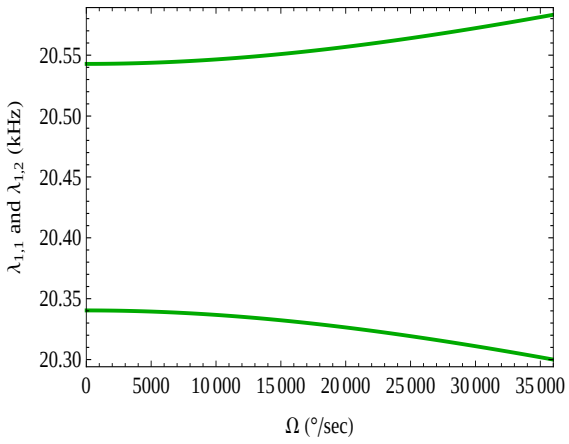

(a) Modal frequencies for $V_v = 3\text{V}$ and $V_w = 3\text{V}$

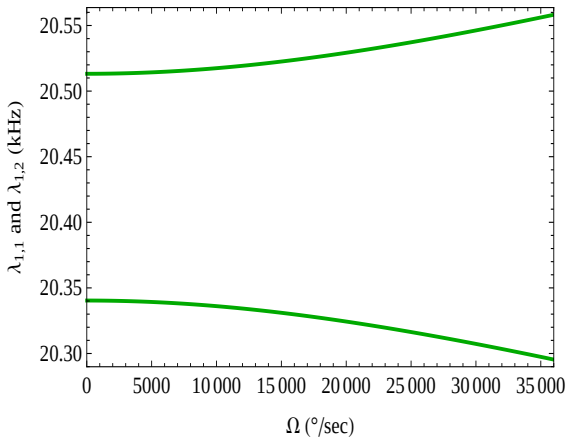

(b) Modal frequencies for $V_v = 3\text{V}$ and $V_w = 5\text{V}$

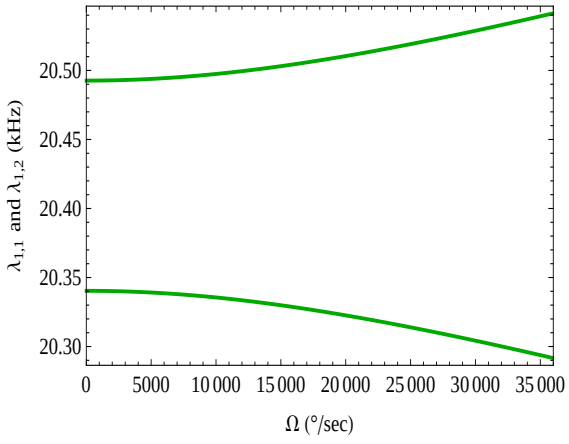

(c) Modal frequencies for $V_v = 3\text{V}$ and $V_w = 6\text{V}$

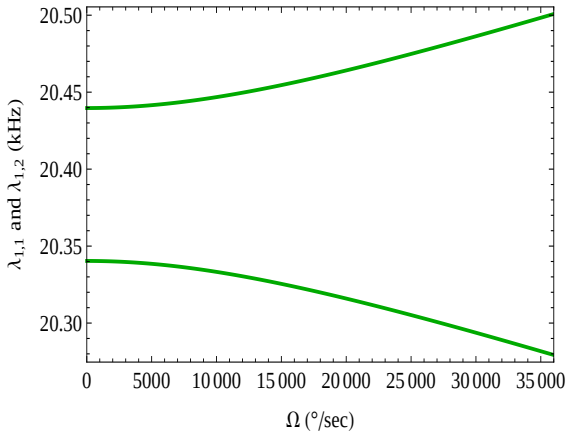

(d) Modal frequencies for $V_v = 3\text{V}$ and $V_w = 8\text{V}$

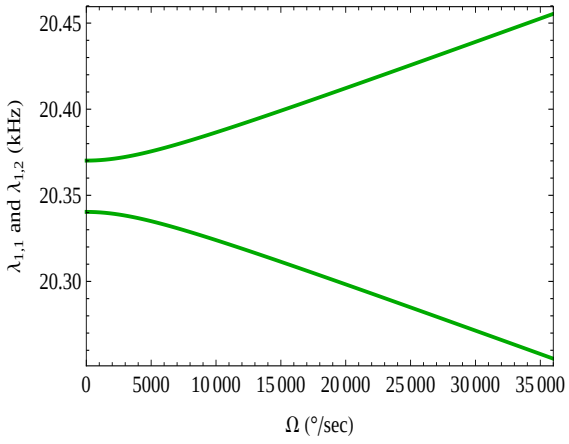

(e) Modal frequencies for $V_v = 3\text{V}$ and $V_w = 10\text{V}$

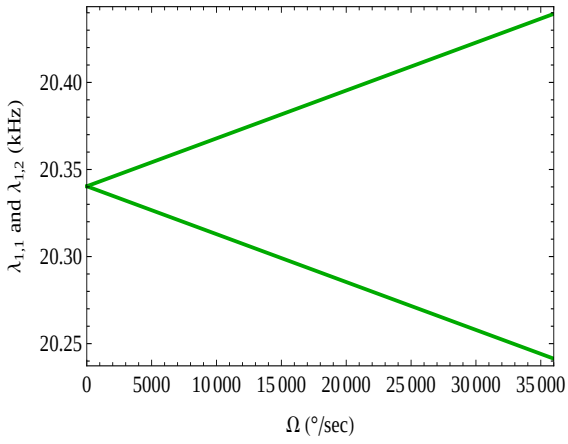

(f) Modal frequencies for $V_v = 3\text{V}$ and $V_w = 10.731\text{V}$

Figure 3.7: The variation in the fundamental modal frequencies in the rotating frame for the variation in the DC loadings ($e = 0.1$ and $\frac{a_M}{a_B} = 15$).

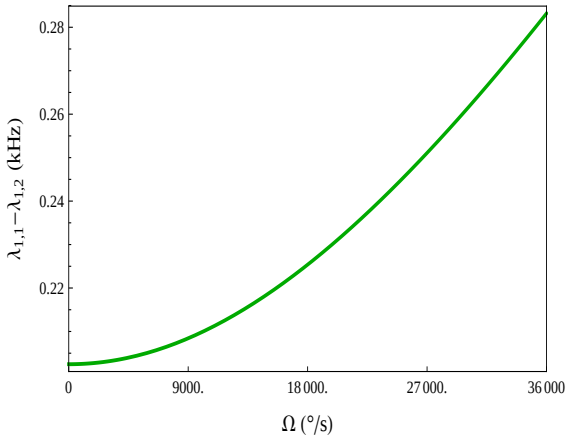

(a) Calibration curve for V_v = 3V and V_w = 3V

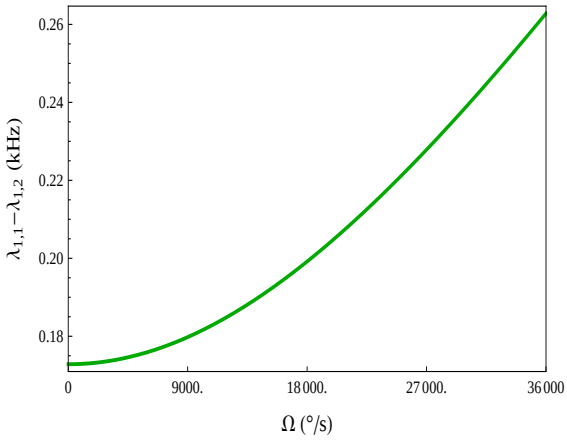

(b) Calibration curve for V_v = 3V and V_w = 5V

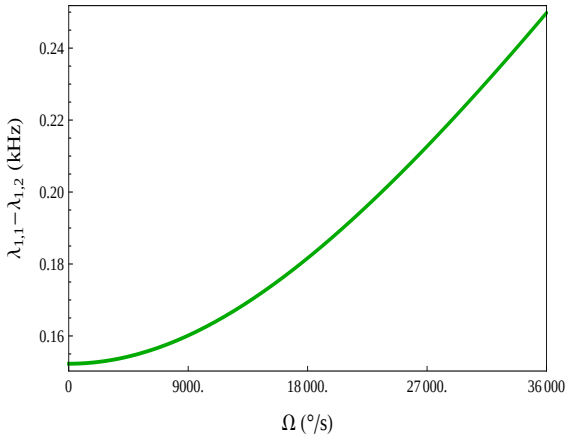

(c) Modal frequencies for V_v = 3V and V_w = 6V

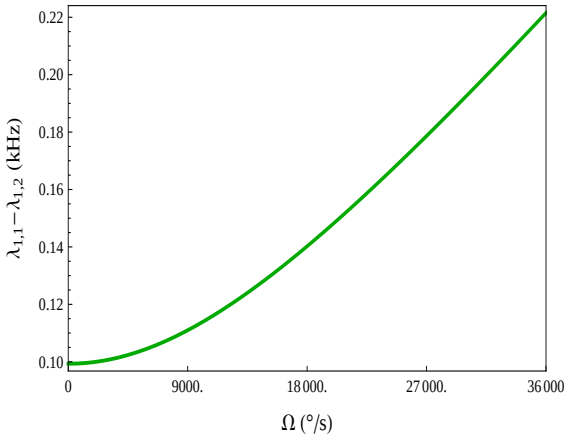

(d) Modal frequencies for V_v = 3V and V_w = 8V

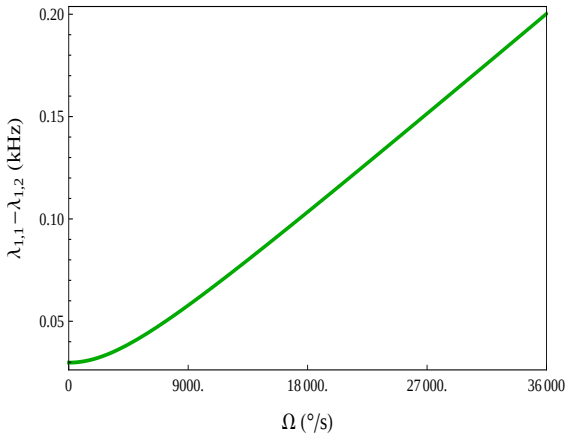

(e) Calibration curve for V_v = 3V and V_w = 10V

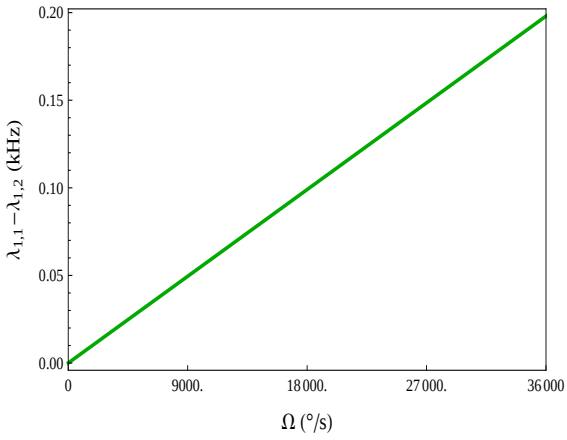

(f) Calibration curve for V_v = 3V and V_w = 10.731V

Figure 3.8: The variation in the fundamental modal frequency split in the rotating frame for the variation in the DC loadings (e = 0.1 and $\frac{a_M}{a_B}$ = 15).

3.4 Summary

In this chapter, the natural frequencies and mode shapes of the uncoupled system were computed. Using the mode shapes of uncoupled system, the free response of coupled cantilever beam-rigid body gyroscope was investigated. An example of micro-scale gyroscope was used to demonstrate the results. The modal frequencies in the rotating frame and pseudo-modal frequencies in the inertial frame were obtained. The instability region due to rotation rate was characterized. The rotation rate was computed in terms of modal frequencies. The differential measurement of the modal frequencies was translated to the angular rotation rate. The analytical results were clarified for the micro-scale beam-rigid body gyroscope and the scale factor was discussed.

Chapter 4

Reduced-Order Nonlinear Analysis

4.1 Preview

By virtue of the inherent nonlinearity of electrostatic force and the coupling of equations of motion in the drive and sense directions because of the angular rotation rate, the response of cantilever beam-rigid body gyroscope becomes multi-valued and loses its stability. In practice, the desired linear behavior is obtained for a certain range of parameters. To identify the proper set of parameters and operating points, the nonlinearity of the system is characterized using the "method of multiple scales", see Section 1.5.2.

In this chapter, the method of multiple scales is used to derive the slowly varying amplitude and phase of the system response under primary excitation. The slowly varying system is used to study the effect of frequency-mismatch on the dynamics of the gyroscope. Obtaining the "slow" system, or the system of modulation equations, and subsequently studying the dynamics of the slow system provides valuable information regarding the efficiency of the design and offer solutions to improve it accordingly.

4.2 Mathematical Method

To derive the proper form of the equations of motion for perturbation analysis, the equations of motion (2.75) and (2.76) are multiplied through by the denominator of the electrostatic force resulting in

$$\ddot{q}(t)\left(\gamma_{1,5}q_1(t)-1\right)^2+c_q\,\dot{q}(t)\left(\gamma_{1,5}q_1(t)-1\right)^2+\frac{\Omega\gamma_{1,2}\dot{p}(t)\left(\gamma_{1,5}q_1(t)-1\right)^2}{\gamma_{1,1}}$$
$$+\frac{\Omega^2q_1(t)\left(\gamma_{1,4}+\gamma_{1,3}\gamma_{1,5}q_1(t)\left(2-\gamma_{1,5}q_1(t)\right)\right)}{\gamma_{1,1}}$$

$$+\frac{\Gamma'' q_1(t)\left(\gamma_{1,5}q_1(t)-1\right)^2}{\gamma_{1,1}} = \frac{\nu\, e\, \gamma_{1,5}\left(V_{\mathrm{AC}}\cos\left(t\Omega_e\right)+V_w\right)^2}{\gamma_{1,1}} \tag{4.1}$$

and

$$\begin{aligned}\ddot{p}(t)\left(\gamma_{2,5}p_1(t)-1\right)^2 + c_p\,\dot{p}(t)\left(\gamma_{2,5}p_1(t)-1\right)^2 - \frac{\Omega\gamma_{2,2}\dot{q}(t)\left(\gamma_{2,5}p_1(t)-1\right)^2}{\gamma_{2,1}}\\ + \frac{\Omega^2 p_1(t)\left(\gamma_{2,4}+\gamma_{2,3}\gamma_{2,5}p_1(t)\left(2-\gamma_{2,5}p_1(t)\right)\right)}{\gamma_{2,1}}\\ + \frac{\Lambda'' p_1(t)\left(\gamma_{2,5}p_1(t)-1\right)^2}{\gamma_{2,1}} = \frac{\nu\, e\, \gamma_{2,5}V_v^2}{\gamma_{2,1}}\end{aligned} \tag{4.2}$$

where

$$\begin{aligned}\gamma_{1,1} &= \alpha\Gamma' + \Gamma + M\left(e\psi'(1)+\psi(1)\right)^2 + J_{22}\psi'(1)^2,\\ \gamma_{1,2} &= 2M\left(e\psi'(1)+\psi(1)\right)\left(e\phi'(1)+\phi(1)\right) + \left(-J_{11}+J_{22}+J_{33}\right)\psi'(1)\phi'(1) + 2\Pi,\\ \gamma_{1,3} &= -\alpha\Gamma' + \Gamma + M\left(e\psi'(1)+\psi(1)\right)^2 + \left(J_{33}-J_{11}\right)\psi'(1)^2,\\ \gamma_{1,4} &= \alpha\Gamma' - \Gamma - M\left(e\psi'(1)+\psi(1)\right)^2 + \left(J_{11}-J_{33}\right)\psi'(1)^2,\\ \gamma_{1,5} &= e\psi'(1)+\psi(1)\\ \gamma_{2,1} &= \alpha\Lambda' + M\left(e\phi'(1)+\phi(1)\right)^2 + J_{33}\phi'(1)^2 + \Lambda,\\ \gamma_{2,2} &= 2M\left(e\psi'(1)+\psi(1)\right)\left(e\phi'(1)+\phi(1)\right) + \left(-J_{11}+J_{22}+J_{33}\right)\psi'(1)\phi'(1) + 2\Pi,\\ \gamma_{2,3} &= -\alpha\Lambda' + M\left(e\phi'(1)+\phi(1)\right)^2 + \left(J_{22}-J_{11}\right)\phi'(1)^2 + \Lambda,\\ \gamma_{2,4} &= \alpha\Lambda' - M\left(e\phi'(1)+\phi(1)\right)^2 + \left(J_{11}-J_{22}\right)\phi'(1)^2 - \Lambda,\\ \gamma_{2,5} &= e\phi'(1)+\phi(1)\end{aligned} \tag{4.3}$$

Removing terms associated with the time derivative of the displacements, $\ddot{q}(t)$, $\dot{q}(t)$, $\ddot{p}(t)$ and $\dot{p}(t)$, results in the static equations equivalent to equations (3.45) and (3.46). The insertion of equation (3.44) into the preceding equations and using the equations of static equilibrium, results in the dynamic equations in the form

$$\begin{aligned}\omega_q^2 q_d(t) + \ddot{q}_d(t) =& 2Q_{14}V_{AC}V_w\cos\left(t\Omega_e\right) + \frac{1}{2}Q_{14}V_{AC}^2\cos\left(2t\Omega_e\right)\\ &- q_d(t)^2\left(Q_8\Omega\dot{p}_d(t) + Q_5\dot{q}_d(t) + Q_2\ddot{q}_d(t) + \Omega^2\left(3Q_{11}q_s + Q_{10}\right) + 3Q_{13}q_s + Q_{12}\right)\\ &+ q_d(t)\left(\Omega\left(-2Q_8q_s - Q_7\right)\dot{p}_d(t) - \left(2Q_5q_s + Q_4\right)\dot{q}_d(t)\right.\\ &\left.- \left(2Q_2q_s + Q_1\right)\ddot{q}_d(t) + \Omega^2\left(-3Q_{11}q_s^2 - 2Q_{10}q_s - Q_9\right)\right)\\ &+ \Omega\left(-Q_8q_s^2 - Q_7q_s - Q_6\right)\dot{p}_d(t) + \left(-Q_5q_s^2 - Q_4q_s - Q_3\right)\dot{q}_d(t)\end{aligned}$$

$$+\left(-Q_{11}\Omega^2 - Q_{13}\right) q_d(t)^3 \tag{4.4}$$

$$\begin{aligned}\omega_p^2 p_d(t) + \ddot{p}_d(t) =& p_d(t)^2 \left(\Omega^2 \left(-3P_{11}p_s - P_{10}\right) - P_5 \dot{p}_d(t) - P_2 \ddot{p}_d(t) - P_8 \Omega \dot{q}_d(t) - 3P_{13}p_s\right. \\ & \left. - P_{12}\right) + p_d(t) \left(\Omega \left(-2P_8 p_s - P_7\right) \dot{q}_d(t) + \left(-2P_5 p_s - P_4\right) \dot{p}_d(t)\right. \\ & \left. + \left(-2P_2 p_s - P_1\right) \ddot{p}_d(t) + \Omega^2 \left(-3P_{11}p_s^2 - 2P_{10}p_s - P_9\right)\right) \\ & + \Omega \left(-P_8 p_s^2 - P_7 p_s - P_6\right) \dot{q}_d(t) + \left(-P_5 p_s^2 - P_4 p_s - P_3\right) \dot{p}_d(t) \\ & + \left(-P_{11}\Omega^2 - P_{13}\right) p_d(t)^3 \end{aligned} \tag{4.5}$$

The coefficients ω_p, ω_q, Q_i and P_i for $i = 1, 2, ..., 14$ are given by

$$\begin{aligned}\omega_q^2 &= \frac{\Gamma'' \left(3\gamma_{1,5}q_s - 1\right)}{\gamma_{1,1} \left(\gamma_{1,5}q_s - 1\right)}, Q_1 = -\frac{2\gamma_{1,5}}{\left(\gamma_{1,5}q_s - 1\right)^2}, Q_2 = \frac{\gamma_{1,5}^2}{\left(\gamma_{1,5}q_s - 1\right)^2}, Q_3 = \frac{\Gamma\omega_D}{Q_q \left(\gamma_{1,5}q_s - 1\right)^2}, \\ Q_4 &= \frac{-2\Gamma\gamma_{1,5}\omega_D}{Q_q \left(\gamma_{1,5}q_s - 1\right)^2}, Q_5 = \frac{\Gamma\gamma_{1,5}^2\omega_D}{Q_q \left(\gamma_{1,5}q_s - 1\right)^2}, Q_6 = \frac{\gamma_{1,2}}{\gamma_{1,1} \left(\gamma_{1,5}q_s - 1\right)^2}, Q_7 = \frac{-2\gamma_{1,2}\gamma_{1,5}}{\gamma_{1,1} \left(\gamma_{1,5}q_s - 1\right)^2}, \\ Q_8 &= \frac{\gamma_{1,2}\gamma_{1,5}^2}{\gamma_{1,1} \left(\gamma_{1,5}q_s - 1\right)^2}, Q_9 = \frac{\gamma_{1,4}}{\gamma_{1,1} \left(\gamma_{1,5}q_s - 1\right)^2}, Q_{10} = \frac{2\gamma_{1,3}\gamma_{1,5}}{\gamma_{1,1} \left(\gamma_{1,5}q_s - 1\right)^2}, Q_{11} = \frac{-\gamma_{1,3}\gamma_{1,5}^2}{\gamma_{1,1} \left(\gamma_{1,5}q_s - 1\right)^2}, \\ Q_{12} &= -\frac{2\gamma_{1,5}\Gamma''}{\gamma_{1,1} \left(\gamma_{1,5}q_s - 1\right)^2}, Q_{13} = \frac{\gamma_{1,5}^2\Gamma''}{\gamma_{1,1} \left(\gamma_{1,5}q_s - 1\right)^2}, Q_{14} = \frac{e\nu\gamma_{1,5}}{\gamma_{1,1} \left(\gamma_{1,5}q_s - 1\right)^2} \end{aligned} \tag{4.6}$$

for the drive equation, and

$$\begin{aligned}\omega_p^2 &= \frac{\Lambda'' \left(3\gamma_{2,5}p_s - 1\right)}{\gamma_{2,1} \left(\gamma_{2,5}p_s - 1\right)}, P_1 = -\frac{2\gamma_{2,5}}{\left(\gamma_{2,5}p_s - 1\right)^2}, P_2 = \frac{\gamma_{2,5}^2}{\left(\gamma_{2,5}p_s - 1\right)^2}, P_3 = \frac{\Lambda\omega_S}{Q_p \left(\gamma_{2,5}p_s - 1\right)^2} \\ P_4 &= \frac{-2\Lambda\gamma_{2,5}\omega_S}{Q_p \left(\gamma_{2,5}p_s - 1\right)^2}, P_5 = \frac{\Lambda\gamma_{2,5}^2\omega_S}{Q_p \left(\gamma_{2,5}p_s - 1\right)^2}, P_6 = \frac{-\gamma_{2,2}}{\gamma_{2,1} \left(\gamma_{2,5}p_s - 1\right)^2}, P_7 = \frac{2\gamma_{2,2}\gamma_{2,5}}{\gamma_{2,1} \left(\gamma_{2,5}p_s - 1\right)^2}, \\ P_8 &= \frac{-\gamma_{2,2}\gamma_{2,5}^2}{\gamma_{2,1} \left(\gamma_{2,5}p_s - 1\right)^2}, P_9 = \frac{\gamma_{2,4}}{\gamma_{2,1} \left(\gamma_{2,5}p_s - 1\right)^2}, P_{10} = \frac{2\gamma_{2,3}\gamma_{2,5}}{\gamma_{2,1} \left(\gamma_{2,5}p_s - 1\right)^2}, P_{11} = \frac{-\gamma_{2,3}\gamma_{2,5}^2}{\gamma_{2,1} \left(\gamma_{2,5}p_s - 1\right)^2}, \\ P_{12} &= \frac{-2\gamma_{2,5}\Lambda''}{\gamma_{2,1} \left(\gamma_{2,5}p_s - 1\right)^2}, P_{13} = \frac{\gamma_{2,5}^2\Lambda''}{\gamma_{2,1} \left(\gamma_{2,5}p_s - 1\right)^2}, P_{14} = \frac{e\nu\gamma_{2,5}}{\gamma_{2,1} \left(\gamma_{2,5}p_s - 1\right)^2} \end{aligned} \tag{4.7}$$

for the sense equation. To derive the system of slowly varying parameters of the system, the method of multiple scales is employed. To determine a uniform second-order approximation of the response, the flexural displacements of the structure in the sense and drive directions are expressed

in the form

$$q_d(t) = \epsilon\, q_{d1}(t_0,t_1,t_2) + \epsilon^2 q_{d2}(t_0,t_1,t_2) + \epsilon^3 q_{d3}(t_0,t_1,t_2) \tag{4.8}$$

$$p_d(t) = \epsilon\, p_{d1}(t_0,t_1,t_2) + \epsilon^2 p_{d2}(t_0,t_1,t_2) + \epsilon^3 p_{d3}(t_0,t_1,t_2) \tag{4.9}$$

where the time scales are defined as $t_0 = t$, $t_1 = \epsilon\, t$, and $t_2 = \epsilon^2 t$. The parameter ϵ indicates the order of the terms. The forcing term, V_{AC}, is scaled by introducing ϵ^3, the rotation rate Ω by ϵ^2, and the damping terms by ϵ such that they appear in the third-order equations. Inserting (4.8) and (4.9) into (4.4) and (4.5) and collecting the coefficients of like powers of ϵ results in the following sequence of equations:

- $O(\epsilon^1)$:

$$\partial_0^2 q_{d1} + \omega_q^2 q_{d1} = 0 \tag{4.10}$$

$$\partial_0^2 p_{d1} + \omega_p^2 p_{d1} = 0 \tag{4.11}$$

- $O(\epsilon^2)$:

$$\begin{aligned}\partial_0^2 q_{d2} + \omega_q^2 q_{d2} = &-3Q_{13} q_s q_{d1}^2 - 2Q_2 q_s\, q_{d1}\, \partial_0^2 q_{d1} - Q_{12} q_{d1}^2 \\ &- Q_1\, q_{d1}\, \partial_0^2 q_{d1} - 2\partial_1\partial_0 q_{d1},\end{aligned} \tag{4.12}$$

$$\begin{aligned}\partial_0^2 p_{d2} + \omega_p^2 p_{d2} = &-3P_{13} p_s p_{d1}^2 - 2P_2 p_s\, p_{d1} - P_{12} p_{d1}^2 \partial_0^2 p_{d1} \\ &- P_1\, p_{d1}\, \partial_0^2 p_{d1} - 2\partial_1\partial_0 p_{d1}\end{aligned} \tag{4.13}$$

- $O(\epsilon^3)$:

$$\begin{aligned}\partial_0^2 q_{d3} + q_{d3}\,\omega_q^2 = &\,2\,Q_{14}\,V_{\mathrm{AC}}\,V_w \cos(\Omega_e\, t) - \Omega Q_8 \partial_0 p_{d1}\, q_s^2 - Q_5 \partial_0 q_{d1}\, q_s^2 - \Omega Q_7 \partial_0 p_{d1}\, q_s \\ &- Q_4 \partial_0 q_{d1}\, q_s - 4Q_2 q_{d1}\, \partial_1\partial_0 q_{d1}\, q_s - 2Q_2 q_{d2}\, \partial_0^2 q_{d1}\, q_s \\ &- 2Q_2 q_{d1}\, \partial_0^2 q_{d2}\, q_s - 2Q_{12} q_{d1}\, q_{d2} \\ &- Q_{13}\left(q_{d1}^3 + 6 q_s q_{d2}\, q_{d1}\right) - \partial_1^2 q_{d1} - \Omega Q_6 \partial_0 p_{d1} \\ &- Q_3 \partial_0 q_{d1} - 2\partial_2\partial_0 q_{d1} - 2Q_1 q_{d1}\, \partial_1\partial_0 q_{d1} - 2\partial_1\partial_0 q_{d2} \\ &- Q_2 q_{d1}^2 \partial_0^2 q_{d1} - Q_1 q_{d2}\, \partial_0^2 q_{d1} - Q_1 q_{d1}\, \partial_0^2 q_{d2},\end{aligned} \tag{4.14}$$

$$\begin{aligned}\partial_0^2 p_{d3} + p_{d3}\,\omega_p^2 = &-P_{13} p_{d1}^3 - P_2 \partial_0^2 p_{d1}\, p_{d1}^2 - 2P_{12} p_{d2}\, p_{d1} - 6 p_s P_{13} p_{d2}\, p_{d1} \\ &- 2P_1 \partial_1\partial_0 p_{d1}\, p_{d1} - 4 p_s P_2 \partial_1\partial_0 p_{d1}\, p_{d1} - P_1 \partial_0^2 p_{d2}\, p_{d1} \\ &- 2 p_s P_2 \partial_0^2 p_{d2}\, p_{d1} - \partial_1^2 p_{d1} - P_3 \partial_0 p_{d1} - p_s P_4 \partial_0 p_{d1} - p_s^2 P_5 \partial_0 p_{d1} \\ &- \Omega P_6 \partial_0 q_{d1} - \Omega p_s P_7 \partial_0 q_{d1} - \Omega p_s^2 P_8 \partial_0 q_{d1} \\ &- 2\partial_2\partial_0 p_{d1} - 2\partial_1\partial_0 p_{d2} - P_1 p_{d2}\, \partial_0^2 p_{d1} - 2 p_s P_2 p_{d2}\, \partial_0^2 p_{d1}\end{aligned} \tag{4.15}$$

where ∂_m^n indicates the nth derivative with respect to the mth time scale, that is t_m, for $m = 0, 1, 2$.

Equations (4.10) and (4.11) represent two uncoupled eigenvalue problems and therefore their solutions are expressed in the form

$$q_{d1}(t_0,t_1,t_2) = \bar{A}_q(t_1,t_2)\, e^{-it_0\omega_q} + A_q(t_1,t_2)\, e^{it_0\omega_q} \tag{4.16}$$

$$p_{d1}(t_0,t_1,t_2) = \bar{A}_p(t_1,t_2)\, e^{-it_0\omega_p} + A_p(t_1,t_2)\, e^{it_0\omega_p} \tag{4.17}$$

where $A_q(t_1,t_2)$ and $A_p(t_1,t_2)$ and their complex conjugates $\bar{A}_q(t_1,t_2)$ and $\bar{A}_p(t_1,t_2)$ are to be determined by removing secular terms in computing the solutions of the second $O(\epsilon^2)$ and third order $O(\epsilon^3)$ problems. The arguments of functions, that is (t_0,t_1,t_2) and (t_1,t_2), are removed where ever it is necessary for the clarity and brevity of notation.

Introducing equations (4.16) and (4.17) in the second order equations (4.12) and (4.13) and collecting terms gives

$$\begin{aligned}
\partial_0^2 q_{d2} + \omega_q^2 q_{d2} &= \left(q_s\left(4Q_2\omega_q^2 - 6Q_{13}\right) + 2Q_1\omega_q^2 - 2Q_{12}\right)\bar{A}_q(t_1,t_2)\,A_q(t_1,t_2) \\
&+ \left(q_s\left(2Q_2\omega_q^2 - 3Q_{13}\right) + Q_1\omega_q^2 - Q_{12}\right)\bar{A}_q(t_1,t_2)^2 e^{-2it_0\omega_q} \\
&+ \left(q_s\left(2Q_2\omega_q^2 - 3Q_{13}\right) + Q_1\omega_q^2 - Q_{12}\right)A_q(t_1,t_2)^2 e^{2it_0\omega_q} \\
&+ 2i\omega_q e^{-it_0\omega_q}\partial_1\bar{A}_q(t_1,t_2) - 2i\omega_q e^{it_0\omega_q}\partial_1 A_q(t_1,t_2)
\end{aligned} \tag{4.18}$$

$$\begin{aligned}
\partial_0^2 p_{d2} + \omega_p^2 p_{d2} &= \left(p_s\left(4P_2\omega_p^2 - 6P_{13}\right) + 2P_1\omega_p^2 - 2P_{12}\right)\bar{A}_p(t_1,t_2)\,A_p(t_1,t_2) \\
&+ \left(p_s\left(2P_2\omega_p^2 - 3P_{13}\right) + P_1\omega_p^2 - P_{12}\right)\bar{A}_p(t_1,t_2)^2 e^{-2it_0\omega_p} \\
&+ \left(p_s\left(2P_2\omega_p^2 - 3P_{13}\right) + P_1\omega_p^2 - P_{12}\right)A_p(t_1,t_2)^2 e^{2it_0\omega_p} \\
&- 2i\omega_p e^{it_0\omega_p}\partial_1 A_p(t_1,t_2) + 2i\omega_p e^{-it_0\omega_p}\partial_1\bar{A}_p(t_1,t_2)
\end{aligned} \tag{4.19}$$

To remove the secular terms in the preceding equations, the coefficients of $e^{it_0\omega_q}$ $e^{-it_0\omega_q}$, $e^{it_0\omega_p}$, and $e^{-it_0\omega_p}$ are set to zero. Therefore, $A_q(t_1,t_2)$ and $A_p(t_1,t_2)$ and their complex conjugates are only functions of t_2. Thus,

$$q_{d1}(t_0,t_2) = \bar{A}_q(t_2)\, e^{-it_0\omega_q} + A_q(t_2)\, e^{it_0\omega_q} \tag{4.20}$$

$$p_{d1}(t_0,t_2) = \bar{A}_p(t_2)\, e^{-it_0\omega_p} + A_p(t_2)\, e^{it_0\omega_p} \tag{4.21}$$

Considering equations (4.20)-(4.21), the solutions of (4.18)-(4.19) are expressed in the form

$$q_{d2}(t_0,t_2) = G_1 e^{-2it_0\omega_q}\bar{A}_q^2 + 2G_2 A_q\,\bar{A}_q + G_1 A_q^2 e^{2it_0\omega_q} \tag{4.22}$$

$$p_{d2}(t_0,t_2) = H_1 e^{-2it_0\omega_p}\bar{A}_p^2 + 2H_2 A_p\,\bar{A}_p + H_1 A_p^2 e^{2it_0\omega_p} \tag{4.23}$$

where the unknown coefficients G_1, G_2, H_1, and H_2 are found by substituting equations (4.20)-(4.23) into equations (4.18) and (4.19) and equating the coefficients of equivalent terms on both sides of the equations. Therefore, the unknown coefficients G_1, G_2, H_1, and H_2 compute to

$$G_1 = \frac{-2Q_2 q_s \omega_q^2 + 3Q_{13} q_s - Q_1 \omega_q^2 + Q_{12}}{3\omega_q^2} \tag{4.24}$$

$$G_2 = \frac{2Q_2 q_s \omega_q^2 - 3Q_{13} q_s + Q_1 \omega_q^2 - Q_{12}}{\omega_q^2} \tag{4.25}$$

$$H_1 = \frac{-2P_2 p_s \omega_p^2 + 3P_{13} p_s - P_1 \omega_p^2 + P_{12}}{3\omega_p^2} \tag{4.26}$$

$$H_2 = \frac{2P_2 p_s \omega_p^2 - 3P_{13} p_s + P_1 \omega_p^2 - P_{12}}{\omega_p^2} \tag{4.27}$$

The interest of this thesis is to investigate the system response near primary resonance. On the other hand, for further analysis of the performance of the beam-rigid body gyroscope operating in the amplitude or frequency-modulation mode, the effect of mismatch of modal frequencies is investigated. Therefore, to describe the primary and internal resonances, two detuning parameters are introduced:

$$\Omega_e = \omega_q + \epsilon^2 \sigma \tag{4.28}$$

$$\omega_p = \omega_q + \epsilon^2 \delta \tag{4.29}$$

The first equation, (4.28), characterizes the nearness of the excitation frequency Ω_e to the drive natural frequency ω_q, and equation (4.29) characterizes the nearness of two modal frequencies in the drive and sense directions, that is ω_q and ω_p.

Substitution of equations (4.20)-(4.23) and (4.28) and (4.29) into the third order coupled problems, equations (4.14) and (4.15), and dropping terms associated with higher frequencies, that is $n\,\omega_q$ for $n > 1$, results in

$$\begin{aligned}
\partial_0^2 q_{d3} + \omega_q^2 q_{d3} = \Big(\big(& (5G_1 Q_1 + 2G_2 Q_1 + 10G_1 q_s Q_2 + 4G_2 q_s Q_2 + 3Q_2)\,\omega_q^2 \\
& -2G_1 Q_{12} - 4G_2 Q_{12} - (6G_1 q_s + 12G_2 q_s + 3)\,Q_{13} \big) \bar{A}_q A_q^2 \\
& - i \left(Q_5 q_s^2 + Q_4 q_s + Q_3 \right) \omega_q A_q + e^{i\sigma t_2} Q_{14} V_{\mathrm{AC}} V_w \\
& - i \left(Q_8 q_s^2 + Q_7 q_s + Q_6 \right) \omega_q \Omega A_p e^{i\delta t_2} - 2i\omega_q \dot{A}_q \Big) e^{it_0 \omega_q} + C.C.
\end{aligned} \tag{4.30}$$

$$\begin{aligned}
\partial_0^2 p_{d3} + \omega_q^2 p_{d3} = \Big(& -i \left(P_8 p_s^2 + P_7 p_s + P_6 \right) \Omega \omega_q A_q + e^{i\delta t_2} \big((5H_1 P_1 + 2H_2 P_1 \\
& + (10H_1 p_s + 4H_2 p_s + 3)\,P_2 \big) \omega_q^2 \bar{A}_p A_p^2 - (2H_1 P_{12} \\
& + 4H_2 P_{12} + (6H_1 p_s + 12H_2 p_s + 3)\,P_{13} \big) \bar{A}_p A_p^2
\end{aligned}$$

$$-i\omega_q\left(\left(P_5p_s^2+P_4p_s+P_3\right)A_p\ +2\dot{A}_p\ \right)\Bigg)\Bigg)e^{it_0\omega_q}+C.C. \tag{4.31}$$

where $\dot{A}_q$ and $\dot{A}_p$ represent the time derivative of amplitudes $A_q(t_2)$ and $A_p(t_2)$ with respect to the slow time scale t_2 and *C.C.* stands for the complex conjugate of its preceding term. The coefficients of $e^{it_0\omega_q}$ give rise to the secular terms. Therefore, the imaginary and real parts of the coefficients of $e^{it_0\omega_q}$ in equations (4.30) and (4.31) are set to zero. To this end, the amplitudes, $A_q(t_2)$ and $A_p(t_2)$, are expressed in polar form as

$$A_q\left(t_2\right)\ =\ \frac{1}{2}a_q(t_2)e^{i\theta_q(t_2)},\quad A_p\left(t_2\right)\ =\ \frac{1}{2}a_p(t_2)e^{i\theta_p(t_2)}, \tag{4.32}$$

substituted in equations (4.30) and (4.31), the real and imaginary parts are separately equated to zero resulting in the following four modulation equations

$$\begin{aligned}&\left(\frac{1}{4}\left(G_1+2G_2\right)\left(3Q_{13}q_s+Q_{12}\right)+\frac{3}{8}Q_{13}-\frac{1}{8}\omega_q^2\left(\left(5G_1+2G_2\right)\left(2Q_2q_s+Q_1\right)+3Q_2\right)\right)a_q^3\\&-\frac{1}{2}\Omega\omega_qa_p\left(q_s\left(Q_8q_s+Q_7\right)+Q_6\right)\sin\left(\eta_2\right)+\omega_qa_q\left(\dot{\eta}_1-\sigma\right)=Q_{14}V_{\mathrm{AC}}V_{\mathrm{w}}\cos\left(\eta_1\right)\end{aligned} \tag{4.33}$$

$$\begin{aligned}&\left(\frac{1}{4}\left(H_1+2H_2\right)+\frac{3}{8}P_{13}\cos\left(\eta_2\right)-\frac{1}{8}\omega_q^2\cos\left(\eta_2\right)\left(\left(5H_1+2H_2\right)\left(2P_2p_s+P_1\right)+3P_2\right)\right)a_p^3\\&+\omega_q\left(\left(\delta-\sigma+\dot{\eta}_1-\dot{\eta}_2\right)\cos\left(\eta_2\right)a_p-\sin\left(\eta_2\right)\dot{a}_p-\frac{1}{2}a_p\left(p_s\left(P_5p_s+P_4\right)+P_3\right)\sin\left(\eta_2\right)\right)\\&+\left(3P_{13}p_s+P_{12}\right)\cos\left(\eta_2\right)=0\end{aligned} \tag{4.34}$$

$$\begin{aligned}&\frac{1}{2}\Omega\omega_qa_p\left(q_s\left(Q_8q_s+Q_7\right)+Q_6\right)\cos\left(\eta_2\right)+\omega_q\left(\frac{1}{2}a_q\left(q_s\left(Q_5q_s+Q_4\right)+Q_3\right)+\dot{a}_q\right)\\&=Q_{14}V_{\mathrm{AC}}V_{\mathrm{w}}\sin\left(\eta_1\right)\end{aligned} \tag{4.35}$$

$$\begin{aligned}&\left(\frac{1}{4}\left(H_1+2H_2\right)+\frac{3}{8}P_{13}\sin\left(\eta_2\right)-\frac{1}{8}\omega_q^2\sin\left(\eta_2\right)\left(\left(5H_1+2H_2\right)\left(2P_2p_s+P_1\right)+3P_2\right)\right)a_p^3\\&+\left(\frac{1}{2}\left(p_s\left(P_5p_s+P_4\right)+P_3\right)\cos\left(\eta_2\right)a_p+\left(\delta-\sigma+\dot{\eta}_1-\dot{\eta}_2\right)\sin\left(\eta_2\right)a_p+\cos\left(\eta_2\right)\dot{a}_p\right)\omega_q\\&+\left(3P_{13}p_s+P_{12}\right)\sin\left(\eta_2\right)+\frac{1}{2}\,\Omega\,\omega_qa_q\left(p_s\left(P_8p_s+P_7\right)+P_6\right)=0\end{aligned} \tag{4.36}$$

where

$$\eta_2\left(t_2\right)=\theta_p\left(t_2\right)-\theta_q\left(t_2\right)+\delta\,t_2 \tag{4.37}$$

$$\eta_1(t_2) = \sigma\, t_2 - \theta_q(t_2) \tag{4.38}$$

and the time derives of the amplitudes and phases $\dot{a}_q$, $\dot{a}_p$, $\dot{\eta}_1$, and $\dot{\eta}_2$ are computed with respect to the slow time scale t_2. The general solutions, that is equations (4.8) and (4.9), of the system of equations are therefore

$$\begin{aligned} q_d(t) &= a_q(t)\cos\left(\Omega_e t - \eta_1(t)\right) - \left(\frac{1}{3}Q_2 q_s - \frac{1}{6}Q_1\right) a_q(t)^2 \cos\left(2\Omega_e t - 2\eta_1(t)\right) \\ &\quad + \left(Q_2 q_s + \frac{1}{2}Q_1 + \frac{\left(\frac{1}{2}Q_{13}q_s + \frac{1}{6}Q_{12}\right)\cos\left(2\,\Omega_e t - 2\eta_1(t)\right) - \frac{3}{2}Q_{13}q_s - \frac{1}{2}Q_{12}}{\omega_q^2}\right) a_q(t)^2 \end{aligned} \tag{4.39}$$

$$\begin{aligned} p_d(t) &= a_p(t)\cos\left(\Omega_e t - \eta_1(t) + \eta_2(t)\right) + \frac{\left(2P_2 p_s \omega_p^2 - 3P_{13}p_s + P_1\omega_p^2 - P_{12}\right)}{2\omega_p^2} a_p(t)^2 \\ &\quad + \frac{\left(-2P_2 p_s \omega_p^2 + 3P_{13}p_s - P_1\omega_p^2 + P_{12}\right)\cos\left(2\Omega_e t - 2\eta_1(t) + 2\eta_2(t)\right)}{6\omega_p^2} a_p(t)^2 \end{aligned} \tag{4.40}$$

4.3 Steady-State Response and its Stability

The former set of the second-order approximation of the dynamic response, equations (4.39) and (4.40), represent a periodic solution with constant amplitudes for constant $a_q(t)$, $a_p(t)$, $\eta_1(t)$, and $\eta_2(t)$. Therefore, the fixed points of the system of equations (4.33)-(4.36) corresponds to the periodic solutions of the structure about the static equilibrium. The system of equilibrium equations expressed in the form of

$$\begin{aligned} &\left(\frac{1}{4}\left(G_1 + 2G_2\right)\left(3Q_{13}q_s + Q_{12}\right) + \frac{3}{8}Q_{13} - \frac{1}{8}\omega_q^2\left(\left(5G_1 + 2G_2\right)\left(2Q_2 q_s + Q_1\right) + 3Q_2\right)\right) a_q^3 \\ &- \frac{1}{2}\Omega\omega_q a_p\left(q_s\left(Q_8 q_s + Q_7\right) + Q_6\right)\sin\left(\eta_2\right) - \omega_q a_q\,\sigma = Q_{14}V_{\mathrm{AC}}V_{\mathrm{w}}\cos\left(\eta_1\right) \end{aligned} \tag{4.41}$$

$$\begin{aligned} &\left(\frac{1}{4}\left(H_1 + 2H_2\right) + \frac{3}{8}P_{13}\cos\left(\eta_2\right) - \frac{1}{8}\omega_q^2\cos\left(\eta_2\right)\left(\left(5H_1 + 2H_2\right)\left(2P_2 p_s + P_1\right) + 3P_2\right)\right) a_p^3 \\ &+ \omega_q\left(\left(\delta - \sigma\right)\cos\left(\eta_2\right) - \frac{1}{2}\left(p_s\left(P_5 p_s + P_4\right) + P_3\right)\sin\left(\eta_2\right)\right) a_p + \left(3P_{13}p_s + P_{12}\right)\cos\left(\eta_2\right) = 0 \end{aligned} \tag{4.42}$$

$$\frac{1}{2}\left(q_s\left(Q_8 q_s + Q_7\right) + Q_6\right)\cos\left(\eta_2\right)\Omega\omega_q a_p + \frac{1}{2}\left(q_s\left(Q_5 q_s + Q_4\right) + Q_3\right) a_q\,\omega_q = Q_{14}V_{\mathrm{AC}}V_{\mathrm{w}}\sin\left(\eta_1\right) \tag{4.43}$$

$$\left(\frac{1}{4}\left(H_1+2H_2\right)+\frac{3}{8}P_{13}\sin\left(\eta_2\right)-\frac{1}{8}\omega_q^2\sin\left(\eta_2\right)\left(\left(5H_1+2H_2\right)\left(2P_2p_s+P_1\right)+3P_2\right)\right)a_p^3$$
$$+\left(\frac{1}{2}\left(p_s\left(P_5p_s+P_4\right)+P_3\right)\cos\left(\eta_2\right)+\left(\delta-\sigma\right)\sin\left(\eta_2\right)\right)a_p\omega_q+\left(3P_{13}p_s+P_{12}\right)\sin\left(\eta_2\right)$$
$$+\frac{1}{2}\left(p_s\left(P_8p_s+P_7\right)+P_6\right)\Omega\,\omega_q\,a_q=0 \tag{4.44}$$

are solved for a_q, a_p, η_1, and η_2, to compute the equilibrium points of the response. The modulation and equilibrium equations are expressed in the Cartesian form by describing the amplitudes in the form

$$A_q\left(t_2\right)\;=\;\frac{1}{2}\left(x_q(t_2)-iy_q(t_2)\right)e^{i\lambda_q(t_2)},\quad A_p\left(t_2\right)\;=\;\frac{1}{2}\left(x_p\left(t_2\right)-iy_p\left(t_2\right)\right)e^{i\lambda_p(t_2)} \tag{4.45}$$

Following the same procedure as outlined for the polar form results in the modulation equation. Therefore, the modulation equations (slow system) in the Cartesian form become

$$\dot{x}_q=f_1 \tag{4.46}$$
$$\dot{y}_q=f_2 \tag{4.47}$$
$$\dot{x}_p=f_3 \tag{4.48}$$
$$\dot{y}_p=f_4 \tag{4.49}$$

where

$$f_1=\frac{x_q^2y_q\left(2\left(G_1+2G_2\right)\left(3Q_{13}q_s+Q_{12}\right)+3Q_{13}\right)-\omega_q^2\left(\left(\left(5G_1+2G_2\right)\left(2Q_2q_s+Q_1\right)+3Q_2\right)\right)}{8\omega_q}$$
$$+\frac{y_q^3\left(\omega_q^2\left(-\left(\left(5G_1+2G_2\right)\left(2Q_2q_s+Q_1\right)+3Q_2\right)\right)+2\left(G_1+2G_2\right)\left(3Q_{13}q_s+Q_{12}\right)+3Q_{13}\right)}{8\omega_q}$$
$$+\frac{1}{2}x_q\left(-q_s\left(Q_5q_s+Q_4\right)-Q_3\right)-\frac{1}{2}\mathrm{xp}_1\Omega\left(q_s\left(Q_8q_s+Q_7\right)+Q_6\right)-\sigma y_q$$
$$f_2=\frac{Q_{14}V_{\mathrm{AC}}V_{\mathrm{w}}}{\omega_q}+\sigma x_q-\frac{1}{2}\Omega y_p\left(q_s\left(Q_8q_s+Q_7\right)+Q_6\right)+\frac{1}{2}y_q\left(-q_s\left(Q_5q_s+Q_4\right)-Q_3\right)$$
$$+x_q\left(\frac{y_q^2\left(\omega_q^2\left(\left(5G_1+2G_2\right)\left(2Q_2q_s+Q_1\right)+3Q_2\right)-2\left(G_1+2G_2\right)\left(3Q_{13}q_s+Q_{12}\right)-3Q_{13}\right)}{8\omega_q}\right)$$
$$+\frac{x_q^3\left(\omega_q^2\left(\left(5G_1+2G_2\right)\left(2Q_2q_s+Q_1\right)+3Q_2\right)-2\left(G_1+2G_2\right)\left(3Q_{13}q_s+Q_{12}\right)-3Q_{13}\right)}{8\omega_q}$$
$$f_3=\frac{1}{2}x_p\left(-p_s\left(P_5p_s+P_4\right)-P_3\right)+\left(\delta-\sigma\right)y_p-\frac{1}{2}\Omega x_q\left(p_s\left(P_8p_s+P_7\right)+P_6\right)$$

$$
\begin{aligned}
&+\frac{x_p^2 y_p\left(\omega_q^2\left(-\left((5H_1+2H_2)\left(2P_2p_s+P_1\right)+3P_2\right)\right)+2\left(H_1+2H_2\right)\left(3P_{13}p_s+P_{12}\right)+3P_{13}\right)}{8\omega_q}\\
&+\frac{y_p^3\left(\omega_q^2\left(-\left((5H_1+2H_2)\left(2P_2p_s+P_1\right)+3P_2\right)\right)+2\left(H_1+2H_2\right)\left(3P_{13}p_s+P_{12}\right)+3P_{13}\right)}{8\omega_q}\\
f_4=&\frac{1}{2}y_p\left(-p_s\left(P_5p_s+P_4\right)-P_3\right)-\frac{1}{2}\Omega y_q\left(p_s\left(P_8p_s+P_7\right)+P_6\right)+\left(\sigma-\delta\right)x_p\\
&+x_p\left(\frac{y_p^2\left(\omega_q^2\left((5H_1+2H_2)\left(2P_2p_s+P_1\right)+3P_2\right)-2\left(H_1+2H_2\right)\left(3P_{13}p_s+P_{12}\right)-3P_{13}\right)}{8\omega_q}\right)\\
&+\frac{x_p^3\left(\omega_q^2\left((5H_1+2H_2)\left(2P_2p_s+P_1\right)+3P_2\right)-2\left(H_1+2H_2\right)\left(3P_{13}p_s+P_{12}\right)-3P_{13}\right)}{8\omega_q}
\end{aligned}
\tag{4.50}
$$

Setting the time derivatives equal to zero in the modulation equations, results in the equilibrium (stationary) equations in the Cartesian form. The stability of stationary points, points where $\dot{x}_p = 0$, $\dot{y}_q = 0$, $\dot{x}_p = 0$, and $\dot{y}_p = 0$, is resolved by computing and evaluating the eigenvalues of the Jacobian matrix defined by

$$
\text{Jacobian} = \begin{bmatrix}
\frac{\partial f_1}{\partial x_q} & \frac{\partial f_1}{\partial y_q} & \frac{\partial f_1}{\partial x_p} & \frac{\partial f_1}{\partial y_p}\\
\frac{\partial f_2}{\partial x_q} & \frac{\partial f_2}{\partial y_q} & \frac{\partial f_2}{\partial x_p} & \frac{\partial f_2}{\partial y_p}\\
\frac{\partial f_3}{\partial x_q} & \frac{\partial f_3}{\partial y_q} & \frac{\partial f_3}{\partial x_p} & \frac{\partial f_3}{\partial y_p}\\
\frac{\partial f_4}{\partial x_q} & \frac{\partial f_4}{\partial y_q} & \frac{\partial f_4}{\partial x_p} & \frac{\partial f_4}{\partial y_p}
\end{bmatrix}
\tag{4.51}
$$

at the stationary points. Equilibrium (stationary) solutions with corresponding eigenvalues with negative real parts are asymptotically stable while others with at least one positive eigenvalue represent an unstable solution.

4.4 Frequency-Response Analysis

The frequency-response plots are produced for the steady state solutions of the modulation equations, (4.41)-(4.44). The basic parameters under consideration are given in Table 3.1. The width ratio of the end mass to the beam is 15 and the eccentricity is 0.1. The excitation frequency, Ω_e, is perturbed apropos of the apparent natural frequency ω_q, see equation (4.28). The other natural frequency, ω_p, is characterized with respect to the ω_q as well. In Table 4.1, the values of effective natural frequencies, ω_q and ω_p, are provided for two sets of DC bias loadings.

Table 4.1: DC loadings and the effective natural frequencies

	V_w (V)		V_v (V)	
	3	10.731	3	10.731
ω_q (Hz)	20542.8	20340.4	N/A	N/A
ω_p (Hz)	N/A	N/A	20340.4	20139.9

The effective nonlinearity of the amplitude equation, equation (4.41), is given by

$$\tau = \frac{1}{4}(G_1 + 2G_2)(3Q_{13}q_s + Q_{12}) + \frac{3}{8}Q_{13} - \frac{1}{8}\omega_q^2\left((5G_1 + 2G_2)(2Q_2q_s + Q_1) + 3Q_2\right) \tag{4.52}$$

To investigate the evolution of the effective nonlinearity for the geometry of interest the DC voltage is increased from zero to just above the pull-in voltage. The nonlinearity is initially negative and very small in magnitude and becomes larger and more negative as the DC voltage approaches the static pull-in voltage indicating the softening characteristics of the response in the drive direction, see Figure 4.1. Considering the center frequency to be equal to ω_q, two cases are investigated in the following analysis: the case of matched DC voltage and the matched natural frequencies.

4.4.1 Matched Natural Frequencies

In operating the beam gyroscope as a rotation rate sensor in the amplitude-modulation mode, the natural frequencies of the sense and drive directions are matched to increase the sensitivity of the device. To this end, the DC loadings are selected as $V_w = 10.731\,\text{V}$ and $V_v = 3\,\text{V}$ to set the frequencies at 20340.4 Hz. In the design of the gyroscope, the bandwidth of the sense direction

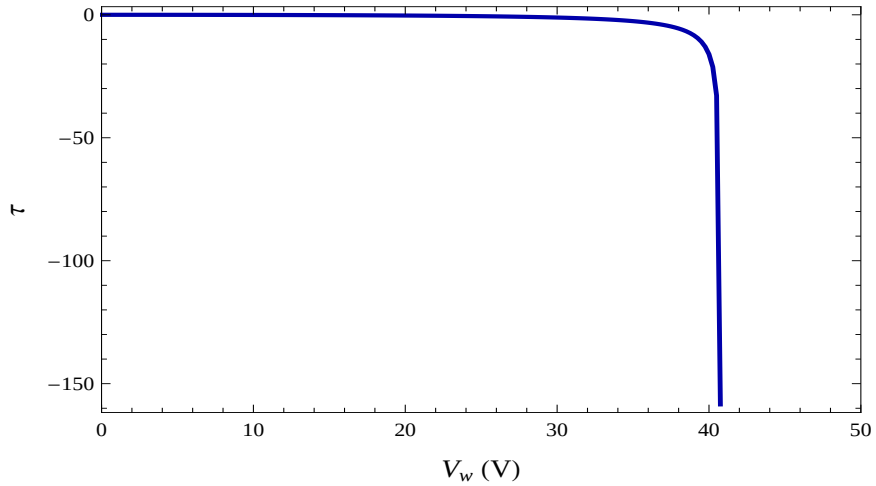

Figure 4.1: The variation of effective nonlinearity with the DC voltage.

$$BW = \frac{\omega_n}{Q} \tag{4.53}$$

where ω_n (Hz) is the natural frequency of the free vibration in the sense direction and Q is the quality factor, is a parameter under consideration by designers. For a bandwidth of 50 Hz, the quality factor is about 400.

In Figures 4.2(a)-4.2(f), the frequency-response plots are demonstrated for an increasing set of AC voltages. The nondimensional responses in the drive and sense direction, see equation (2.65), are plotted for the center of the rigid body. For low excitation amplitude, $V_{\text{AC}} = 0.3$V, the response is completely linear and single-valued. By increasing the excitation amplitude to 0.7 V and then 1.2 V, an unstable branch of response appears in the frequency-response plots. The horizontal solid line represents the physical limit where the end of the structure strikes the substrate. The horizontal dotted-dashed line goes through the static unstable equilibrium for the corresponding DC loading, see Figures 3.3(a).

Figures 4.3(a)-4.3(f) demonstrate the variation in the frequency-response of the system as the rotation rate is increased to the magnitude of 18000°/s or 50 revolutions per second (Hz). It is expected to observe the higher effect of the Coriolis force in the form of the sense response. The maximum displacement in the sense direction increases from 0.442% to 3.617% of the initial gap size for an increase in the angular rotation rate from $\Omega = 180$°/s to $\Omega = 1800$°/s. On the other hand, the modal frequencies diverge from each other as the rotation rate increases. Although initially the modal frequencies are matched by manipulating the DC voltages, the higher the rotation rate the larger the difference of modal frequencies becomes and appears as two separate peaks in the frequency-response plot, see Figure 4.3(e) and 4.3(f).

4.4.2 Matched DC Voltages

When operating the gyroscope in the frequency-modulation mode, measuring the amplitude of the sense displacement is not of primary interest. As a consequence, the bandwidth of the sensor is not restricted by the quality factor. In principle, the bandwidth is limited by the natural frequency of the microsensor which is several orders of magnitude larger than the highest input rotation rate, see Chapter 3. The quality factor is set to 400 and the rotation rate to 18°/s. For varying excitation amplitude, the frequency-response plots are provided in Figures 4.4(a)-4.4(f). The low DC potential prevents the structure from large displacements and thus nonlinearity due to electrostatic force does not affect the response.

The DC voltages are increased to 10.731 V for results of Figures 4.5(a)-4.5(f). Note that the product of V_w and V_{AC}, see equations (4.41) and (4.43), gives the excitation amplitude on the slowly varying system. The angular rotation rate is set to 18°/s. For displacements larger than the 35% of the initial distance between the rigid body and the corresponding electrode (the gap size), the response becomes nonlinear and multi-valued.

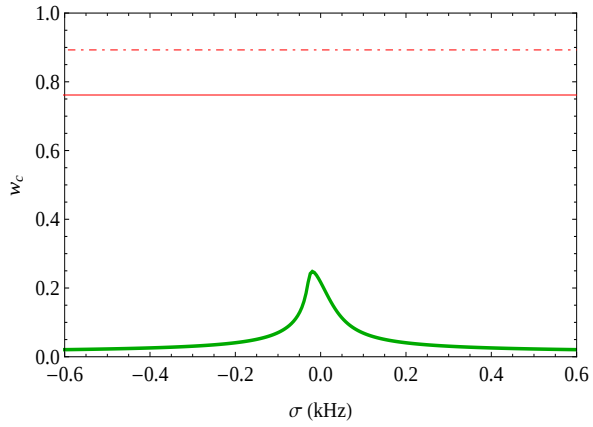

(a) Drive direction ($V_{\mathrm{AC}} = 0.3\mathrm{V}$)

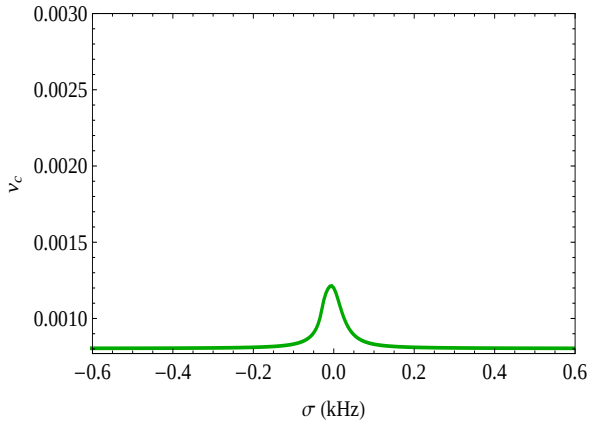

(b) Sense direction ($V_{\mathrm{AC}} = 0.3\mathrm{V}$)

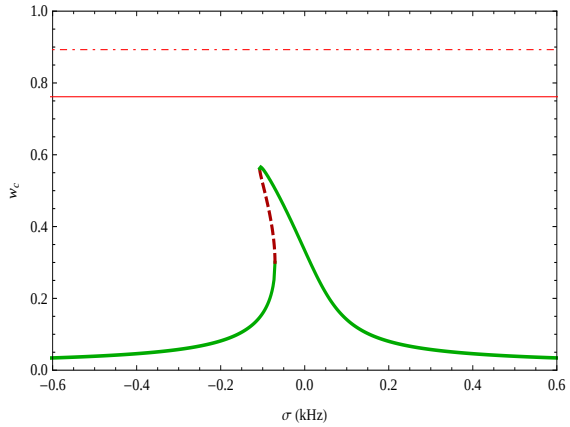

(c) Drive direction ($V_{\mathrm{AC}} = 0.7\mathrm{V}$)

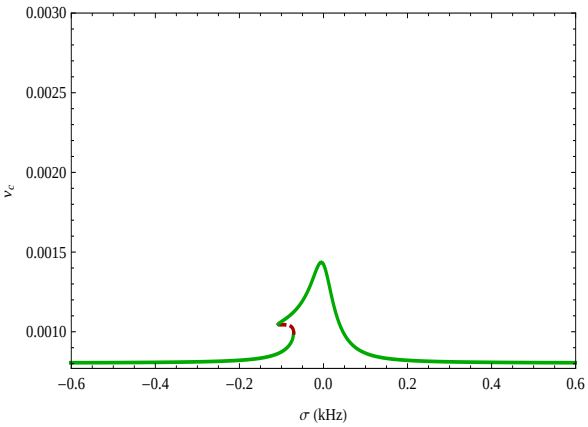

(d) Sense direction ($V_{\mathrm{AC}} = 0.7\mathrm{V}$)

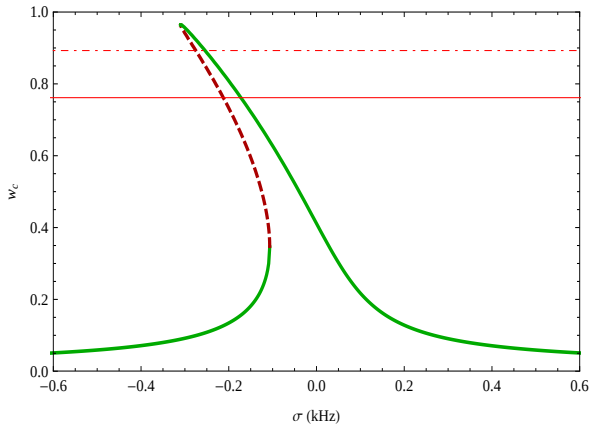

(e) Drive direction ($V_{\mathrm{AC}} = 1.2\mathrm{V}$)

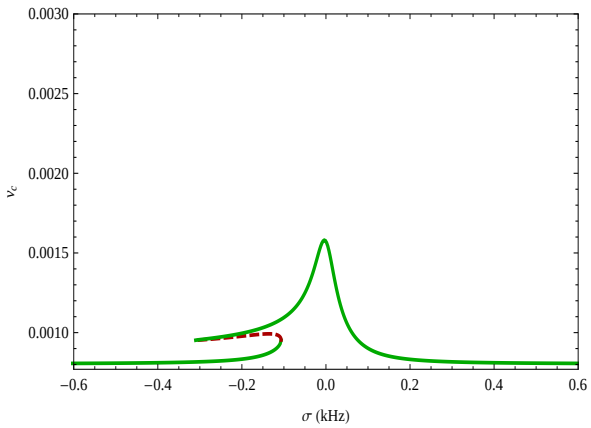

(f) Sense direction ($V_{\mathrm{AC}} = 1.2\mathrm{V}$)

Figure 4.2: The frequency-response plots for varying V_{AC}, the solid red horizontal line indicates the physical limit of the displacement and the dashed-dot line represents the static saddle line through saddle node for the corresponding V_w ($V_w = 10.731\,\mathrm{V}$, $V_v = 3\,\mathrm{V}$, $\Omega = 18^\circ/\mathrm{s}$).

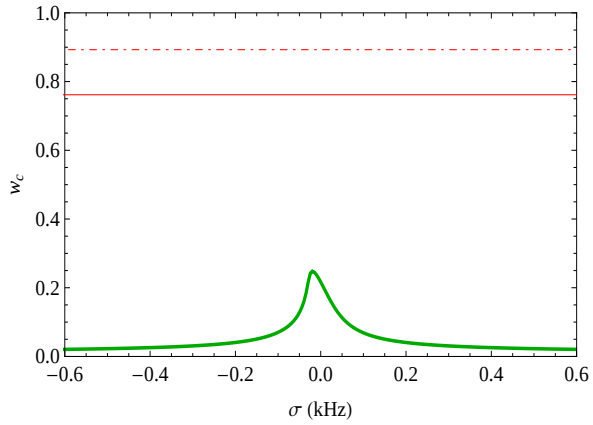

(a) Drive direction ($\Omega = 180°/s$)

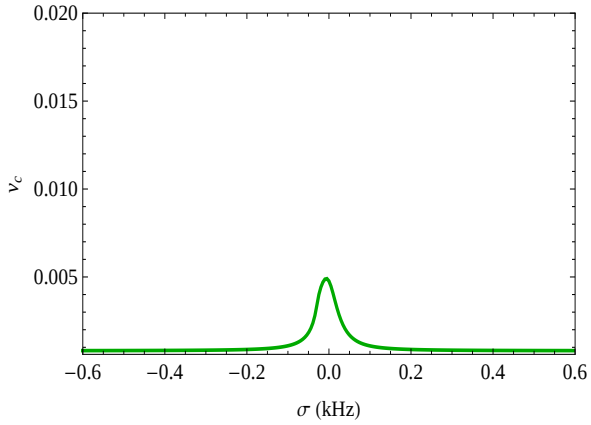

(b) Sense direction ($\Omega = 180°/s$)

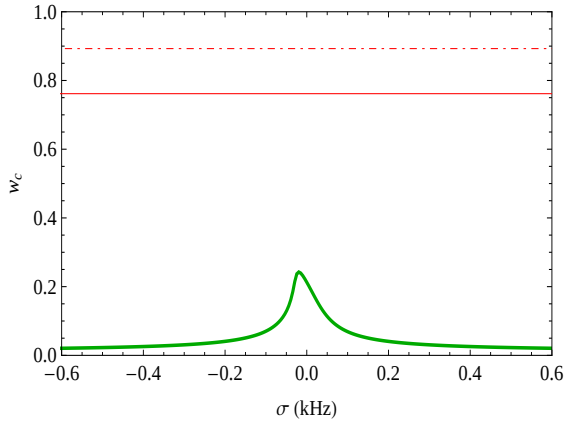

(c) Drive direction ($\Omega = 1800°/s$)

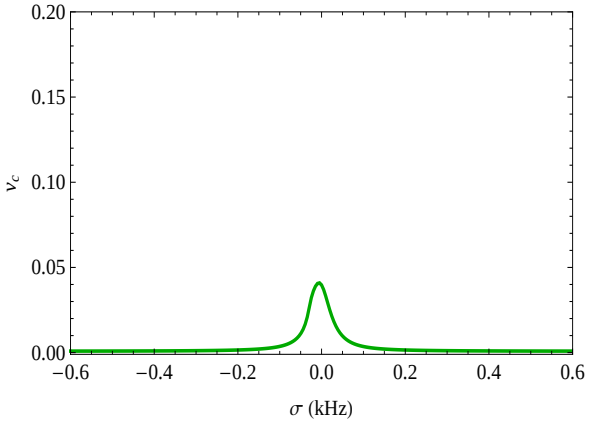

(d) Sense direction ($\Omega = 1800°/s$)

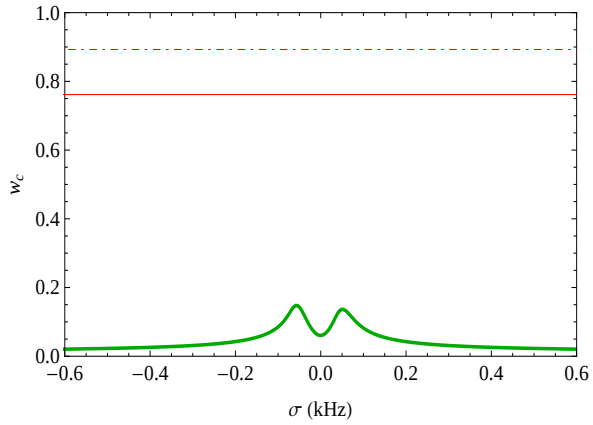

(e) Drive direction ($\Omega = 18000°/s$)

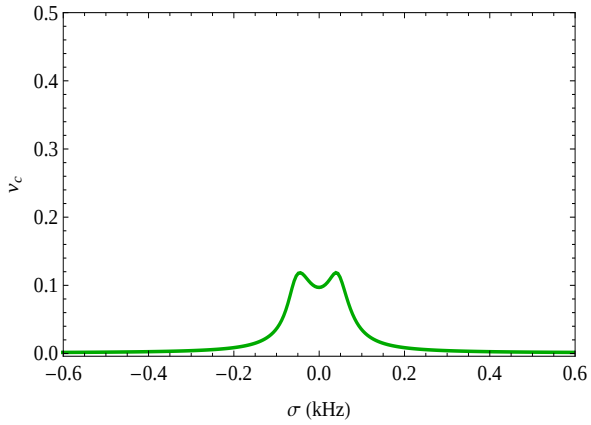

(f) Sense direction ($\Omega = 18000°/s$)

Figure 4.3: The frequency-response plots for $V_{\text{AC}} = 0.3\,\text{V}$ varying Ω, the solid red horizontal line indicates the physical limit of the displacement and the dashed-dot line represents the static saddle line through saddle node for the corresponding V_w ($V_w = 10.731\,\text{V}$, $V_v = 3\,\text{V}$).

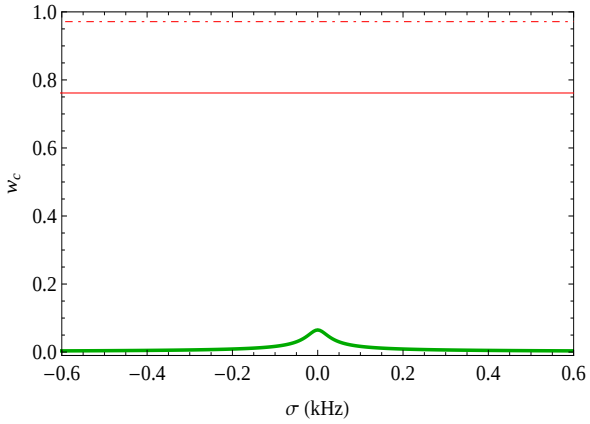

(a) Drive direction ($V_{\mathrm{AC}} = 0.3\mathrm{V}$)

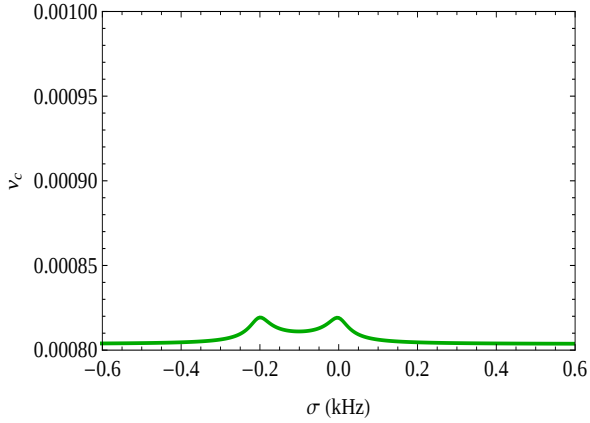

(b) Sense direction ($V_{\mathrm{AC}} = 0.3\mathrm{V}$)

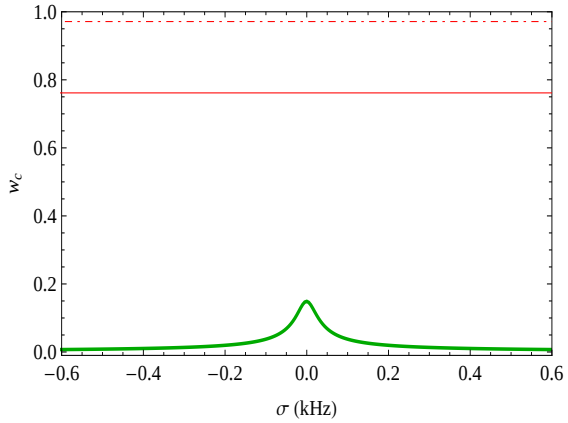

(c) Drive direction ($V_{\mathrm{AC}} = 0.7\mathrm{V}$)

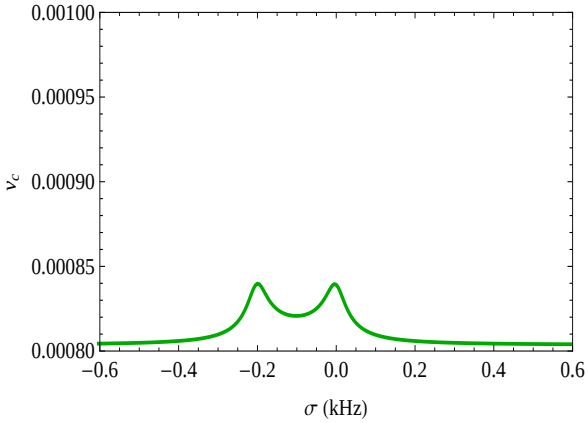

(d) Sense direction ($V_{\mathrm{AC}} = 0.7\mathrm{V}$)

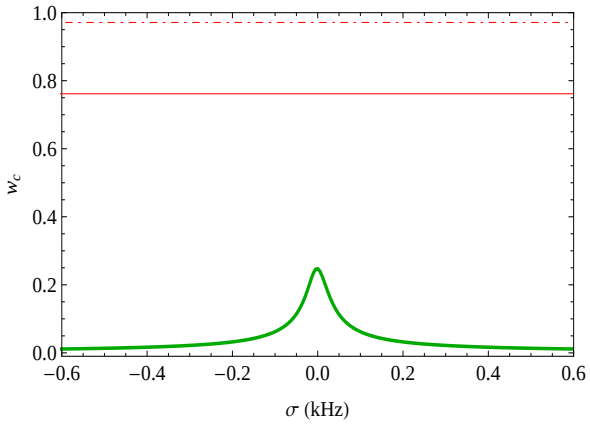

(e) Drive direction ($V_{\mathrm{AC}} = 1.2\mathrm{V}$)

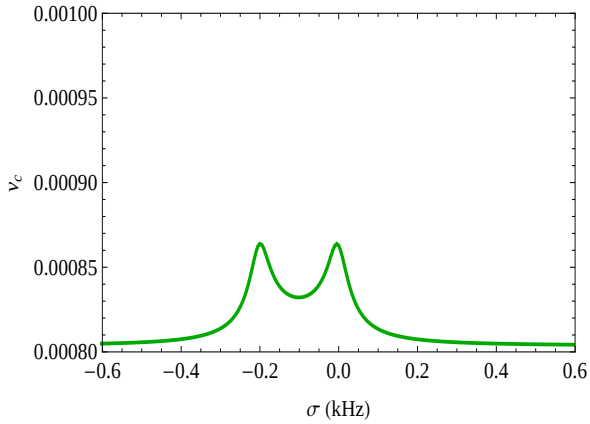

(f) Sense direction ($V_{\mathrm{AC}} = 1.2\mathrm{V}$)

Figure 4.4: The frequency-response plots for varying V_{AC}, the solid red horizontal line indicates the physical limit of the displacement and the dashed-dot line represents the static saddle line through saddle node for the corresponding V_w ($V_w = 3\,\mathrm{V}$, $V_v = 3\,\mathrm{V}$, $\Omega = 18^\circ/\mathrm{s}$)

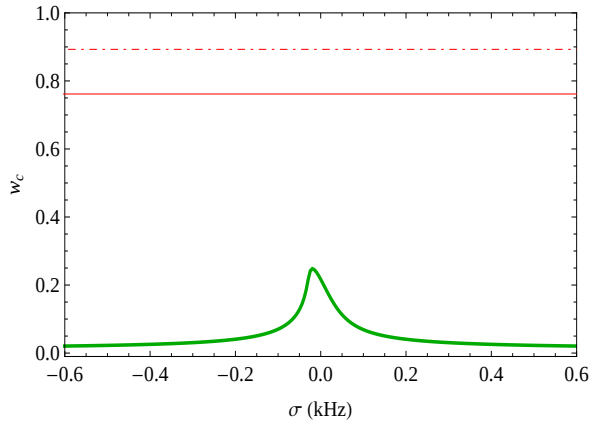

(a) Drive direction ($V_{\mathrm{AC}} = 0.3\mathrm{V}$)

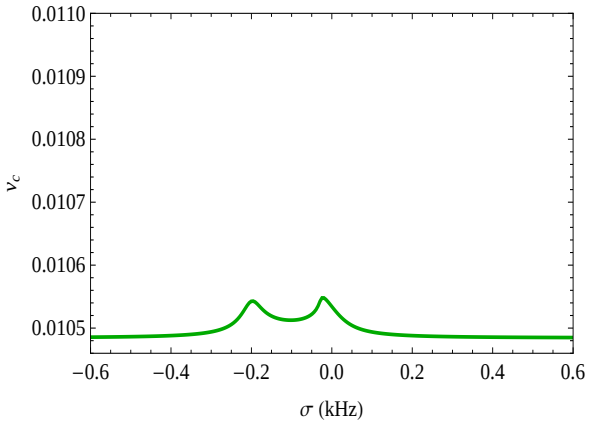

(b) Sense direction ($V_{\mathrm{AC}} = 0.3\mathrm{V}$)

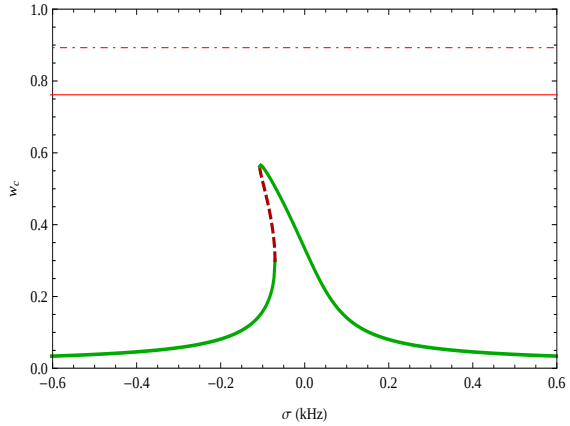

(c) Drive direction ($V_{\mathrm{AC}} = 0.7\mathrm{V}$)

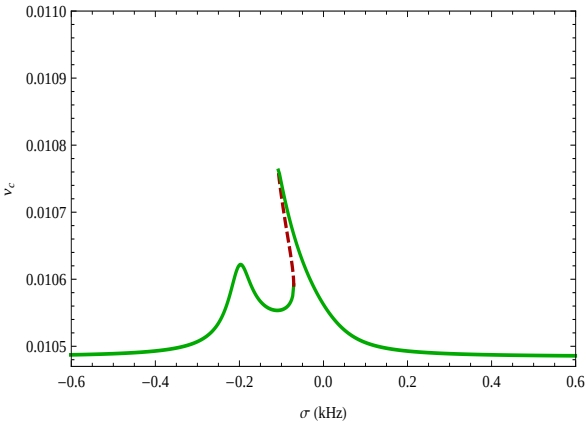

(d) Sense direction ($V_{\mathrm{AC}} = 0.7\mathrm{V}$)

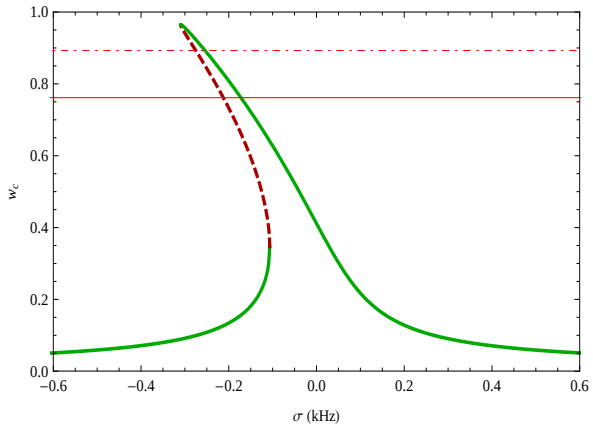

(e) Drive direction ($V_{\mathrm{AC}} = 1.2\mathrm{V}$)

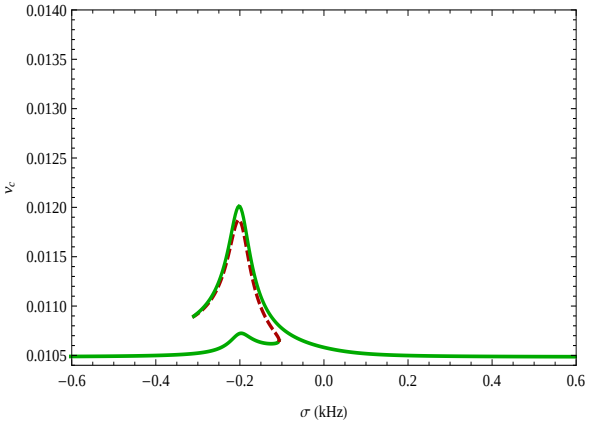

(f) Sense direction ($V_{\mathrm{AC}} = 1.2\mathrm{V}$)

Figure 4.5: The frequency-response plots for varying V_{AC}, the solid red horizontal line indicates the physical limit of the displacement and the dashed-dot line represents the static saddle line through saddle node for the corresponding V_w ($V_w = 10.731\,\mathrm{V}$, $V_v = 10.731\,\mathrm{V}$, $\Omega = 18^\circ/\mathrm{s}$).

4.5 Force-Response Analysis

The force-response analysis is performed on the nonlinear multi-valued cases of matched natural frequencies and matched DC loads. For the frequency-response plots in Figures 4.2(e) and 4.5(e), with the detuning parameter $\sigma = -0.245$ kHz, the force-response plots are given in Figures 4.6(a)-4.6(d). Increasing V_{AC}, the first bifurcation point where the response loses stability is 1.888 V in both cases. And the second turning point is at 0.822 V in both cases, indicating similar behavior in terms of bifurcation points for both matched frequency and matched DC voltage cases. In agreement with the frequency-response results, the upper stable, branch in the case of matched DC voltages, appears to be larger than its counterpart in the frequency matched case.

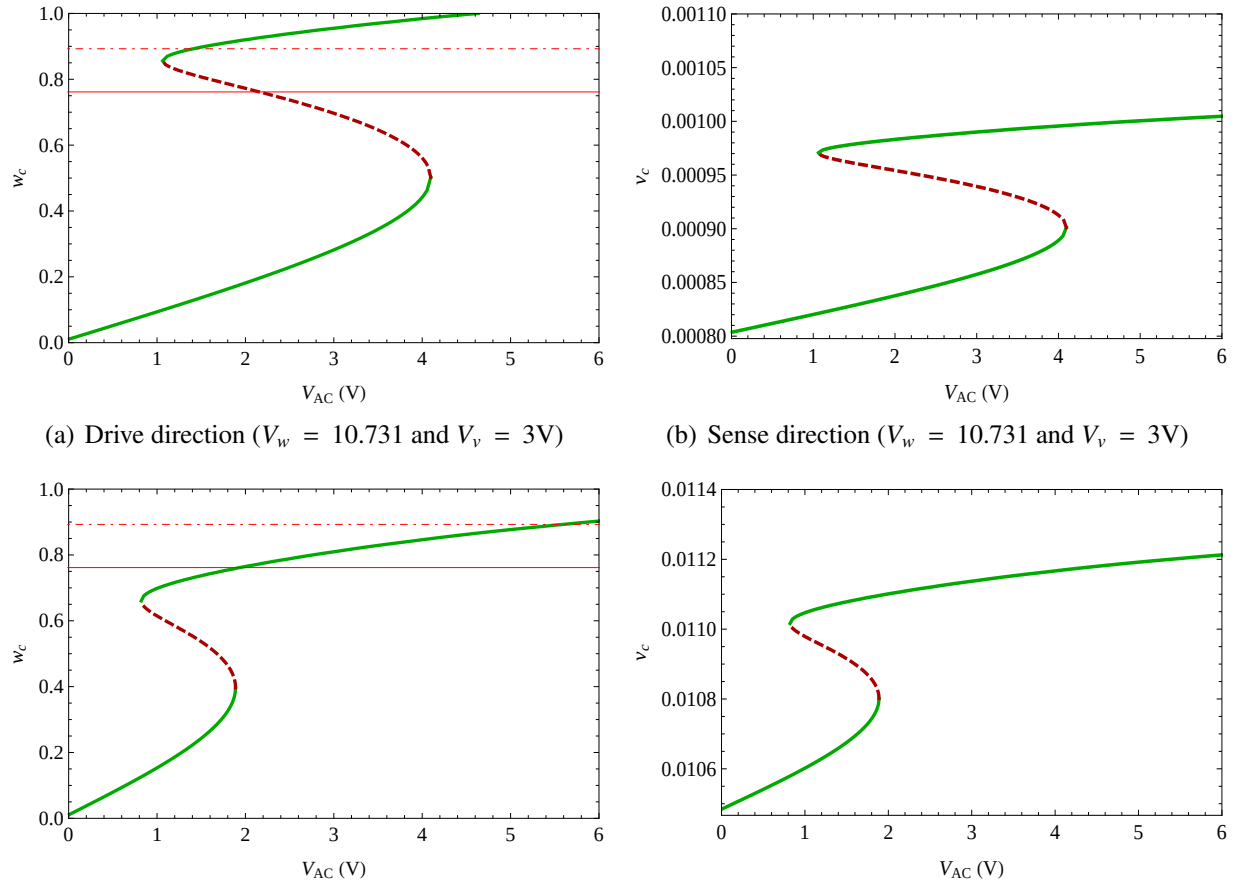

(a) Drive direction ($V_w = 10.731$ and $V_v = 3$V)

(b) Sense direction ($V_w = 10.731$ and $V_v = 3$V)

(c) Drive direction ($V_w = 10.731$ and $V_v = 10.731$V)

(d) Sense direction ($V_w = 10.731$ and $V_v = 10.731$V)

Figure 4.6: The force-response plots for $\sigma = -0.147$kHz, the solid red horizontal line indicates the physical limit of the displacement and the dotted-dashed line represents the static saddle line through saddle node for the corresponding V_w ($V_w = 10.731$ V, $V_v = 3$ V, $\Omega = 18°/\text{s}$).

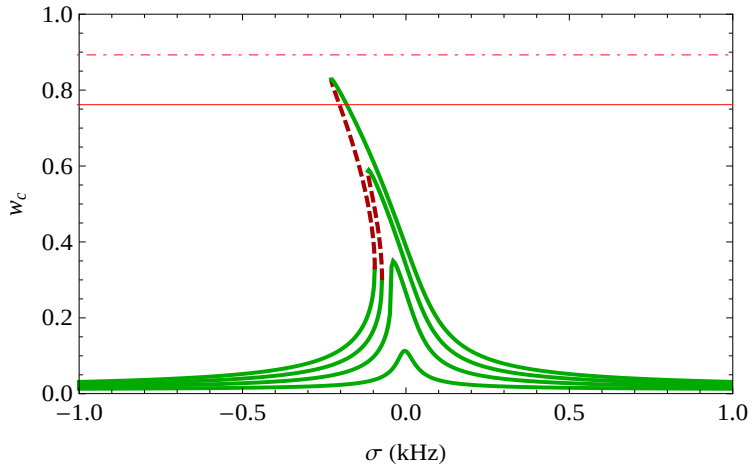

(a) Drive direction, increasing V_{AC}

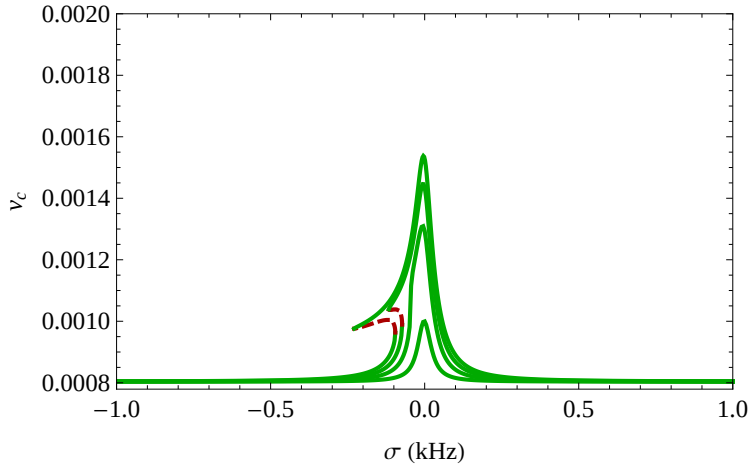

(b) Sense direction, increasing V_{AC}

Figure 4.7: The frequency-response plots for varying V_{AC} ($V_w = 10.731$ V, $V_v = 3$ V, $\Omega = 18°/\mathrm{s}$).

4.6 The Effects of the AC Voltage and the Quality Factor

Figures 4.7(a) and 4.7(b) show the variation of the frequency-response plots with the excitation amplitude V_{AC}. As the excitation amplitude increases the maximum response steadily grows and becomes nonlinear for sufficiently large V_{AC}. The frequency-response curves are given for $V_{\mathrm{AC}} = 0.13$V, 0.43 V, 0.73 V, and 1.03 V where the response is fully linear for the lowest two AC voltages and at the onset of multivaluedness for $V_{\mathrm{AC}} = 0.43$ V. In the sense direction, Figure 4.7(b), an unstable branch appears for $V_{\mathrm{AC}} = 0.73$ V and $V_{\mathrm{AC}} = 1.03$ V, see the dashed (red) lines. For $V_{\mathrm{AC}} = 1.03$ V part of the response near the peak is beyond the physical limit of the device for this geometry indicated by the solid horizontal line. Increasing the V_{AC} amplifies the effect of nonlinearity and a stronger softening behaviour is observed in the drive direction as the

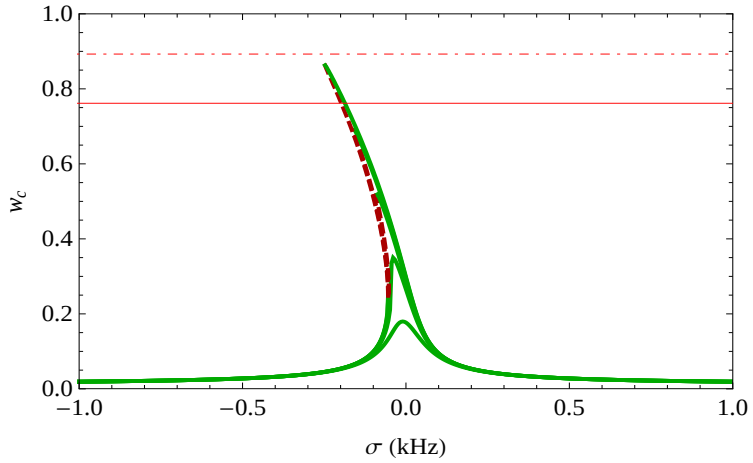

(a) Drive direction, increasing Q

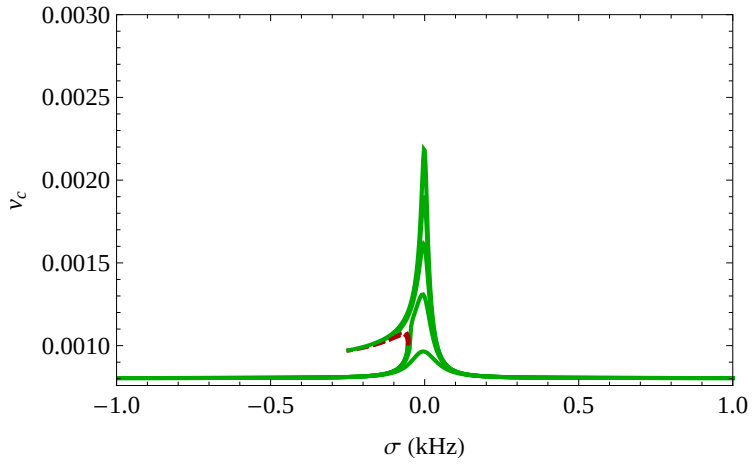

(b) Sense direction, increasing Q

Figure 4.8: The frequency-response plots for varying qualify factor Q ($V_w = 10.731\,\text{V}$, $V_v = 10.731\,\text{V}$, $\Omega = 18^\circ/\text{s}$).

consequence of large amplitude of vibration.

In Figures 4.8(a) and 4.8(b) for $V_{\text{AC}} = 0.43\,\text{V}$, the frequency curves are plotted for some different quality factors. The quality factor is 200 for the smallest maximum amplitude of vibration in the drive direction and 1000 for the largest amplitude of vibration. The curves are for $Q = 200$, 400, 600, 800, and 1000. The amplitude constantly grows with the quality factor and the peak response region becomes sharper indicating a lower bandwidth. Therefore, for operating in the amplitude-modulation mode, the required bandwidth limits the quality factor. In the design of the gyroscope sensor, modifying the geometry of the end rigid body results in a higher or lower natural frequency which affects the quality factor for the desired bandwidth.

4.7 Summary

In this chapter, the non/linear dynamics of the second-order approximation of the discretized model have been studied using the method of multiple scales. The Coriolis terms have been considered while higher order centrifugal terms have been neglected. The excitation, damping, and Coriolis terms appear in the third-order equations of motion. Removing the secular terms, the modulation equations are computed and the equilibrium points and their stability are determined. Controlling the DC voltage, the effective eigenvalues are matched in the drive and sense directions to increase the sensitivity of the sensor. For equal DC voltages in the drive and sense directions, while the response in the drive direction is similar to the matched-frequency case, the sense response indicates the synchronization of two frequencies near the excitation frequency.

Chapter 5

Computational Nonlinear Analysis

5.1 Preview

The nonlinear dynamics of full single-mode model are investigated in this chapter. To this end, the effects of the second-order rotation rate Ω^2 and the excitation amplitude V_{AC}^2 are taken into consideration. When exciting the structure using the electrostatic method, the nonlinearity appears in the denominator of the actuation force term. To operate the sensor in the primary resonance range, the excitation frequency is set near the effective natural frequency of the structure.

To study the nonlinear resonance of the complete reduced-order model, the shooting method is used. The nonlinear reduced-order model is re-cast into the state space form and the shooting method is used to transform the initial value of finding periodic solutions to the boundary value problem of matching initial conditions and end conditions. The stability of each response branch is determined by computing Floquet multipliers, see Section 1.5.2. Therefore, the monodromy matrix is computed and its eigenvalues are monitored for their exit from the unit circle on the complex plane.

5.2 Computational Method

The analysis is performed on the reduced-order model of equations (2.75) and (2.76). The equations are repeated here:

$$
\begin{aligned}
&\Delta\left(\Gamma+\alpha\,\Gamma'+\underset{M}{J}_{\eta\eta}\,\psi'(1)^2+M\,\left(\psi(1)+e\,\psi'(1)\right)^2\right)\ddot{q}(t)+c_q\,\dot{q}(t)\\
&+\Delta\,\Omega(t)\left(2\,\Pi-\left(\underset{M}{J}_{\xi\xi}-\underset{M}{J}_{\eta\eta}-\underset{M}{J}_{\zeta\zeta}\right)\phi'(1)\psi'(1)+2\,M\,\left(\phi(1)+\,e\,\phi'(1)\right)\left(\psi(1)+e\,\psi'(1)\right)\right)\dot{p}(t)\\
&+\Delta\,\dot{\Omega}(t)\left(\Pi+\alpha\Pi'+\underset{M}{J}_{\eta\eta}\,\psi'(1)\,\phi'(1)+\,M\,\left(\phi(1)+\,e\,\phi'(1)\right)\left(\psi(1)+e\,\psi'(1)\right)\right)p(t)
\end{aligned}
$$

$$+\Delta\left(\Gamma''-\Omega^2\left(\Gamma-\alpha\,\Gamma'+M\,\left(\psi(1)+\,e\,\psi'(1)\right)^2-\underset{M}{J}_{\xi\xi}\,\psi'(1)^2+\underset{M}{J}_{\zeta\zeta}\,\psi'(1)^2\right)\right)q(t)=$$

$$\frac{\nu\,e\,(\psi(1)+e\,\psi'(1))\,V_w^2}{(1-\,q(t)\,\psi(1)-e\,q(t)\psi'(1))^{\,2}} \tag{5.1}$$

and

$$\Delta\left(\Lambda+\alpha\,\Delta^2\,\Lambda'+\underset{M}{J}_{\zeta\zeta}\,\phi'(1)^2+M\,\left(\phi(1)+e\,\phi'(1)\right)^2\right)\ddot{p}(t)+c_p\,\dot{p}(t)$$

$$-\Delta\,\Omega(t)\left(2\,\Pi+\left(\underset{M}{J}_{\eta\eta}+\underset{M}{J}_{\zeta\zeta}-\underset{M}{J}_{\xi\xi}\right)\phi'(1)\psi'(1)+2M\,\left(\psi(1)+e\,\psi'(1)\right)\left(\phi(1)+e\,\phi'(1)\right)\right)\dot{q}(t)$$

$$-\Delta\,\dot{\Omega}(t)\left(\Pi-\alpha\Pi'+\left(\underset{M}{J}_{\zeta\zeta}-\underset{M}{J}_{\xi\xi}\right)\psi'(1)\,\phi'(1)+\,M\,\left(\phi(1)+\,e\,\phi'(1)\right)\left(\psi(1)+e\,\psi'(1)\right)\right)q(t)$$

$$+\Delta\left(\Delta^2\,\Lambda''-\Omega^2\left(\Lambda-\alpha\,\Delta^2\,\Lambda'+M\,\left(\phi+e\,\phi'(1)\right)^2-\underset{M}{J}_{\xi\xi}\,\phi'(1)^2+\underset{M}{J}_{\eta\eta}\,\phi'(1)^2\right)\right)p(t)=$$

$$\frac{\nu\,e\,(\phi(1)+e\,\phi'(1))\,V_v^2}{(1-\,p(t)\phi(1)-e\,\,p(t)\phi'(1))^{\,2}} \tag{5.2}$$

where the $\hat{(\,)}$'s have been removed for the notational clarity. To re-express the equations in the state space form, it is assumed that $x_1 = q(t)$, $x_2 = \dot{q}(t)$, $x_3 = p(t)$, and $x_4 = \dot{p}(t)$ resulting in

$$\dot{x}_1=x_2 \tag{5.3}$$

$$\dot{x}_2=\frac{1}{m_q}\left(-c_q\,x_2-\Delta\left(\Gamma''-\Omega^2\left(\Gamma-\alpha\,\Gamma'+M\,\left(\psi(1)+\,e\,\psi'(1)\right)^2+\left(\underset{M}{J}_{\zeta\zeta}-\underset{M}{J}_{\xi\xi}\right)\psi'(1)^2\right)\right)x_1\right.$$

$$-\Delta\,\dot{\Omega}(t)\left(\Pi+\alpha\Pi'+\underset{M}{J}_{\eta\eta}\,\psi'(1)\,\phi'(1)+\,M\,\left(\phi(1)+\,e\,\phi'(1)\right)\left(\psi(1)+e\,\psi'(1)\right)\right)x_3$$

$$-\Delta\,\Omega(t)\left(2\,\Pi-\left(\underset{M}{J}_{\xi\xi}\,-\underset{M}{J}_{\eta\eta}-\underset{M}{J}_{\zeta\zeta}\right)\phi'(1)\psi'(1)+2\,M\,\left(\phi(1)+\,e\,\phi'(1)\right)\left(\psi(1)+e\,\psi'(1)\right)\right)x_4 \tag{5.4}$$

$$\left.+\frac{\nu\,e\,(\psi(1)+e\,\psi'(1))\,V_w^2}{(1-x_1\,\psi(1)-e\,x_1\psi'(1))^{\,2}}\right)$$

$$\dot{x}_3=x_4 \tag{5.5}$$

$$\dot{x}_4=\frac{1}{m_p}\left(-c_p\,x_3-\Delta\left(\Delta^2\,\Lambda''-\Omega^2\left(\,\Lambda-\alpha\,\Delta^2\,\Lambda'+M\,\left(\phi+e\,\phi'(1)\right)^2+\left(\underset{M}{J}_{\eta\eta}-\underset{M}{J}_{\xi\xi}\right)\phi'(1)^2\right)\right)x_3\right.$$

$$+\Delta\,\Omega(t)\left(2\,\Pi+\left(\underset{M}{J}_{\eta\eta}+\underset{M}{J}_{\zeta\zeta}-\underset{M}{J}_{\xi\xi}\right)\phi'(1)\psi'(1)+2M\,\left(\psi(1)+e\,\psi'(1)\right)\left(\phi(1)+e\,\phi'(1)\right)\right)x_2$$

$$+\Delta\,\dot{\Omega}(t)\left(\Pi-\alpha\Pi'+\left(\underset{M}{J}_{\zeta\zeta}-\underset{M}{J}_{\xi\xi}\right)\psi'(1)\,\phi'(1)+\,M\,\left(\phi(1)+\,e\,\phi'(1)\right)\left(\psi(1)+e\,\psi'(1)\right)\right)x_1$$

$$+\frac{\nu\, e\,(\phi(1)+e\,\phi'(1))\,V_v^2}{(1-\ x_3\phi(1)-e\ x_3\phi'(1))^{\,2}}\Bigg) \tag{5.6}$$

where m_q and m_p are the coefficients of the modal acceleration terms $\ddot{p}(t)$ and $\ddot{q}(t)$ in equations (5.1) and (5.2). The damping coefficients c_q and c_p are replaced with the $m_q\,\omega_D/Q_D$ and $m_p\,\omega_S\,/Q_S$ respectively, ω_D and ω_S are the natural frequency in the drive and sense directions (for zero DC voltages), and Q_D and Q_S are the quality factors in the drive and sense directions respectively.

To locate periodic solutions of the response, a combination of long time integration and shooting method is used. The shooting method is employed to locate the periodic solutions of the non/autonomous nonlinear systems. The method of implementation and the algorithm are discussed in [59], pp. 120-121, and [63], pp. 38-41. To determine the stability of periodic orbits, the eigenvalues of the monodromy matrix are computed, see Section 1.5.2.

5.3 Frequency-Response Analysis

In the analysis of the system response using the method of multiple scales, the higher order nonlinearities and the second-order angular velocity and excitation amplitude, $V_{\rm AC}^2$ were neglected as they appear in higher order equations of motion. In computing the response of the system using the computational shooting method, the nonlinearities of the electrostatic force and higher order angular rotation rate and the excitation amplitude affect the dynamic equilibrium of the structure for relatively large displacements.

5.3.1 Matched Natural Frequencies

In Figures 5.1(a)-5.1(f) the results of computational analysis are compared with the perturbation method for matched natural frequencies, see Table 4.1. The DC voltages are set to 10.731 V in the drive direction and 3 V in the sense direction. The applied AC excitation voltage is increased from 0.3 V to 1.2 V for Figures 5.1(a)-5.1(f). The circles represent the perturbation solution obtained by using the method of multiple scales. It has been mentioned earlier that in operating the gyroscope as rotation rate sensor in the amplitude-modulation mode, the matched natural frequencies case is highly desired to increase the sensitivity of the system.

In Figures 5.1(a) and 5.1(b) the response is linear and single-valued. It is observed that the perturbation result is in excellent agreement with the computational shooting method. As the excitation amplitude grows, the response becomes larger and the agreement between the computational and perturbation solutions degrades. Figures 5.1(c) and 5.1(d), compare two solutions for $V_{\rm AC}\ =\ 0.7$V. The lower stable branch for frequencies less than the effective natural frequency is approximated closely by both methods. For less than 60% of the total gap size, the perturbation method agrees with the computational method for upper stable branch.

Figures 5.1(e) and 5.1(f), present the frequency-response plots for $V_{\rm AC}\ =\ 1.2$V. Comparing with previous case for $V_{\rm AC}\ =\ 0.7$V, it is seen that the difference between the perturbation and computational predictions becomes larger for the unstable branch (indicated with dashed red line and

red circles). The method of multiple scales tend to overestimate the larger response branches. However, the bifurcation points do not differ significantly. For practical purposes, operating in the highly nonlinear region is not advised by virtue of higher failure possibilities. Therefore, the results of the second-order perturbation analysis remain close to those of the computational analysis.

The next set of results, Figures 5.2(a)-5.2(f), demonstrate and compare the effect of an increasing Ω on the frequency-response plot. The corresponding AC voltage is 0.3 V is low enough to ensure the linearity of the response in all cases. In all cases, the results of the perturbation analysis using the method of multiple scales are in excellent agreement with those of the computational shooting analysis. Increasing the rotation rate to the large magnitude of 18000°/s (or 50 Hz) affect the modal frequencies of both drive and sense directions.

5.3.2 Matched DC Voltages

Operating the gyroscopic sensor in the frequency-modulation mode does not require amplitude amplification, and thus modal frequency matching. Two sets of results are presented here for low and high DC voltages. The low DC loading weakens the combined effect of AC and DC loadings and results in a single-valued response in all cases. Figures 5.3(a)-5.3(f), provide the comparison of the computational and perturbation solutions for $V_v = V_w = 3$ V. Qualitative and quantitative agreements are obtained comparing the two methods of computations.

Two peaks appear at the effective modal frequencies in the sense direction. The external excitation force is large enough to prevail over the feedback due to the Coriolis force to the drive direction and create a single maximum in the drive mode for all common rotation rate sensors. It is realized that in all cases, the perturbation solution firmly agrees with the computational results. Employing the gyroscope in the frequency-modulation mode, the desired amplitude is as large as required to identify two peaks. A low V_{AC} results in the lower effect of V_{AC}^2 on the response.

Figures 5.4(a)-5.4(f) illustrate the frequency-response plots for $V_v = V_w = 10.731$ V. Because of the large DC voltage, an unstable branch of response appears for $V_{\text{AC}} = 0.7$V and $V_{\text{AC}} = 1.2$V. The accuracy of the perturbation solution degrades in estimating the unstable branch and the higher stable branch as the excitation amplitude grows. However, qualitatively the perturbation solution depicts the same synchronization behavior in the sense mode for $V_{\text{AC}} = 1.2$.

5.4 Force-Response Analysis

The force-response curves are depicted in Figures 5.5(a) and 5.5(b) for the case of matched natural frequencies. Increasing the excitation amplitude, the perturbation and computational solutions agree up to $V_{\text{AC}} = 1.6$ V where they start to differ gradually. The semi-analytical perturbation solution overestimates the AC voltage and the displacement at the first turning point. It continues to overestimate the corresponding unstable and the higher stable equilibrium points. According to the computational shooting method, the first bifurcation (turning) point occurs when $V_{\text{AC}} = 2.479$ V at 33.6% of the initial gap size, while the method of multiple scale gives $V_{\text{AC}} = 4.096$ V at 50.2% for the same point.

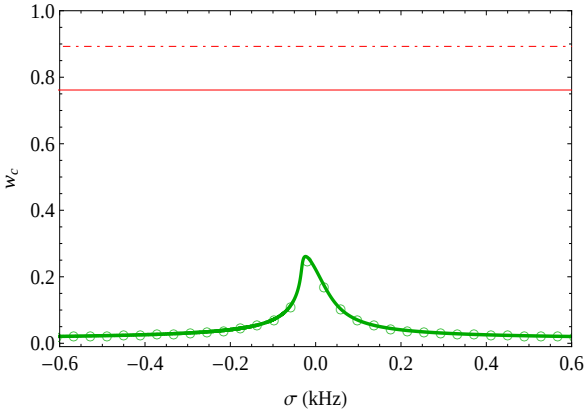

(a) Drive direction ($V_{\mathrm{AC}} = 0.3$V)

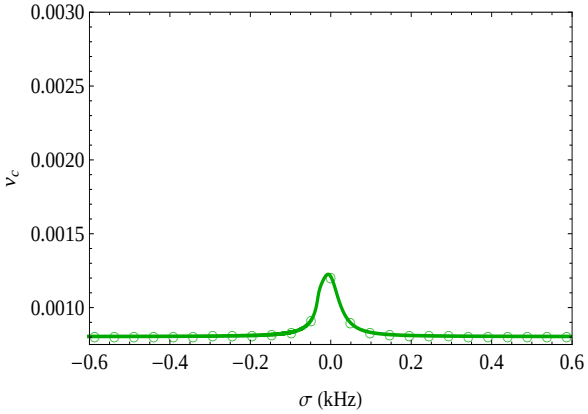

(b) Sense direction ($V_{\mathrm{AC}} = 0.3$V)

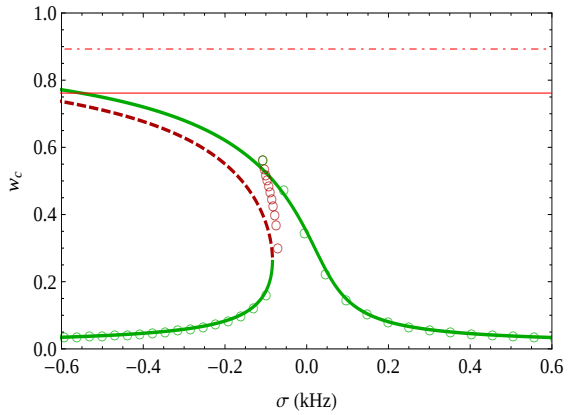

(c) Drive direction ($V_{\mathrm{AC}} = 0.7$V)

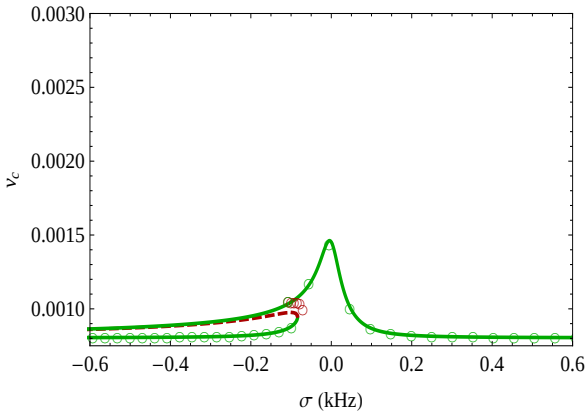

(d) Sense direction ($V_{\mathrm{AC}} = 0.7$V)

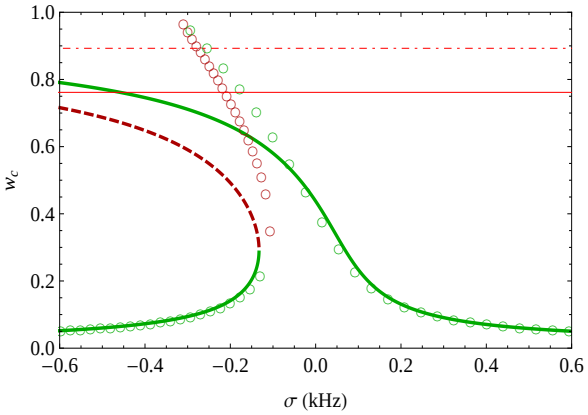

(e) Drive direction ($V_{\mathrm{AC}} = 1.2$V)

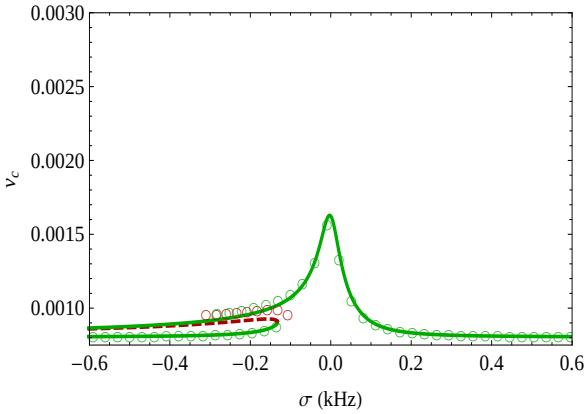

(f) Sense direction ($V_{\mathrm{AC}} = 1.2$V)

Figure 5.1: The frequency-response plots for varying V_{AC}, the solid red horizontal line indicates the physical limit of the displacement and the dashed-dot line represents the static saddle line through saddle node for the corresponding V_w ($V_w = 10.731$ V, $V_v = 3$ V, $\Omega = 18^\circ$/s). The circles indicate perturbation solution using the method of multiple scales.

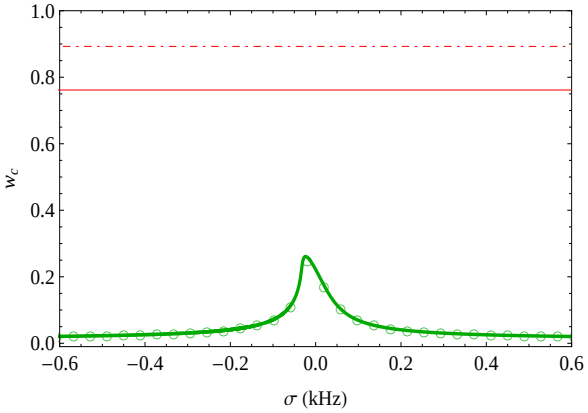

(a) Drive direction ($\Omega = 180°/s$)

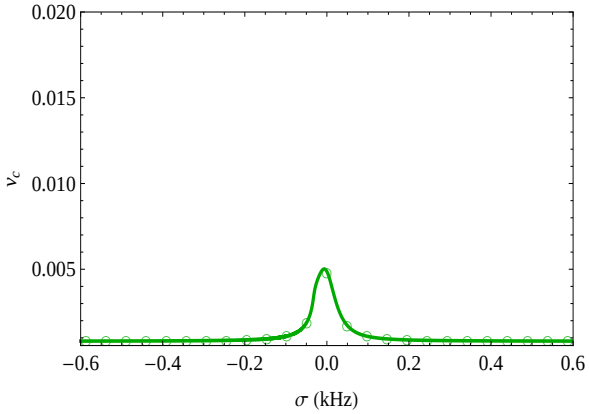

(b) Sense direction ($\Omega = 180°/s$)

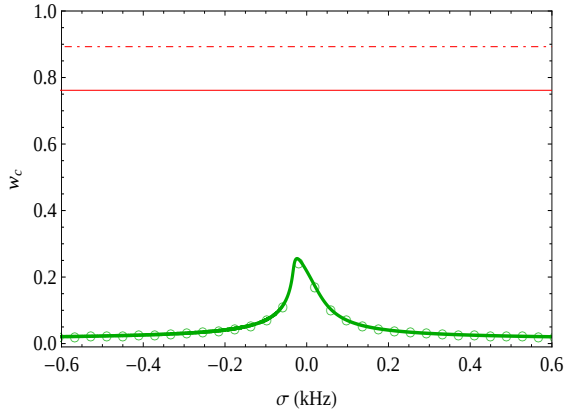

(c) Drive direction ($\Omega = 1800°/s$)

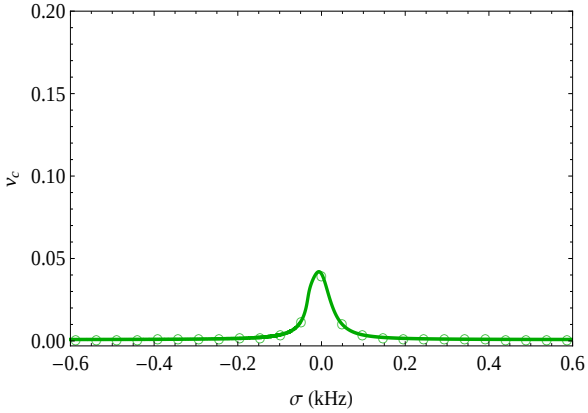

(d) Sense direction ($\Omega = 1800°/s$)

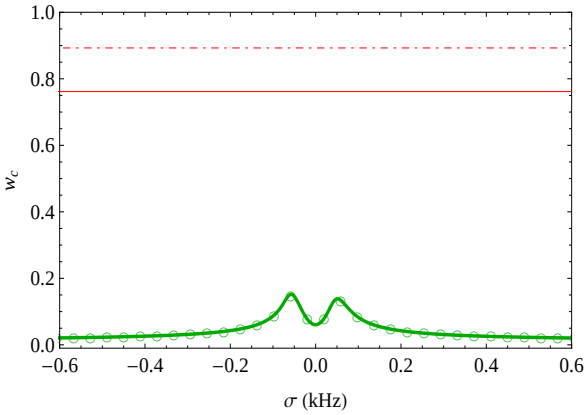

(e) Drive direction ($\Omega = 18000°/s$)

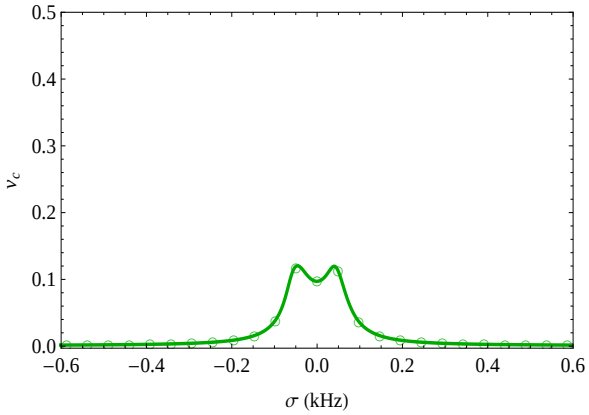

(f) Sense direction ($\Omega = 18000°/s$)

Figure 5.2: The frequency-response plots for $V_{AC} = 0.3\,V$ varying Ω, the solid red horizontal line indicates the physical limit of the displacement and the dashed-dot line represents the static saddle line through saddle node for the corresponding V_w ($V_w = 10.731\,V$, $V_v = 3\,V$). The circles indicate perturbation solution using the method of multiple scales.

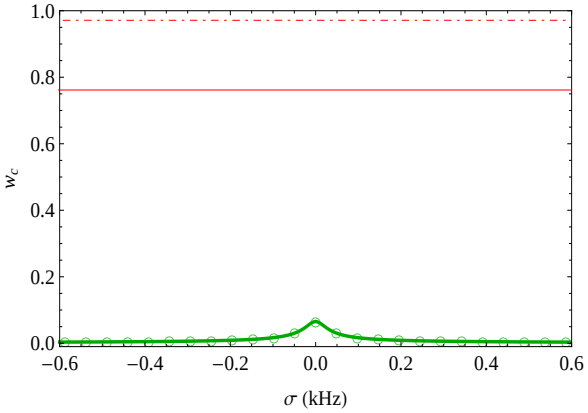

(a) Drive direction ($V_{\mathrm{AC}} = 0.3\mathrm{V}$)

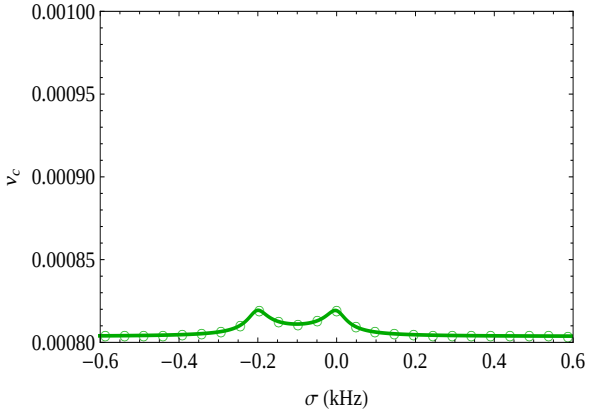

(b) Sense direction ($V_{\mathrm{AC}} = 0.3\mathrm{V}$)

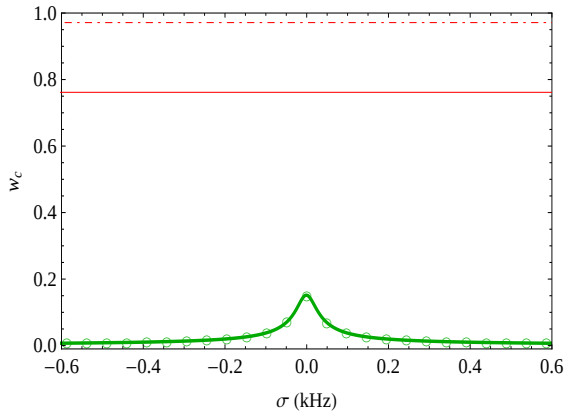

(c) Drive direction ($V_{\mathrm{AC}} = 0.7\mathrm{V}$)

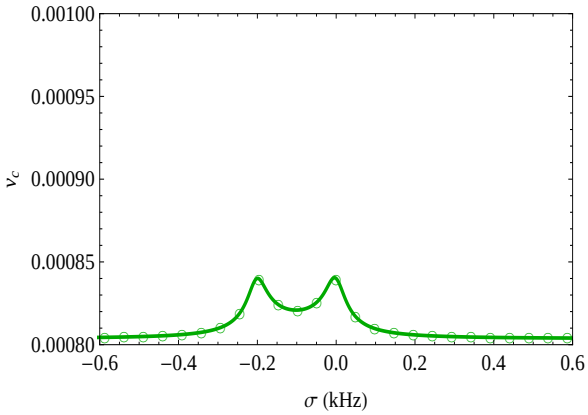

(d) Sense direction ($V_{\mathrm{AC}} = 0.7\mathrm{V}$)

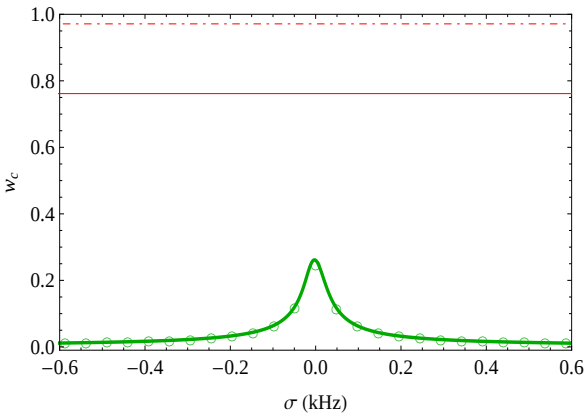

(e) Drive direction ($V_{\mathrm{AC}} = 1.2\mathrm{V}$)

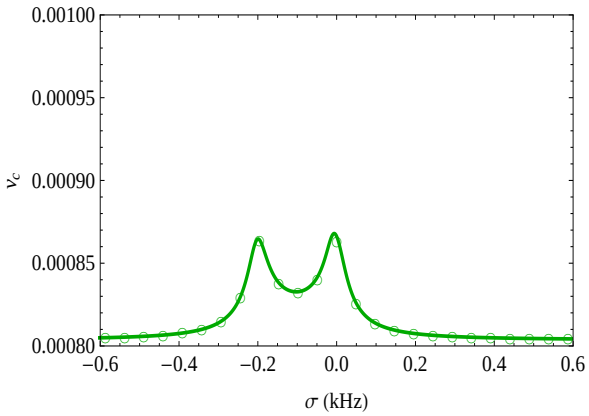

(f) Sense direction ($V_{\mathrm{AC}} = 1.2\mathrm{V}$)

Figure 5.3: The frequency-response plots for varying V_{AC}, the solid red horizontal line indicates the physical limit of the displacement and the dashed-dot line represents the static saddle line through saddle node for the corresponding V_w ($V_w = 3\,\mathrm{V}$, $V_v = 3\,\mathrm{V}$, $\Omega = 18^\circ/\mathrm{s}$). The circles indicate perturbation solution using the method of multiple scales.

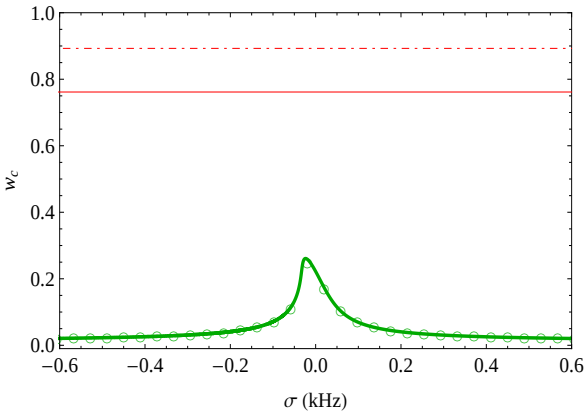

(a) Drive direction ($V_{\mathrm{AC}} = 0.3\mathrm{V}$)

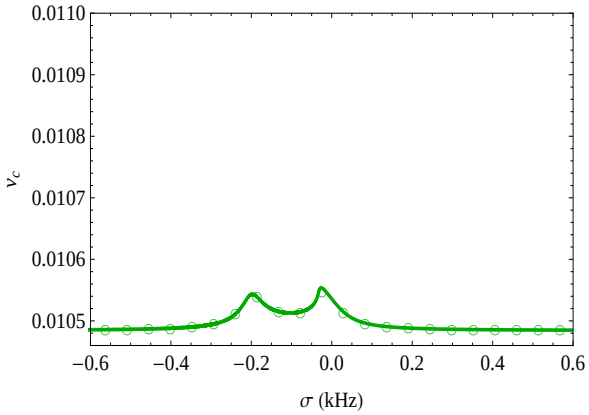

(b) Sense direction ($V_{\mathrm{AC}} = 0.3\mathrm{V}$)

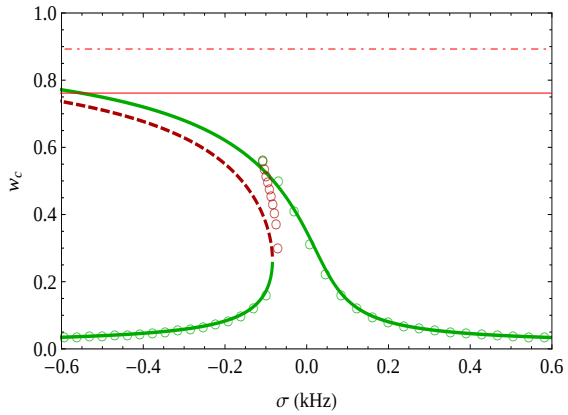

(c) Drive direction ($V_{\mathrm{AC}} = 0.7\mathrm{V}$)

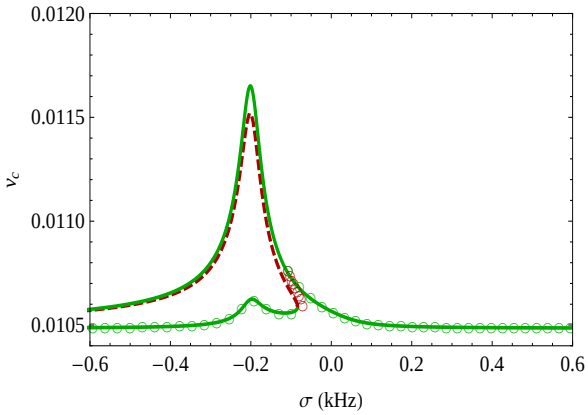

(d) Sense direction ($V_{\mathrm{AC}} = 0.7\mathrm{V}$)

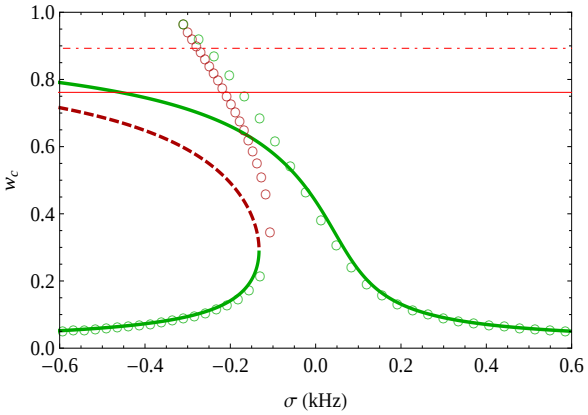

(e) Drive direction ($V_{\mathrm{AC}} = 1.2\mathrm{V}$)

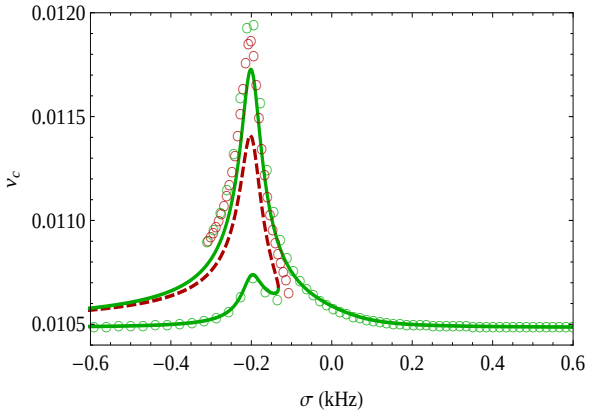

(f) Sense direction ($V_{\mathrm{AC}} = 1.2\mathrm{V}$)

Figure 5.4: The frequency-response plots for varying V_{AC}, the solid red horizontal line indicates the physical limit of the displacement and the dashed-dot line represents the static saddle line through saddle node for the corresponding V_w ($V_w = 10.731\,\mathrm{V}$, $V_v = 10.731\,\mathrm{V}$, $\Omega = 18^\circ/\mathrm{s}$). The circles indicate perturbation solution using the method of multiple scales.

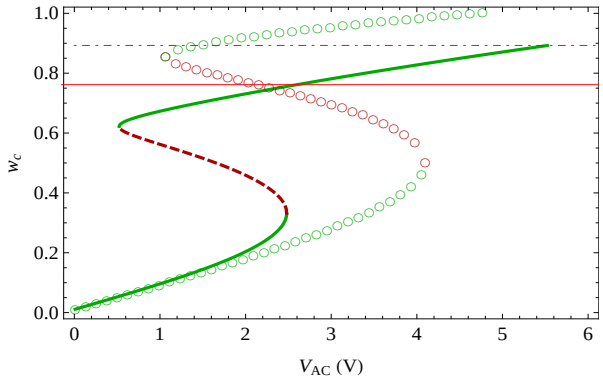

(a) Drive direction ($V_w = 10.731$ and $V_v = 3$V)

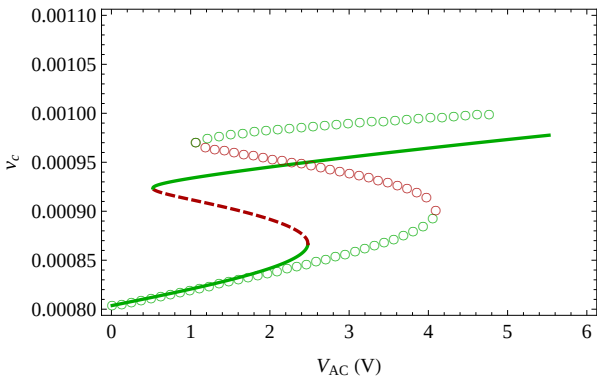

(b) Sense direction ($V_w = 10.731$ and $V_v = 3$V)

Figure 5.5: The force-response plots for $\sigma = -0.245$kHz, $V_w = 10.731$ V, $V_v = 3$ and $\Omega = 18^\circ/$s.

5.5 Orbits

In Figures 5.6(a)-5.7(f), the steady state displacement trajectories, that is the displacement in the sense direction versus the displacement in the drive direction, are plotted. The first set of figures, 5.6(a)-5.6(f), correspond to the matched natural frequencies and the second set, 5.7(a)-5.7(f), to the matched DC voltages in the drive and sense directions. Two sections at the frequency-response plots are chosen to compute the periodic orbits; first one at $\sigma = 0$ kHz and second at $\sigma = -190$ kHz near the maximum for multi-valued cases.

For the matched frequencies case, Figures 5.6(a)-5.6(f), the steady state solution indicates that near the effective natural frequency in the drive direction, that is $\sigma = 0$ kHz, the response in the sense direction is larger than when $\sigma = -190$ kHz. On the other hand, the spatial trajectory follows a nearly straight line when the excitation frequency is near the effective natural frequency in the drive direction, see Figures 5.6(a), 5.6(c), and 5.6(e). The displacement trajectory becomes an ellipse for the excitation near the effective natural frequency in the sense direction, see Figures 5.6(b), 5.6(d), and 5.6(f). A very small perturbation of initial condition on the unstable orbit, dashed line, results in converging to the small or large stable orbits, solid lines.

For the same points on the frequency-response plots of matched DC voltages at $V_w = 10.731$ V, $V_v = 10.731$ V, $\sigma = 0$ kHz and $\sigma = -190$ kHz, the steady state solutions are computed and the displacement trajectories are plotted in Figures 5.7(a)-5.7(f). In all instances, the results indicate nearly horizontal ellipses with the larger diagonal in the drive direction, as expected, for $\sigma = 0$ kHz. Approaching the effective modal frequency in the sense direction, that is $\sigma = -190$ kHz, amplifies the sense motion and therefore the ratio of the major axis to the minor axis of the ellipses becomes smaller and the angles between the major axes and the horizontal lines become larger. It is interesting to note that the smaller stable orbit for $\sigma = -190$ kHz presents a stronger response in the sense direction in comparison with the same orbit for $\sigma = 0$ kHz.

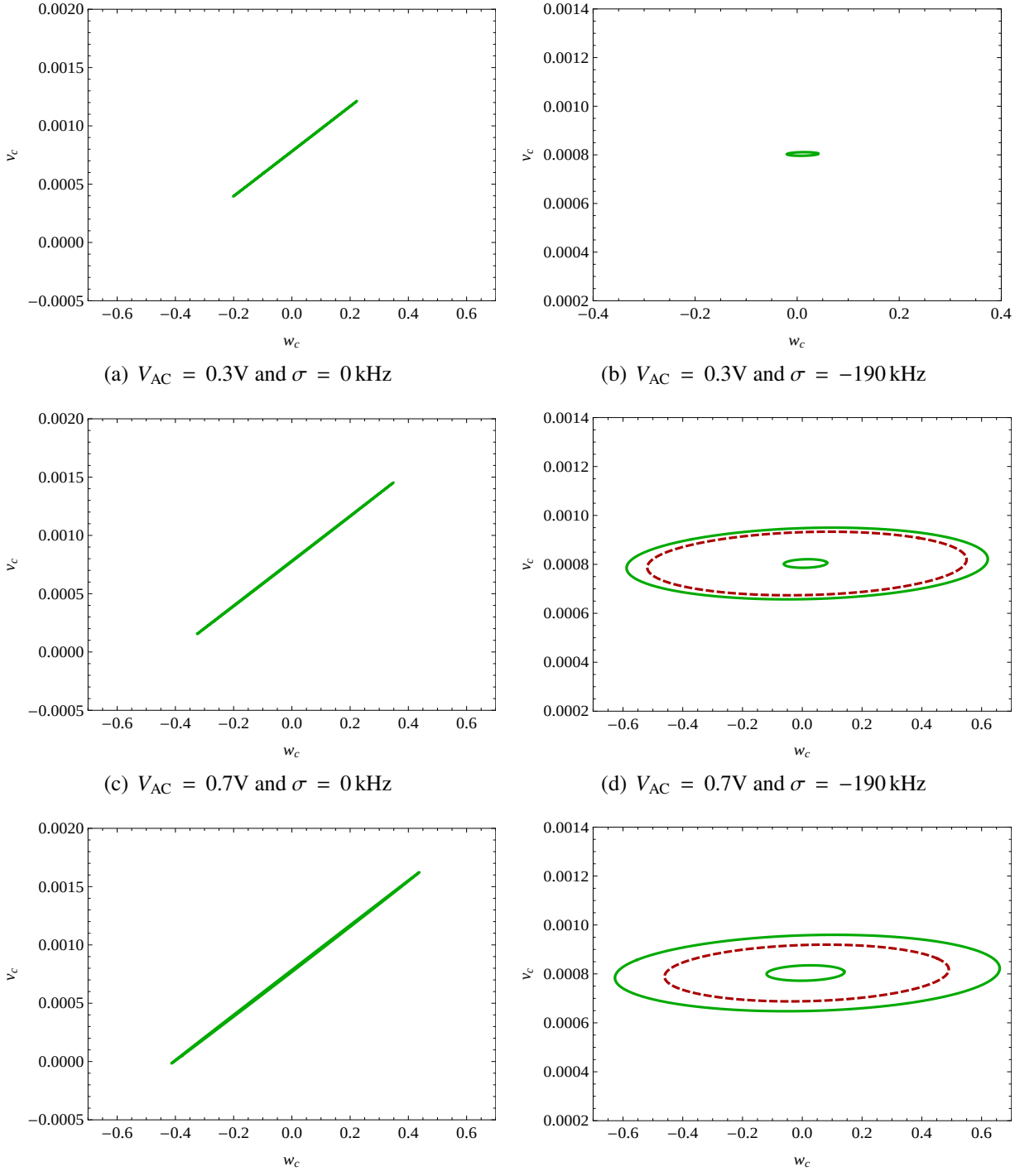

(a) $V_{\mathrm{AC}} = 0.3\mathrm{V}$ and $\sigma = 0\,\mathrm{kHz}$

(b) $V_{\mathrm{AC}} = 0.3\mathrm{V}$ and $\sigma = -190\,\mathrm{kHz}$

(c) $V_{\mathrm{AC}} = 0.7\mathrm{V}$ and $\sigma = 0\,\mathrm{kHz}$

(d) $V_{\mathrm{AC}} = 0.7\mathrm{V}$ and $\sigma = -190\,\mathrm{kHz}$

(e) $V_{\mathrm{AC}} = 1.2\mathrm{V}$ and $\sigma = 0\,\mathrm{kHz}$

(f) $V_{\mathrm{AC}} = 1.2\mathrm{V}$ and $\sigma = -190\,\mathrm{kHz}$

Figure 5.6: The orbits for two sections of frequency-response plot for $V_w = 10.731\,\mathrm{V}$, $V_v = 3\,\mathrm{V}$ and $\Omega = 18^\circ/\mathrm{s}$.

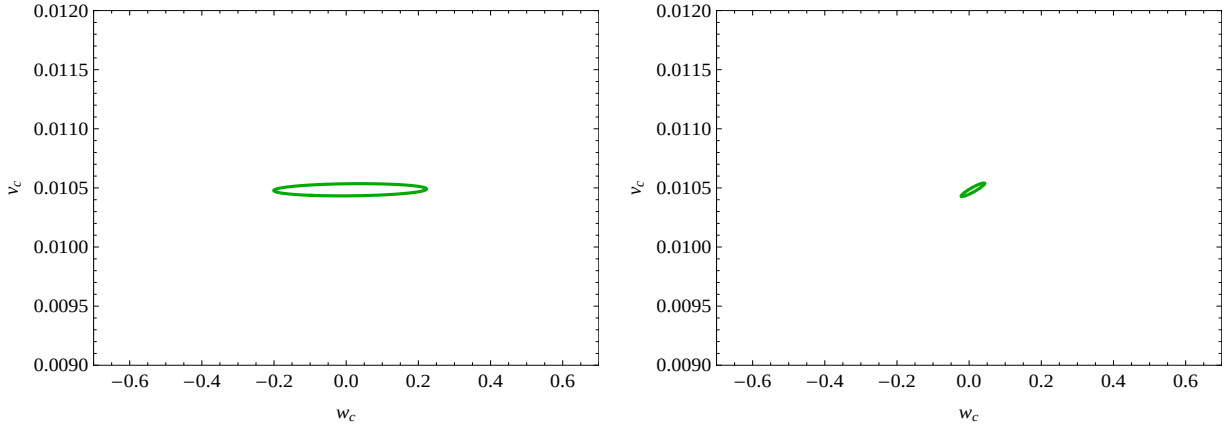

(a) $V_{\mathrm{AC}} = 0.3\mathrm{V}$ and $\sigma = 0\,\mathrm{kHz}$

(b) $V_{\mathrm{AC}} = 0.3\mathrm{V}$ and $\sigma = -190\,\mathrm{kHz}$

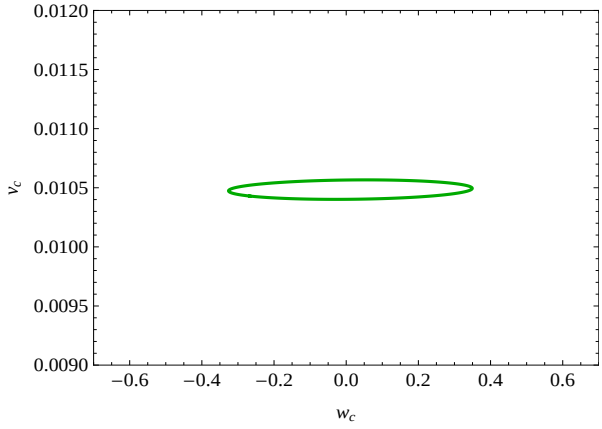

(c) $V_{\mathrm{AC}} = 0.7\mathrm{V}$ and $\sigma = 0\,\mathrm{kHz}$

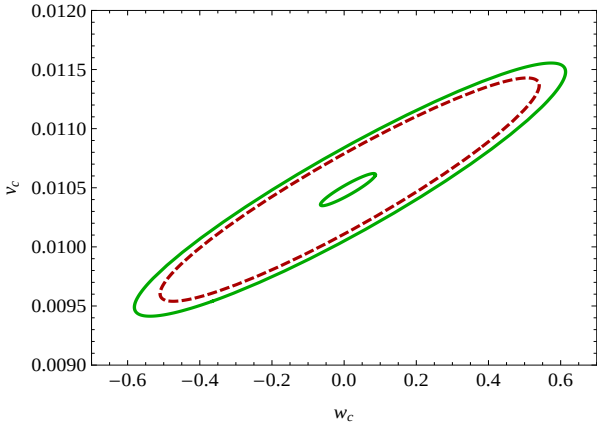

(d) $V_{\mathrm{AC}} = 0.7\mathrm{V}$ and $\sigma = -190\,\mathrm{kHz}$

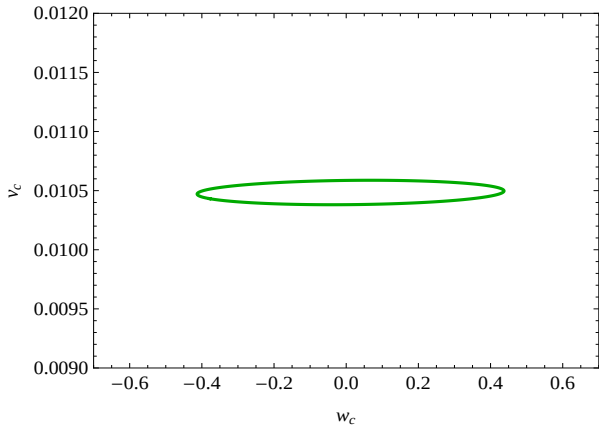

(e) $V_{\mathrm{AC}} = 1.2\mathrm{V}$ and $\sigma = 0\,\mathrm{kHz}$

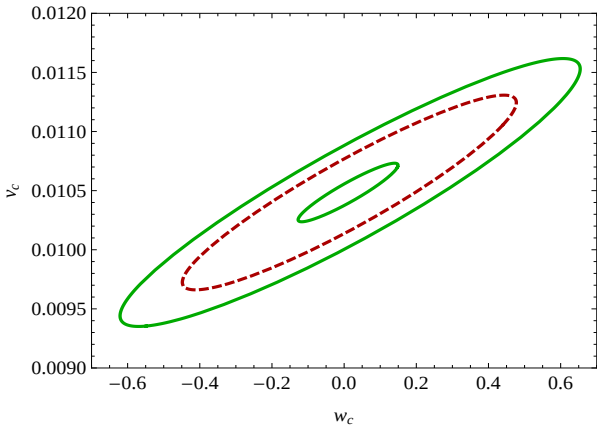

(f) $V_{\mathrm{AC}} = 1.2\mathrm{V}$ and $\sigma = -190\,\mathrm{kHz}$

Figure 5.7: The orbits for two sections of frequency-response plot for $V_w = 10.731\,\mathrm{V}$, $V_v = 10.731\,\mathrm{V}$ and $\Omega = 18^\circ/\mathrm{s}$.

5.6 Global Stability

To study the global stability of the response, the basin of attraction of the stable solution, that is the stable periodic displacement trajectory, the erosion of the basin of attraction, the jump phenomena, and the sensitivity of the steady-state solutions to the unwanted excitation are studied.

5.6.1 Basin of Attraction

Figures 5.8-5.10 present three cases: the undamped-unforced, the damped-unforced, and the damped-forced. The results are generated for the matched-frequency case in the drive direction where $V_w = 10.731\,\text{V}$, $V_v = 3\,\text{V}$ and $\Omega = 18°/\text{s}$. In Figure 5.8, the "C" indicates the stable static position (the center) and "S" the unstable static position (the saddle) which is passed over by the vertical dashed-dot line. Two modes of deflection are separated by separatrices: the initial conditions resulting in the periodic motion around the center and the initial conditions resulting in the unbounded displacement going to pull-in, that is $w_c = 1$.

The separatrix trajectories meet at the saddle node and are identified with the pair of self-intersecting trajectories (homoclinic path). Two other divergent trajectories emanate from the saddle node and go to infinity or pull-in. To compute the trajectories, the initial condition is varied and the steady-state solutions are computed by forward and backward computations. Outside the stable region, indicated by an ellipse-like shape, the trajectories do not intersect and diverge to infinity.

In Figure 5.9, the damping is included in the analysis by considering $Q_D = 400$ and $Q_S = 400$. As a result of taking damping into account, a homoclinic bifurcation occurs and the center becomes a focus "F". A heteroclinic spiral-saddle connection appears and any trajectory finally converges to the focus given the initial condition is in the filled area. Therefore, the structural change of the response is observed by adding the damping.

Figure 5.10 illustrates the damped-forced case. The AC voltage is set to 0.3V and the excitation frequency is computed for $\sigma = 500\,\text{kHz}$. The area inside the ellipse results in the bounded motion, while the outside in the divergent motion and dynamic pull-in. The right limit is slightly away from the static saddle node indicated by the vertical dashed-dot line. Comparing all three sets of results with each other, Figures 5.8-5.10, it is realized that the undamped-unforced case gives a very good approximation of the safe basin of attraction where the device can operate.

5.6.2 The Jump Phenomena, Hysteresis, and Dynamic Pull-In

The initial conditions and excitation parameters define the ultimate state of the response. To further clarify the global behaviour of the system response, the time histories and phase portraits are employed for a combination of parameters. For the matched-frequency case with $V_w = 10.731\,\text{V}$, $V_v = 3\,\text{V}, \Omega = 18°/\text{s}, Q_D = 400, Q_S = 400$, and $V_{\text{AC}} = 1.2\text{V}$ the results of long-time integration are plotted in conjunction with shooting result on Figures 5.11(a)-5.11(c). The initial condition is identified with the solid (black) circle. The final solution is the solid trajectory and matches the stable limit cycles of the shooting method indicated by small circles, see Figure 5.11(a).

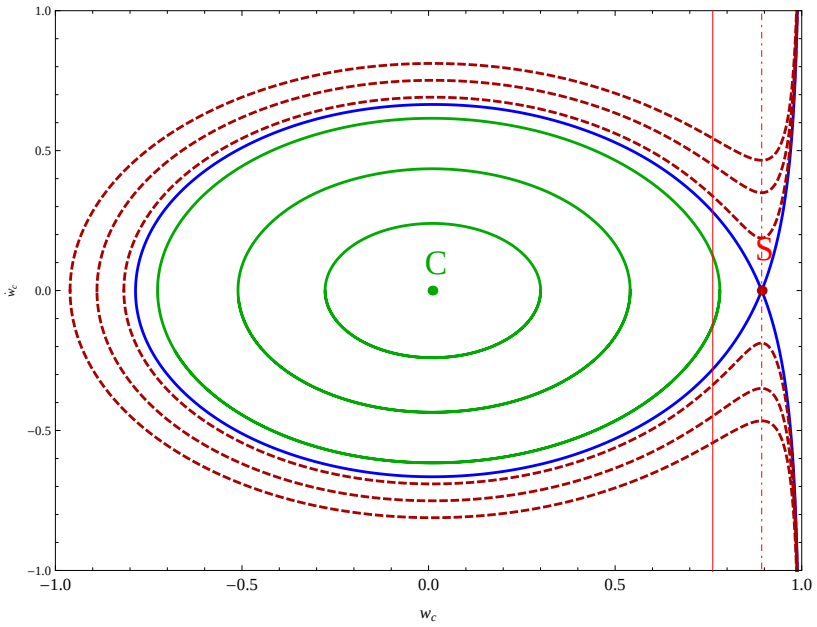

Figure 5.8: The phase portrait and the basin of attraction for the undamped-unforced case ($V_w = 10.731\,\mathrm{V}$, $V_v = 3\,\mathrm{V}$, $\Omega = 18°/\mathrm{s}$).

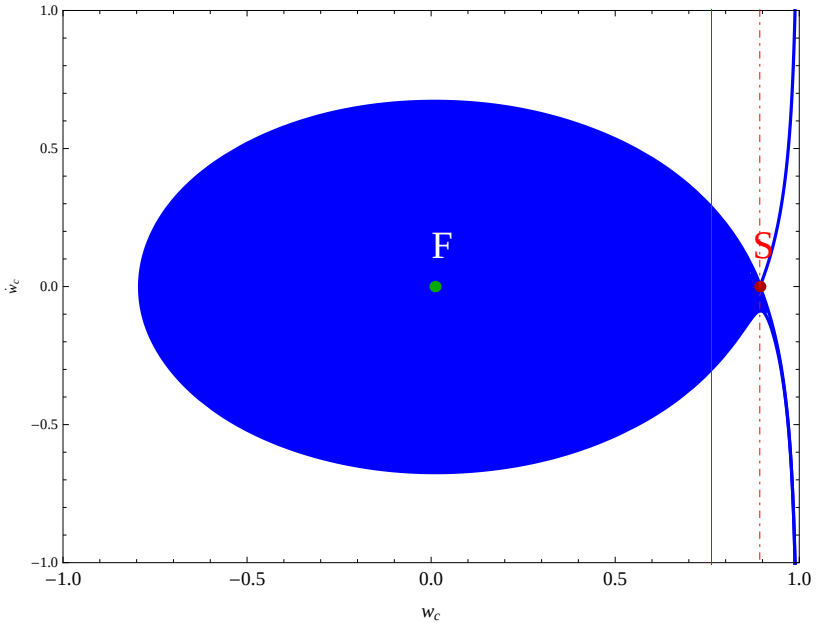

Figure 5.9: The phase portrait and the basin of attraction for the damped-unforced case ($V_w = 10.731\,\mathrm{V}$, $V_v = 3\,\mathrm{V}$, $\Omega = 18°/\mathrm{s}$, $Q = 400$).

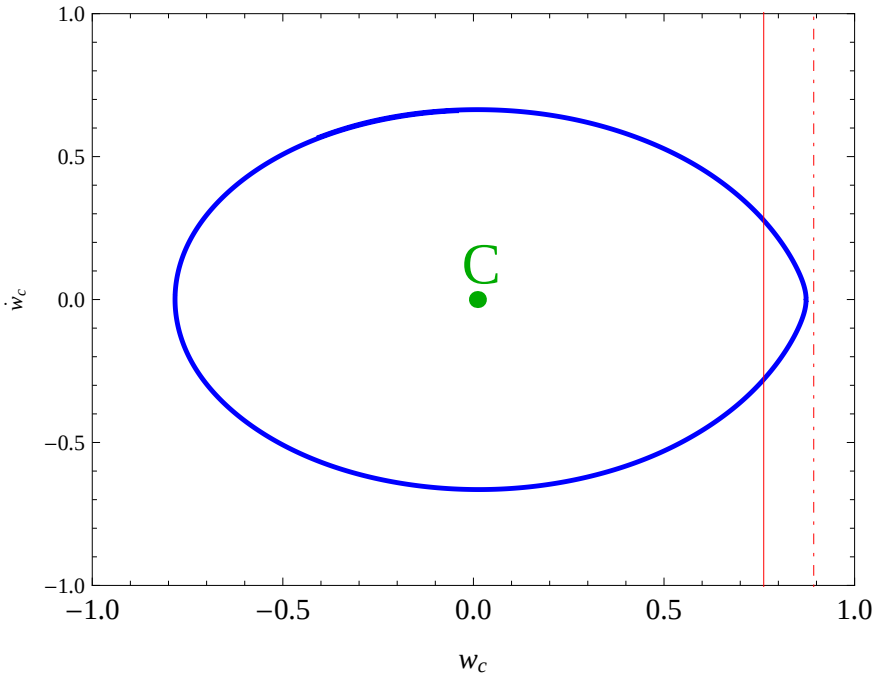

Figure 5.10: The phase portrait and the basin of attraction for the damped-forced case ($V_w = 10.731\,\text{V}$, $V_v = 3\,\text{V}$, $\Omega = 18^\circ/\text{s}$, $Q = 400$, $V_{\text{AC}} = 0.3\,\text{V}$).

The time history indicates that the solution converges to stable limit cycles after the transient motion disappears, see Figures 5.11(b) and 5.11(c). The dynamic response of the system manifests jump phenomena near the cyclic fold bifurcation point in Figures 5.1(e) and 5.1(f). The bifurcation occurs at $\sigma = -132.81\,\text{kHz}$ generating the nondimensional displacement at the center of end rigid body as large as ≈ 0.2756 and ≈ 0.0008 in the drive and sense directions, respectively. Sweeping the frequency from left to right, the response jumps to the higher stable branch where the drive and sense displacements respectively are ≈ 0.6115 and ≈ 0.0010.

Choosing an initial condition in the basin of attraction of the smaller stable orbit, the final solution merges in the smaller stable periodic solution, see Figures 5.12(a)-5.12(c). The circles indicate the results of shooting method. At the onset of bifurcation, the unstable orbit, the red circles, appear near the smaller stable orbit, the green circles. The response experiences some transient behaviour, see Figure 5.12(c), however quickly approaches and stays on the smaller stable orbit. The final state of the system depends on the initial condition and other available attractors around the initial operating point.

The initial condition of the system is influenced by external excitations such as unwanted vibrations and shock. As a result of external excitations, transients appear in the system response and the steady-state solution may settle into other than the expected orbit. In Figures 5.13(a)-5.13(c), the jump phenomena from the lower stable orbit to the larger stable orbit is demonstrated. The initial displacement condition is the same as in the previous case, Figures 5.12(a)-5.12(c), however the

initial drive velocity is increased from 0.0648 to 0.0672. The initial velocity in the sense direction is zero same as previous case.

Initially, the motion remains around the lower stable orbit. However, the result shows the response initially slowly grows and after experiencing some transient motion, the response jumps to the higher stable solution and continues to oscillate around the larger equilibrium solution. The steady state solution is completely different from the initial and the expected solution. Similar behaviour is realized considering the force-response plots, Figures 5.5(a) and 5.5(b).

In Figures 5.14(a)-5.14(c), the steady-state orbit and the time histories in the drive and sense directions are plotted for initial condition $w_c(0) = 0.0286$, $\dot{w}_c(0) = 0.4995$, $v_c(0) = 0.0009$, and $\dot{v}_c(0) = 0$. Starting near the larger stable orbit and the upper bifurcation point, the final solution converges to the same orbit. In the vicinity of upper bifurcation point, the stable and unstable solutions (identified respectively with the green and red circles) appear close to each other.

A small change in the initial condition, that is for $w_c(0) = 0.0286$, $\dot{w}_c(0) = 0.4971$, $v_c(0) = 0.0009$, and $\dot{v}_c(0) = 0$, results in the structural change of the system behaviour, see Figures 5.15(a)-5.15(c). The structure oscillates about the larger stable orbit for about 500 cycles and then is attracted to the smaller orbit after experiencing some transient motion. In backward sweep of the excitation amplitude, V_{AC}, about the upper cyclic fold bifurcation point, the response jumps to the lower branch. Increasing the excitation amplitude, V_{AC}, beyond the lower bifurcation point and decreasing the amplitude below the upper bifurcation point results in the hysteresis.

The other possibility is that by causing a change in the initial condition, the structure goes to dynamic pull-in. Near the lower bifurcation point of the force-response plot of Figure 5.5(a) for $w_c(0) = 0.2786$, $\dot{w}_c(0) = 0.0744$, $v_c(0) = 0.0008$, and $\dot{v}_c(0) = 0$, the response goes through some temporary transients and joins the stable response, Figures 5.16(a) and 5.16(b). By a small excitation in the velocity, $\dot{w}_c(0) = 0.0756$, the response rises and converges to the larger orbit after experiencing some transients, Figures 5.16(c) and 5.16(d). Further unwanted excitation, $\dot{w}_c(0) = 0.0768$, results in the failure of the device. Figures 5.16(e) and 5.16(f), demonstrate that the response in the drive direction reaches to the full gap size, $w_c = 1$ after almost 170 cycles.

5.7 Summary

The nonlinear behaviour of the rotation rate sensor has been studied in this chapter using the computational shooting method. The shooting method has been applied to the single-mode approximation of the response. The frequency-response plots have been generated for matched-frequency and matched-DC cases and compared with the results of reduced-order perturbation analysis. The global stability of the system response has been investigated by computing the orbits (periodic solutions), the basins of attraction, the jump phenomena, and the dynamic pull-in.

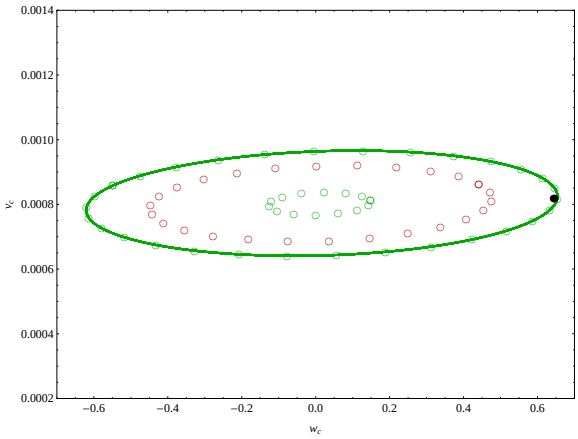

(a) Steady-state displacement trajectory

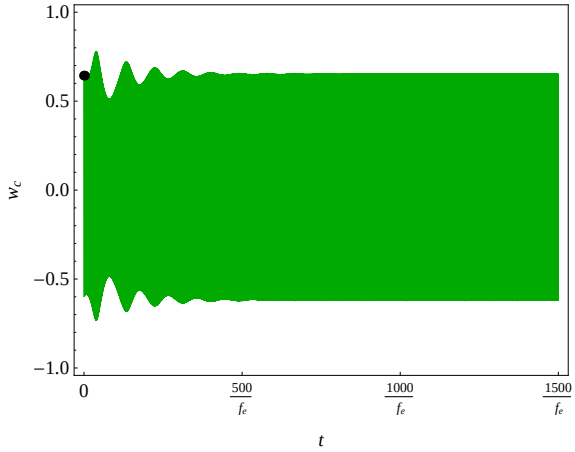

(b) Time history in the drive direction

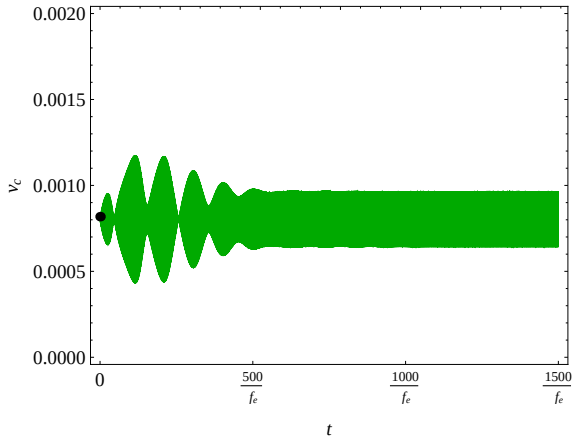

(c) Time history in the sense direction

Figure 5.11: The steady-state response and time histories for an initial condition adjacent to the larger stable orbit $V_w = 10.731\,\text{V}$, $V_v = 3\,\text{V}$, $\Omega = 18^\circ/\text{s}$, $V_{\text{AC}} = 1.2\text{V}$ and $\sigma = -190\,\text{kHz}$. The circles indicate the solution by the shooting method.

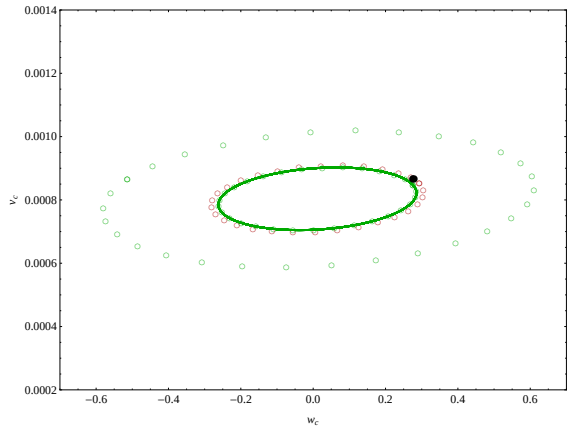

(a) Steady-state displacement trajectory

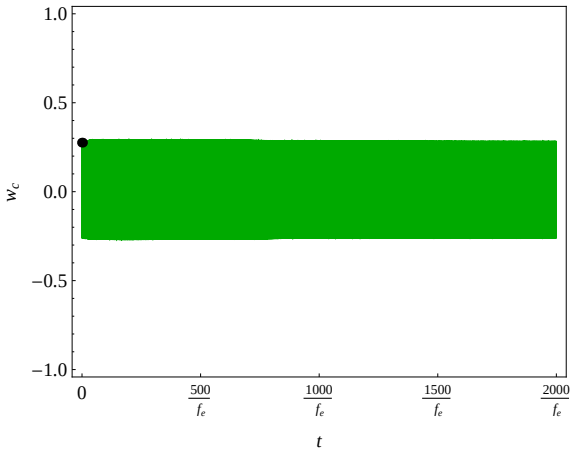

(b) Time history in the drive direction

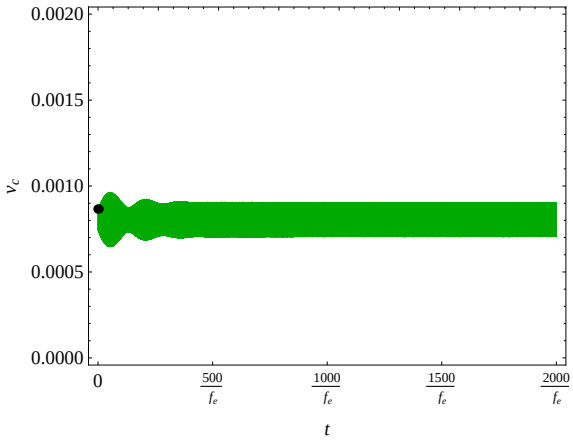

(c) Time history in the sense direction

Figure 5.12: The steady-state response and time histories for an initial condition adjacent to the smaller stable orbit $V_w = 10.731\,\text{V}$, $V_v = 3\,\text{V}$, $\Omega = 18°/\text{s}$, $V_{\text{AC}} = 1.2\text{V}$ and $\sigma = -132\,\text{kHz}$. The circles indicate the solution by the shooting method.

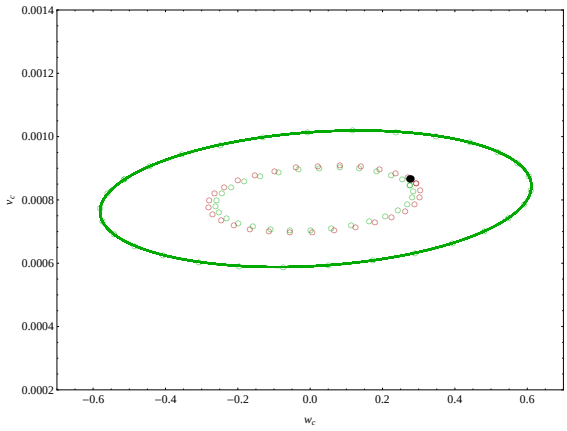

(a) Steady-state displacement trajectory

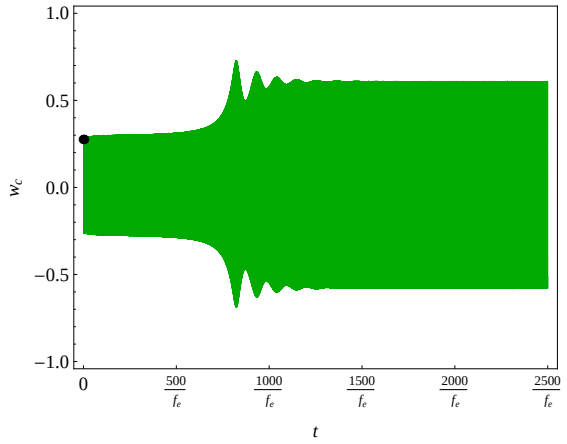

(b) Time history in the drive direction

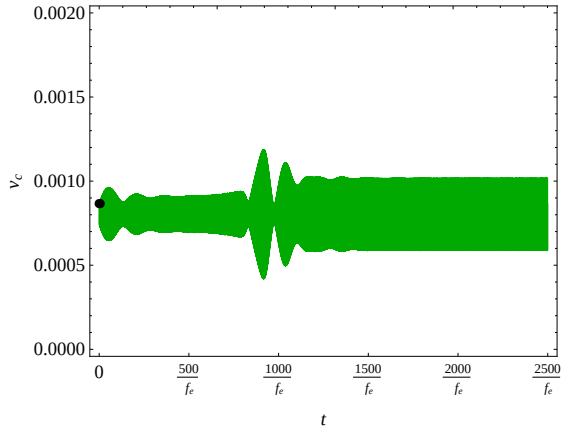

(c) Time history in the sense direction

Figure 5.13: The steady-state response and time histories for an initial condition adjacent to the smaller stable orbit $V_w = 10.731\,\text{V}$, $V_v = 3\,\text{V}$, $\Omega = 18°/\text{s}$, $V_{\text{AC}} = 1.2\text{V}$ and $\sigma = -132\,\text{kHz}$. The circles indicate the solution by the shooting method. The response jumps to the larger stable orbit near the cyclic fold bifurcation.

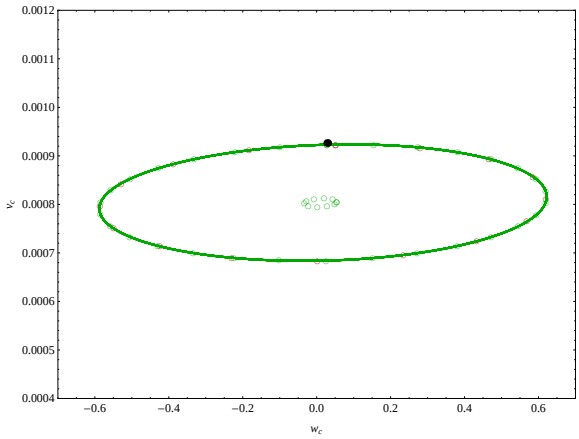

(a) Steady-state displacement trajectory

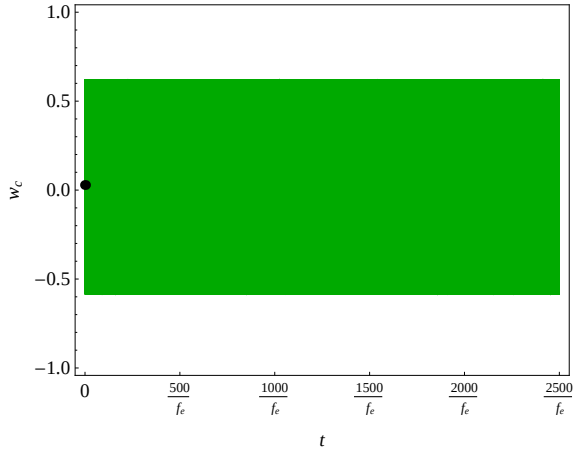

(b) Time history in the drive direction

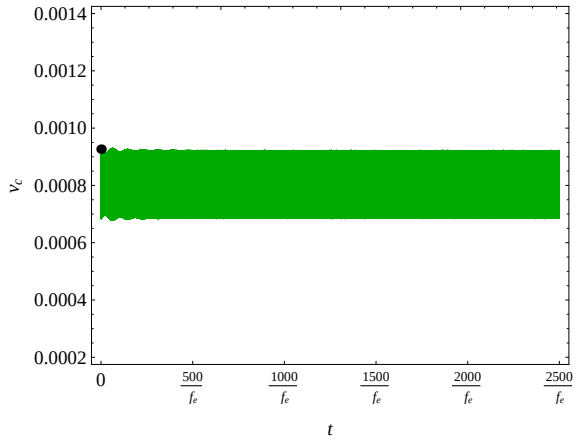

(c) Time history in the sense direction

Figure 5.14: The steady-state response and time histories for an initial condition adjacent to the larger stable orbit $V_w = 10.731\,\text{V}$, $V_v = 3\,\text{V}$, $\Omega = 18°/\text{s}$, $V_{\text{AC}} = 0.52\text{V}$ and $\sigma = -132\,\text{kHz}$. The circles indicate the solution by the shooting method.

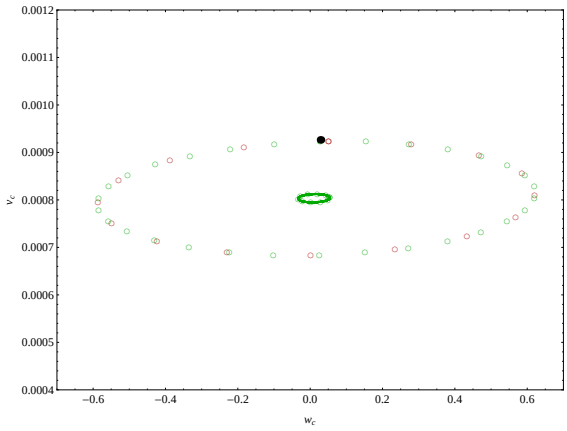

(a) Steady-state displacement trajectory

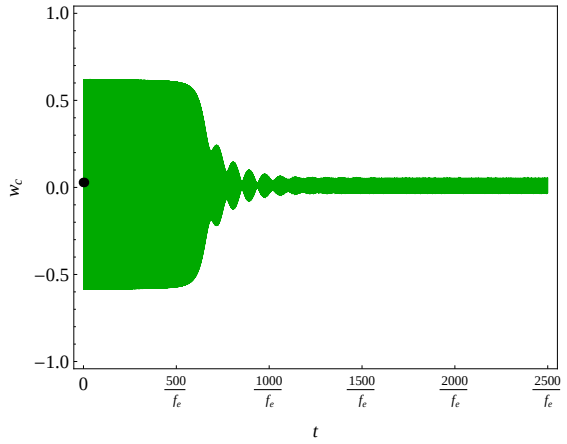

(b) Time history in the drive direction

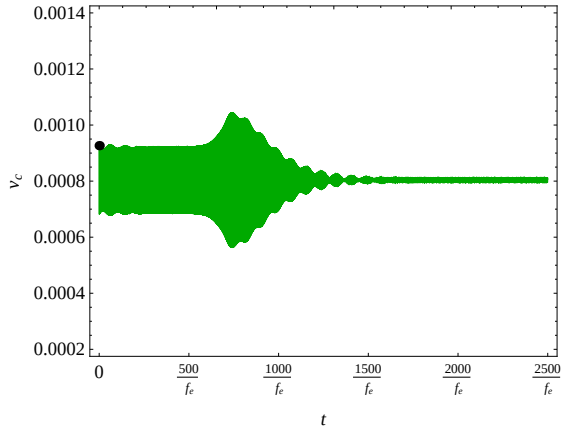

(c) Time history in the sense direction

Figure 5.15: The steady-state response and time histories for an initial condition adjacent to the smaller stable orbit $V_w = 10.731\,\text{V}$, $V_v = 3\,\text{V}$, $\Omega = 18^\circ/\text{s}$, $V_{\text{AC}} = 0.52\text{V}$ and $\sigma = -132\,\text{kHz}$. The circles indicate the solution by the shooting method. The response jumps to the smaller stable orbit near the upper cyclic fold bifurcation.

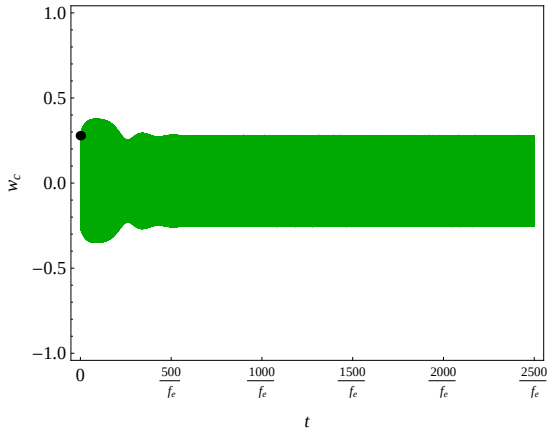

(a) Time history in the drive direction

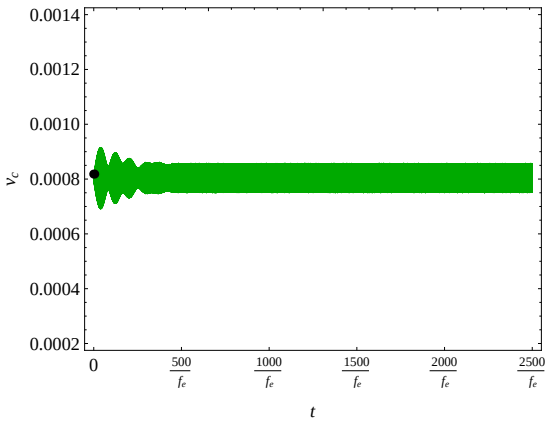

(b) Time history in the sense direction

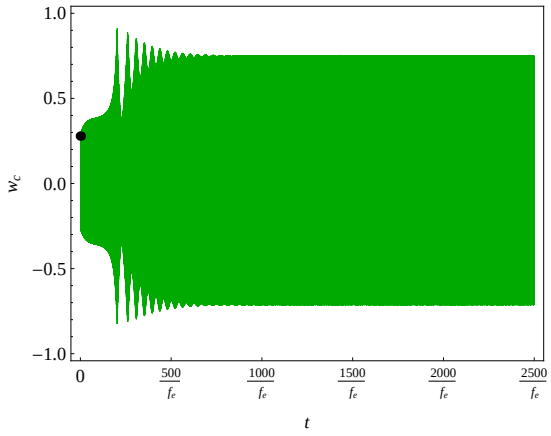

(c) Time history in the drive direction

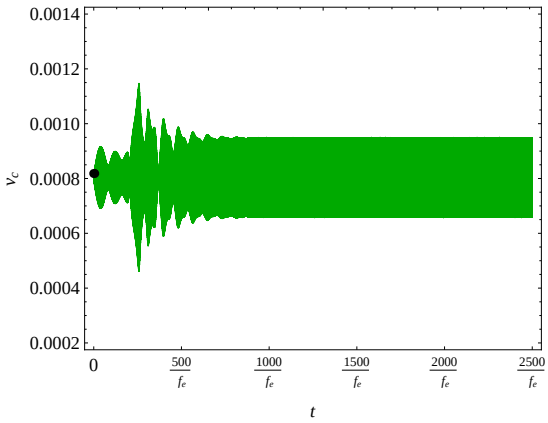

(d) Time history in the sense direction

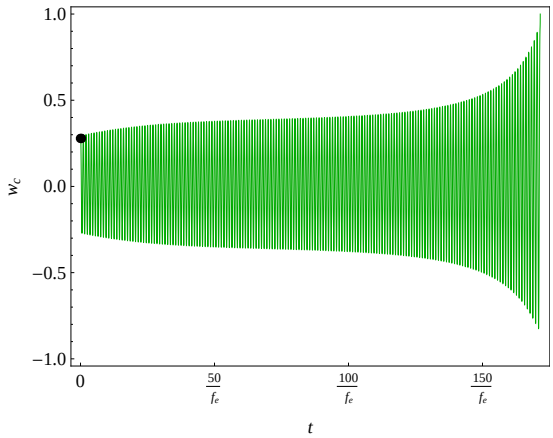

(e) Time history in the drive direction

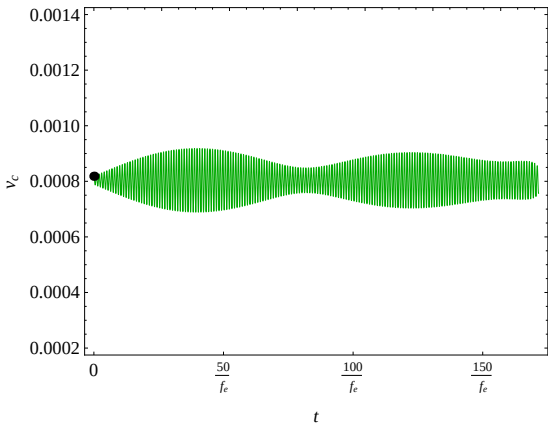

(f) Time history in the sense direction

Figure 5.16: The time histories for an initial condition adjacent to the smaller stable orbit $V_w = 10.731\,\mathrm{V}$, $V_v = 3\,\mathrm{V}$, $\Omega = 18°/\mathrm{s}$, $V_{\mathrm{AC}} = 2.4\mathrm{V}$ and $\sigma = -132\,\mathrm{kHz}$. The circles indicate the solution by the shooting method. The response jumps to the smaller stable orbit near the upper cyclic fold bifurcation.

Chapter 6

Mechanical-Thermal Noise Analysis

6.1 Preview

Mechanical-thermal (thermomechanical) noise defines the theoretical sensitivity limit of any mechanical oscillator and becomes of prime importance at the micro/nano-scale, see Section 1.4 for an introduction on mechanical-thermal noise (MTN). The thermal noise appears in conjunction with the damping term. In the following sections the thermomechcanical noise for the beam-rigid body rotation rate sensor is characterized. Two approaches are employed: the linearized equation of motion, equations (3.48) and (3.49) including damping terms, and the slowly varying system, equations (4.46)-(4.49). The method is developed in this chapter for the further analysis of the performance of the novel sensor in the future.

6.2 The Linear Analysis of MTN

The objective is to characterize the effect of MTN on the displacement in the sense direction. The displacement in the drive axis is sufficiently large that the MTN effect is negligible in this direction and discarded. The virtual work done by the thermal noise is computed at the center of end rigid body as

$$\overline{\delta W_n} = F_n \delta v_c \tag{6.1}$$

where F_n represents the generalized noise force and v_c the displacement at the center of mass. Including the thermal noise work, discretizing displacements using (2.74), and computing Lagrange's equations, equations (1.2), gives a similar equation as in (2.76) with an additional generalized (modal) noise force term. The equations are linearized around the static position following the procedure outlined in Chapter 3 equations (3.43)-(3.49). The mechanical-thermal noise is associated with the damping and appears in the dynamic equation. The system of equations are

expressed as

$$\ddot{q}_d(t) + D_q\dot{q}_d(t) + K_q q_d(t) = -F_q\cos\left(t\Omega_e\right) \tag{6.2}$$

$$\ddot{p}_d(t) + \Omega C_p\dot{q}_d(t) + D_p\dot{p}_d(t) + K_p p_d(t) = \hat{F}_n\left(e\phi'(1) + \phi(1)\right) \tag{6.3}$$

where

$$K_q = \frac{\Delta\Gamma''\left(q_s\left(e\psi'(1) + \psi(1)\right) - 1\right)^3 + 2e\nu V_w^2\left(e\psi'(1) + \psi(1)\right)^2}{\Delta\left(q_s\left(e\psi'(1) + \psi(1)\right) - 1\right)^3\left(\alpha\Gamma' + \Gamma + M\left(e\psi'(1) + \psi(1)\right)^2 + J_{22}\psi'(1)^2\right)} \tag{6.4}$$

$$D_q = \frac{c_q}{\Delta\left(\alpha\Gamma' + \Gamma + M\left(e\psi'(1) + \psi(1)\right)^2 + J_{22}\psi'(1)^2\right)} \tag{6.5}$$

$$F_q = -\frac{2e\nu V_{\mathrm{AC}} V_w\left(e\psi'(1) + \psi(1)\right)}{\Delta\left(q_s\left(e\psi'(1) + \psi(1)\right) - 1\right)^2\left(\alpha\Gamma' + \Gamma + M\left(e\psi'(1) + \psi(1)\right)^2 + J_{22}\psi'(1)^2\right)} \tag{6.6}$$

$$K_p = \frac{\Delta^3\Lambda''\left(p_s\left(e\phi'(1) + \phi(1)\right) - 1\right)^3 + 2e\nu V_v^2\left(e\phi'(1) + \phi(1)\right)^2}{\Delta\left(p_s\left(e\phi'(1) + \phi(1)\right) - 1\right)^3\left(\alpha\Delta^2\Lambda' + M\left(e\phi'(1) + \phi(1)\right)^2 + J_{33}\phi'(1)^2 + \Lambda\right)} \tag{6.7}$$

$$D_p = \frac{c_p}{\Delta\left(\alpha\Delta^2\Lambda' + M\left(e\phi'(1) + \phi(1)\right)^2 + J_{33}\phi'(1)^2 + \Lambda\right)} \tag{6.8}$$

$$\hat{F}_n = \frac{F_n}{6eL_B g_v\alpha^2} \tag{6.9}$$

In equation (6.2), the effect of the Coriolis force on the drive direction is neglected which is acceptable by virtue of its small magnitude compared with the driving force. This compact form of the governing equations is suitable for the design purpose. Other coefficients were introduced in equation (2.65) and (2.66). Inserting a solution of the form

$$q_d(t) = a_q\cos\left(\Omega_e\, t - \theta\right) \tag{6.10}$$

into equation (6.2), separating the coefficients of $\cos\left(\Omega_e\, t\right)$ and $\sin\left(\Omega_e\, t\right)$, and equating the coefficients to zero gives the following relations for the phase and amplitude

$$\theta = -\arctan\left(\frac{D_q\Omega_e}{\Omega_e^2 - K_q}\right) \tag{6.11}$$

$$a_q = \frac{F_q}{\sqrt{D_q^2\Omega_e^2 + \left(\Omega_e^2 - K_q\right)^2}} \tag{6.12}$$

or

$$a_q = \frac{-2e\nu V_{\mathrm{AC}} V_w \left(e\psi'(1) + \psi(1)\right)}{\Delta \sqrt{D_q^2 \Omega_e^2 + \left(\Omega_e^2 - K_q\right)^2} \left(q_s \left(e\psi'(1) + \psi(1)\right) - 1\right)^2 \left(\alpha\Gamma' + \Gamma + M \left(e\psi'(1) + \psi(1)\right)^2 + J_{22}\psi'(1)^2\right)} \tag{6.13}$$

Equation (6.13) provides the necessary tool to measure the maximum amplitude for most of practical purposes where the response is limited to the linear range. According to the equation of sense mode, (6.3), the Coriolis force is given by

$$F_c \;=\; -\Omega C_p \dot{q}_d(t) \tag{6.14}$$

The maximum displacement rate in the drive direction, $\dot{q}_d(t)$ is $\Omega_e\, a_q$. The amplitude is given in equation (6.13). The MTN equivalent rotation rate, Ω_n, is determined by equating the thermal noise force and the Coriolis force, thus

$$C_p\, \Omega_n\, \Omega_e\, a_q \;=\; \hat{F}_n \left(e\phi'(1) + \phi(1)\right) \tag{6.15}$$

Solving equation (6.15) for Ω_n gives

$$\Omega_n = -\frac{\hat{F}_n \left(e\phi'(1) + \phi(1)\right) \left(\alpha\Delta^2\Lambda' + M \left(e\phi'(1) + \phi(1)\right)^2 + J_{33}\phi'(1)^2 + \Lambda\right)}{a_q \Omega_e \left(2M \left(e\psi'(1) + \psi(1)\right) \left(e\phi'(1) + \phi(1)\right) + \left(-J_{11} + J_{22} + J_{33}\right) \psi'(1)\phi'(1) + 2\Pi\right)} \tag{6.16}$$

Inserting equation (6.13) into equation (6.16) gives the closed-form relation for computing the noise-equivalent angular rotation rate, Ω_n, for a beam-rigid body gyroscope (rotation rate sensor). Operating the gyroscope near the effective natural frequency increases the sensitivity of the device, that is the sense amplitude increases. Therefore, for Ω_e^2 near K_q^2, the oscillation amplitude, equation (6.12), a_q becomes

$$a_q \;=\; \frac{F_q}{D_q\, \Omega_e} \tag{6.17}$$

The MTN equivalent rotation rate for beam-rigid body sensor is thus given by

$$\Omega_n = -\frac{\Gamma\omega_D \hat{F}_n \left(e\phi'(1) + \phi(1)\right) \left(q_s \left(e\psi'(1) + \psi(1)\right) - 1\right)^2 \mathcal{A}}{2e\nu V_{\mathrm{AC}} Q_D V_w \left(e\psi'(1) + \psi(1)\right)\, \mathcal{B}} \tag{6.18}$$

where

$$\mathcal{A} \;=\; \left(\alpha\Gamma' + \Gamma + \hat{M} \left(\hat{e}\psi'(1) + \psi(1)\right)^2 + \hat{J}_{22}\psi'(1)^2\right) \left(\alpha\Lambda' + \hat{M} \left(\hat{e}\phi'(1) + \phi(1)\right)^2 + \hat{J}_{33}\phi'(1)^2 + \Lambda\right)$$

$$\mathcal{B} = \left(2\hat{M}\left(\hat{e}\psi'(1)+\psi(1)\right)\left(\hat{e}\phi'(1)+\phi(1)\right)+\left(-\hat{J}_{11}+\hat{J}_{22}+\hat{J}_{33}\right)\psi'(1)\phi'(1)+2\Pi\right)$$

where the damping has been replaced with $m_q\,\omega_D/Q_D$ with m_q being the coefficient of the modal acceleration terms, that is $\ddot{q}(t)$ in equation (5.1). Equation (6.18) is of prime importance in the design procedure of beam-based rotation rate sensors. It is noted that the MTNΩ is inversely related to the quality factor in the drive direction, Q_D and the AC voltage $V_{\rm AC}$. The static deflection q_s is associated with the DC load V_w.

6.3 The Nonlinear Analysis of MTN

The method of reduced-order nonlinear analysis was presented in Chapter 4. The slow system is given in equations (4.46) to (4.49) in Cartesian coordinate system. The MTN force appears in the same order as damping and the excitation. The method of multiple scales is based on the identification and removal of secular terms. The micro/nano-systems present very light damping and thus act as narrow-band filter. The excitation frequency is matched with the effective natural frequencies in the drive and sense directions. It is assumed that the noise force appears at the frequency of oscillation (which is equal to the effective natural frequencies). Therefore, the modified form of the third-order problem, equation (4.15), in the sense direction is given by

$$\begin{aligned}\partial_0^2 p_{d3}+p_{d3}\,\omega_p^2 = {} & T_n\,\cos(\Omega_e\,t)-P_{13}p_{d1}^3-P_2\partial_0^2 p_{d1}\,p_{d1}^2-2P_{12}p_{d2}\,p_{d1}-6p_sP_{13}p_{d2}\,p_{d1}\\ & -2P_1\partial_1\partial_0 p_{d1}\,p_{d1}-4p_sP_2\partial_1\partial_0 p_{d1}\,p_{d1}-P_1\partial_0^2 p_{d2}\,p_{d1}\\ & -2p_sP_2\partial_0^2 p_{d2}\,p_{d1}-\partial_1^2 p_{d1}-P_3\partial_0 p_{d1}-p_sP_4\partial_0 p_{d1}-p_s^2P_5\partial_0 p_{d1}\\ & -\Omega P_6\partial_0 q_{d1}-\Omega p_sP_7\partial_0 q_{d1}-\Omega p_s^2P_8\partial_0 q_{d1}\\ & -2\partial_2\partial_0 p_{d1}-2\partial_1\partial_0 p_{d2}-P_1p_{d2}\,\partial_0^2 p_{d1}-2p_sP_2p_{d2}\,\partial_0^2 p_{d1}\end{aligned}\tag{6.19}$$

where $T_n = \hat{F}_n\,(\phi(1)+e\,\phi'(1))$ indicates the noise force. Following the same procedure as outlined in chapter 4, the third-order problem develops to

$$\begin{aligned}\partial_0^2 p_{d3}+\omega_q^2\,p_{d3} = {} & \Bigg(\frac{1}{2}T_n\,e^{i\sigma t_2}-i\left(P_8p_s^2+P_7p_s+P_6\right)\Omega\omega_qA_q+e^{i\,\delta\,t_2}\Big((5H_1P_1+2H_2P_1\\ & +(10H_1p_s+4H_2p_s+3)\,P_2\Big)\omega_q^2\bar{A}_p\,A_p^2-(2H_1P_{12}\\ & +4H_2P_{12}+(6H_1p_s+12H_2p_s+3)\,P_{13}\Big)\bar{A}_p\,A_p^2\\ & -i\omega_q\left(\left(P_5p_s^2+P_4p_s+P_3\right)A_p+2\dot{A}_p\right)\Bigg)\Bigg)e^{it_0\omega_q}+C.C.\end{aligned}\tag{6.20}$$

The modulation equations in the polar coordinates becomes

$$\left(\frac{1}{4}\left(G_1+2G_2\right)\left(3Q_{13}q_s+Q_{12}\right)+\frac{3}{8}Q_{13}-\frac{1}{8}\omega_q^2\left(\left(5G_1+2G_2\right)\left(2Q_2q_s+Q_1\right)+3Q_2\right)\right)a_q^3$$

$$-\frac{1}{2}\Omega\omega_q a_p\left(q_s\left(Q_8 q_s+Q_7\right)+Q_6\right)\sin\left(\eta_2\right)+\omega_q a_q\left(\dot{\eta}_1-\sigma\right)=Q_{14}V_{\mathrm{AC}}V_w\cos\left(\eta_1\right) \tag{6.21}$$

$$\begin{aligned}&\left(\frac{1}{4}\left(H_1+2H_2\right)+\frac{3}{8}P_{13}\cos\left(\eta_2\right)-\frac{1}{8}\omega_q^2\cos\left(\eta_2\right)\left(\left(5H_1+2H_2\right)\left(2P_2p_s+P_1\right)+3P_2\right)\right)a_p^3\\&+\omega_q\left(\left(\delta-\sigma+\dot{\eta}_1-\dot{\eta}_2\right)\cos\left(\eta_2\right)a_p-\sin\left(\eta_2\right)\dot{a}_p-\frac{1}{2}a_p\left(p_s\left(P_5p_s+P_4\right)+P_3\right)\sin\left(\eta_2\right)\right)\\&+\left(3P_{13}p_s+P_{12}\right)\cos\left(\eta_2\right)=\frac{1}{2}T_n\cos\left(\eta_1\right)\end{aligned} \tag{6.22}$$

$$\begin{aligned}&\frac{1}{2}\Omega\omega_q a_p\left(q_s\left(Q_8q_s+Q_7\right)+Q_6\right)\cos\left(\eta_2\right)+\omega_q\left(\frac{1}{2}a_q\left(q_s\left(Q_5q_s+Q_4\right)+Q_3\right)+\dot{a}_q\right)\\&=Q_{14}V_{\mathrm{AC}}V_{\mathrm{w}}\sin\left(\eta_1\right)\end{aligned} \tag{6.23}$$

$$\begin{aligned}&\left(\frac{1}{4}\left(H_1+2H_2\right)+\frac{3}{8}P_{13}\sin\left(\eta_2\right)-\frac{1}{8}\omega_q^2\sin\left(\eta_2\right)\left(\left(5H_1+2H_2\right)\left(2P_2p_s+P_1\right)+3P_2\right)\right)a_p^3\\&+\left(\frac{1}{2}\left(p_s\left(P_5p_s+P_4\right)+P_3\right)\cos\left(\eta_2\right)a_p+\left(\delta-\sigma+\dot{\eta}_1-\dot{\eta}_2\right)\sin\left(\eta_2\right)a_p+\cos\left(\eta_2\right)\dot{a}_p\right)\omega_q\\&+\left(3P_{13}p_s+P_{12}\right)\sin\left(\eta_2\right)+\frac{1}{2}\Omega\,\omega_q a_q\left(p_s\left(P_8p_s+P_7\right)+P_6\right)=\frac{1}{2}T_n\sin\left(\eta_1\right)\end{aligned} \tag{6.24}$$

where the phases are given in equations (4.37) and (4.38). And in Cartesian coordinates, the first three modulation equations remain the same as equations (4.46)-(4.48), but the last equation takes the form

$$\dot{y}_p{=}f_4 \tag{6.25}$$

where

$$\begin{aligned}f_4{=}&\frac{1}{2\,\omega_q}T_n+\frac{1}{2}y_p\left(-p_s\left(P_5p_s+P_4\right)-P_3\right)-\frac{1}{2}\Omega y_q\left(p_s\left(P_8p_s+P_7\right)+P_6\right)+\left(\sigma-\delta\right)x_p\\&+x_p\left(\frac{y_p^2\left(\omega_q^2\left(\left(5H_1+2H_2\right)\left(2P_2p_s+P_1\right)+3P_2\right)-2\left(H_1+2H_2\right)\left(3P_{13}p_s+P_{12}\right)-3P_{13}\right)}{8\omega_q}\right)\\&+\frac{x_p^3\left(\omega_q^2\left(\left(5H_1+2H_2\right)\left(2P_2p_s+P_1\right)+3P_2\right)-2\left(H_1+2H_2\right)\left(3P_{13}p_s+P_{12}\right)-3P_{13}\right)}{8\omega_q}\end{aligned} \tag{6.26}$$

For practical purposes, it is desired to avoid a multi-valued response and the consequent instabil-

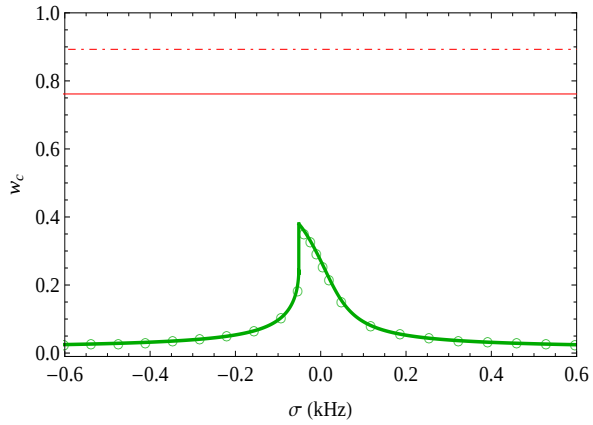

(a) Drive: $Q_D = 400$, $Q_S = 400$, $V_{\text{AC}} = 0.43\text{V}$

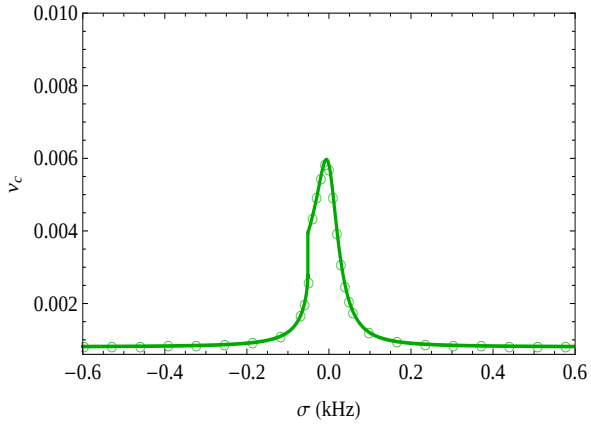

(b) Sense: $Q_D = 400$, $Q_S = 400$, $V_{\text{AC}} = 0.43\text{V}$

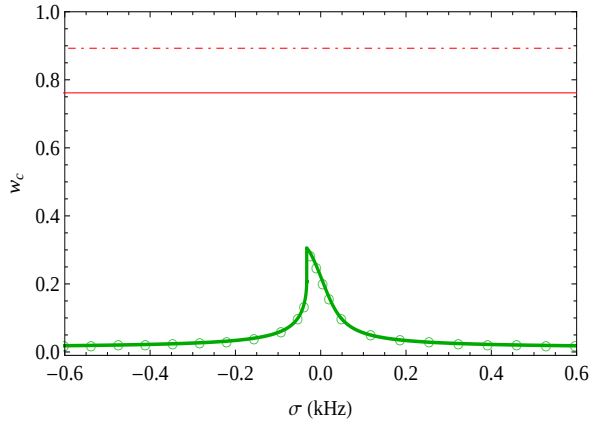

(c) Drive: $Q_D = 600$, $Q_S = 600$, $V_{\text{AC}} = 0.23\text{V}$

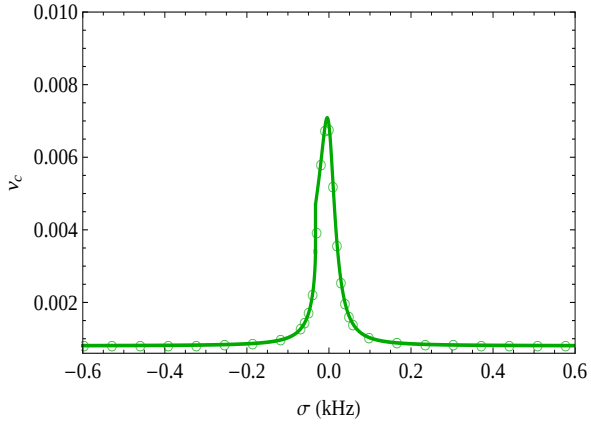

(d) Sense: $Q_D = 600$, $Q_S = 600$, $V_{\text{AC}} = 0.23\text{V}$

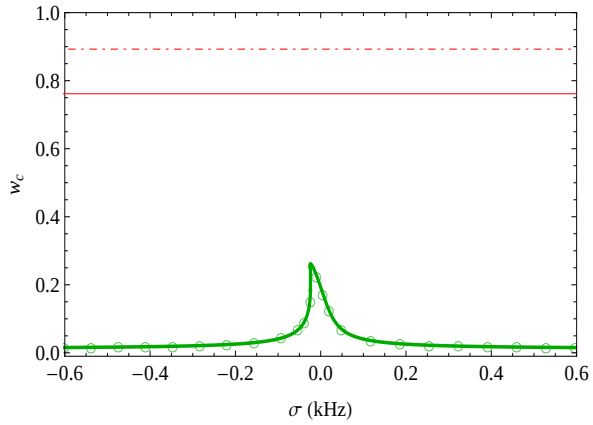

(e) Drive: $Q_D = 800$, $Q_S = 800$, $V_{\text{AC}} = 0.15\text{V}$

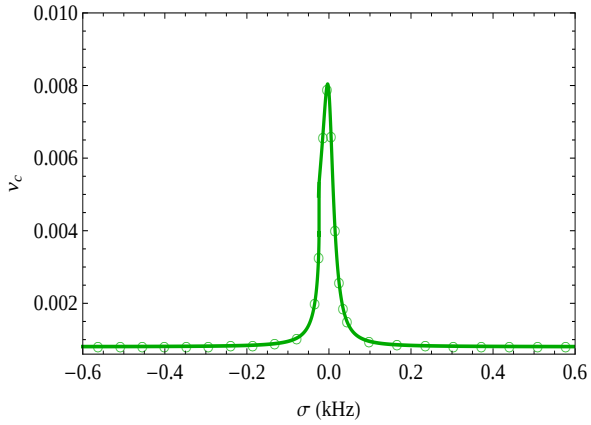

(f) Sense: $Q_D = 800$, $Q_S = 800$, $V_{\text{AC}} = 0.15\text{V}$

Figure 6.1: The frequency-response plots for $V_w = 10.731\,\text{V}$, $V_v = 3\,\text{V}$, and $\Omega = 180°/\text{s}$, The circles indicate the solution by the perturbation method and the solid line the results of the shooting method.

ity. Therefore, the AC voltage is limited to the range resulting in a single-valued response. The reduced-order nonlinear analysis using the perturbation method presented in Chapter 4 agrees remarkably well with the computational shooting method, while the later is computationally more demanding and time consuming. In the frequency-response plots of Figures 6.1(a)-6.1(f), the results of method of multiple scales are compared with the shooting method for varying quality factors and AC voltages. The noise force, T_n, is set to zero. Above the identified AC load, an unstable branch appears in the response.

6.4 Noise Equivalent Rotation Rate

To compute the noise equivalent (angular) rotation rate (MTNΩ) using the slow system, the pure noise induced displacement signal in the sense direction is computed using equations (6.21)-(6.24). To this end, the angular rotation rate, Ω, and the excitation force, V_{AC}, are set to zero and the steady-state response in the sense direction under noise excitation is computed. Having found the noise response, the equations of pure signal, no noise input, that is equations (4.46) to (4.49), are solved for the angular rotation rate, Ω, and three other unknowns, that is a_q, η_1, and η_2.

The linear approximation of the noise equivalent rotation rate is computed from equation (6.16). Therefore, the nonlinear analysis is employed to identify the onset of multi-valuedness where an unstable branch appears in the response. The slow system including noise force is solved for pure noise response and the MTNΩ. On the other hand, for the same set of AC voltage, the linear MTNΩ is computed and compared with the result of nonlinear noise analysis. In practice, the linear analysis provides a reliable tool for MTN analysis and the optimization of the device for lower MTNΩ.

In Figures 6.2(a)-6.2(c), the MTNΩ is plotted versus the AC load. The respective quality factors are 400, 600, and 800 in the sense and drive directions. It is observed that the linear and nonlinear analysis are in excellent agreement while the nonlinear approximation is always larger than the linear one. It is noted that the MTNΩ is reduced with an increasing AC load. This presents the importance of operating at the highest possible AC voltage. On the other hand, increasing the quality factor has a positive effect on reducing MTNΩ.

In Table 6.1, the corresponding MTNΩ for the highest AC voltages for each set of results in Figures 6.2(a)-6.2(c). Therefore, it is recommended to design a system with higher quality factor considering the desired bandwidth, see equation (4.53). An approach to reduce the damping and increase the quality factor is to package the sensor in vacuum and reduce the effect of squeeze film damping. The higher the bandwidth is the lower the quality factor. The static deflection is decided by the DC loads and affects the MTNΩ, see equation (6.16). Figures 6.3(a)-6.3(c), present three matched-frequency cases.

In Table 6.2, the lowest MTNΩ for three cases of Figures 6.3(a)-6.3(c) are presented. It is seen that operating at higher DC voltages and therefore lower effective natural frequencies, increases MTNΩ. The conclusions are valid for any V_{AC}, that is design a system with lower damping, higher quality factor, and operating at the lower V_{DC} results in lower MTNΩ.

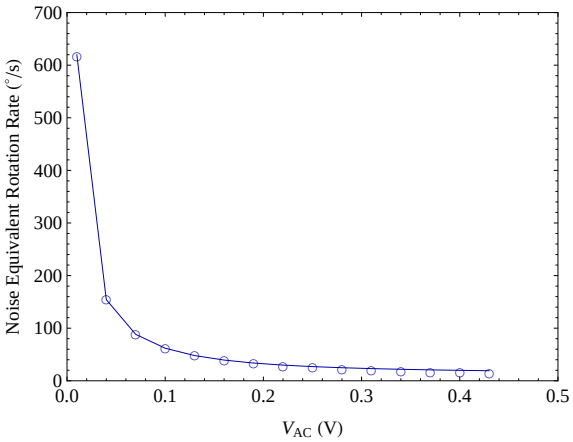

(a) $Q_D = 400$ and $Q_S = 400$

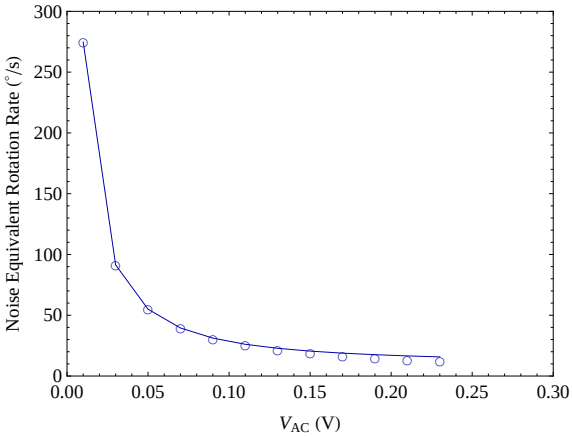

(b) $Q_D = 600$ and $Q_S = 600$

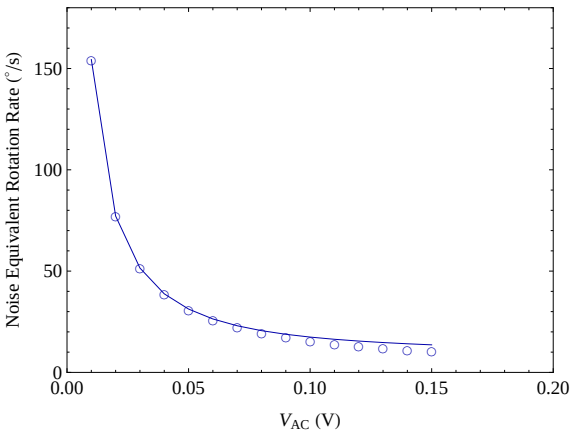

(c) $Q_D = 800$ and $Q_S = 800$

Figure 6.2: The noise equivalent (angular) rotation rate (MTNΩ) versus the AC voltage. The AC load is limited by the onset of multi-valuedness of the response. The solid line indicates the results of nonlinear slow system and the circles the linear analysis. The parameters include $V_w = 10.731$ V and $V_v = 3$ V.

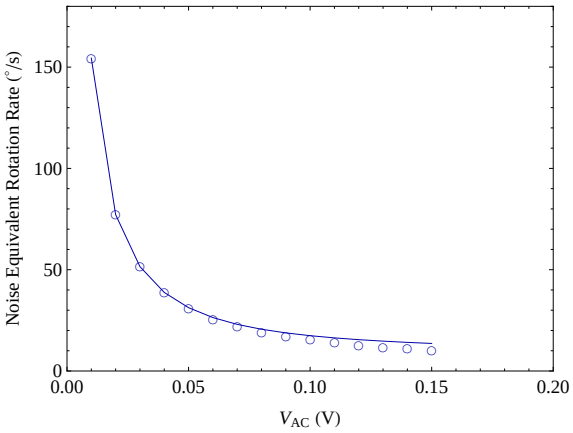

(a) $V_w = 10.731\,\text{V}$ and $V_v = 3\,\text{V}$

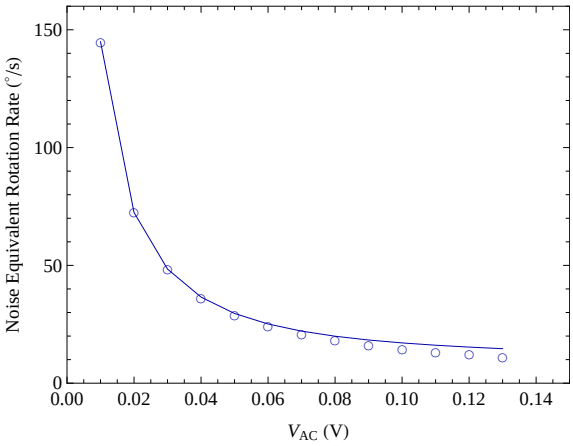

(b) $V_w = 11.400\,\text{V}$ and $V_v = 5\,\text{V}$

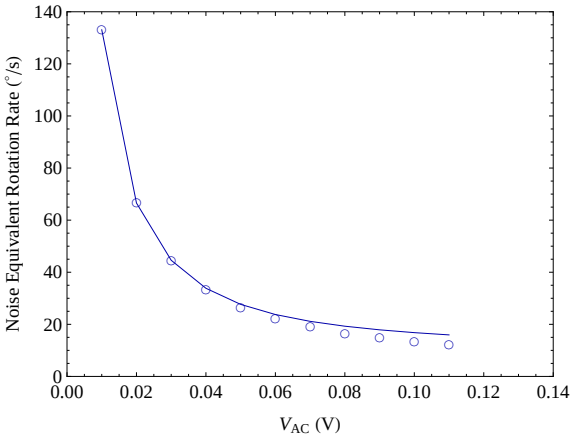

(c) $V_w = 12.335\,\text{V}$ and $V_v = 7\,\text{V}$

Figure 6.3: The noise equivalent (angular) rotation rate (MTNΩ) versus the AC voltage. The AC load is limited by the onset of multi-valuedness of the response. The solid line indicates the results of nonlinear slow system and the circles the linear analysis. The parameters include $Q_D = 800$ and $Q_S = 800$.

Table 6.1: Noise equivalent rotation rate (MTNΩ) for $V_w = 10.731\,\text{V}$, $V_v = 3\,\text{V}$

	$Q_S = 400$, $Q_D = 400$	$Q_S = 600$, $Q_D = 600$	$Q_S = 800$, $Q_D = 800$
V_{AC} (V)	0.43	0.23	0.15
MTNΩ (°/s) (Nonlinear analysis)	19.101	15.740	13.601
MTNΩ (°/s) (Linear analysis)	14.349	11.923	10.284

Table 6.2: Noise equivalent rotation rate (MTNΩ) for $Q_S = 800$, $Q_D = 800$

	$V_w = 10.731\,\text{V}$, $V_v = 3\,\text{V}$	$V_w = 11.400\,\text{V}$, $V_v = 5\,\text{V}$	$V_w = 12.335\,\text{V}$, $V_v = 7\,\text{V}$
V_{AC} (V)	0.15	0.13	0.11
MTNΩ (°/s) (Nonlinear analysis)	13.601	14.651	15.944
MTNΩ (°/s) (Linear analysis)	10.284	11.138	12.114

6.5 Summary

Due to the presence of damping, the mechanical-thermal (thermomechanical) noise appears in the system. For various applications, the resolution requirements differ from each other and thus amplify the importance of noise response. In this chapter, the thermal noise response of the system has been characterized in terms of noise equivalent rotation rate by using the linear approximation of system equations and the reduced-order nonlinear analysis of the system. It has been shown that in all cases, the linear and nonlinear approximations are in excellent agreement. The results suggest that the higher the quality factor is the lower the noise equivalent rotation rate. On the other hand, the operating static deflection position should be smaller for lower noise equivalent rotation rate. Therefore, for the given structure a combination of lower DC voltages, higher quality factor, and higher AC voltage results in the lowest noise equivalent rotation rate.

Chapter 7

Conclusions

7.1 The State of the Art

The thesis provides the necessary tools for the design and optimization of beam-rigid body gyroscope (rotation rate sensor). The systematic approach offers an invaluable method for the design of the new class of rotation rate senors in micro- and nano-scale. The new design and accurate model have not been reported in the literature. The dynamics and nonlinear dynamics of the beam carrying the large end rigid body have been extensively studied to provide the proper basis for the future research on the topic. In the following summary, the principal contributions of this thesis are highlighted and the prospects for future research are presented along with some recommendations for the design improvements.

7.2 Contributions of the Thesis

The major contributions of the thesis are as follows:

Chapter 2:

- The mathematical model of the cantilever beam carrying a rigid body is developed in Chapter 2. To derive the mathematical model, the kinetic energy of the structure under spatial rotation and deformation is computed. The kinetic energy associated with the end-rigid body modifies the total kinetic energy and the equations of motion.
- No assumption regarding the dimensions are made and the mathematical model is applicable to the micro/nano-sensors. The variations of the model including the beam-point mass model are presented. Furthermore, the model simplifies to the beam carrying an eccentric point mass by setting the rotary inertia matrix equal to zero.
- The common type of electrostatic actuation in the micro- and nano-systems is incorporated in

the mathematical model by computing the force at the center of mass and its corresponding moment at beam's free end. In the new form of the electrostatic force, the eccentricity, that is distance between beam's free end and the center of mass, appears in the nonlinear forcing term.

- The single-mode approximation of the mathematical model is established using the assumed-modes method. The reduced-order model is used for the reduced-order semi-analytical nonlinear analysis and the computational nonlinear analysis. The simplified forms of the reduced-order model are presented for the beam-point mass and beam-eccentric point mass systems.

Chapter 3:

- The static behaviour and the dynamic behaviour as seen through the modal frequencies of the system are studied in Chapter 3. It is shown that the reduced-order single-mode approximation agrees with the full-order partial differential equations of static motion.
- The static pull-in voltage is computed in the presence of angular rotation rate. The pull-in voltage for all practical purposes is not affected by the rotation rate.
- The modal frequencies of the gyroscope are determined. To this end, the characteristic equation is obtained and solved for the modal frequencies of the system in the rotating base frame.
- The application of the proposed system in the frequency-modulation mode is demonstrated by computing the input rotation rate as the function of the modal frequencies. In practice, the modal frequencies are measured and the rotation rate is computed from the equation.
- The effects of the end rigid body parameters, the eccentricity and the width of the body, on the frequency split are studied.
- The semi-modal frequencies in the inertial frame and the instability region by virtue of the rotation rate are calculated.

Chapter 4:

- The perturbation method, the method of multiple scales, is used to study the nonlinear behaviour of the second-order approximation of the system. The stability of the response is determined by computing the eigenvalues of the Jacobian matrix.
- The second order AC load and the second order rotation rate are discarded and the first order AC forcing, the Coriolis force, and the damping terms are scaled to appear in the third-order equations.

- The modulation equations in polar and Cartesian coordinates are computed. Detuning parameters describe the difference between the modal frequencies and the modal frequency and the excitation frequency.
- The frequency-response curves and the force-response curves are computed for various sets of DC loads.
- To compute the frequency-response plots, the excitation frequency is varied around the modal frequency by increasing and decreasing the excitation frequency and the steady-state amplitude is recorded for each excitation frequency.
- The possibility of operating the gyroscope in the frequency-modulation mode for forced vibration is demonstrated.
- It is shown that for matched-DC voltages in the drive and sense direction, the synchronization around the lower modal frequency is observed. Therefore, for large AC voltages the maximum response of the three branches appear at the common frequency.

Chapter 5:

- The nonlinear single-mode approximation is studied using the computational shooting method and the stability of the response is determined by computing the Floquet multipliers.
- The computational results are compared with the semi-analytical perturbation method and the range of validity of the reduced-order nonlinear analysis is determined. It is shown that for the cases of single-valued response, the perturbation method agrees with the computational shooting method.
- The steady-state trajectories of the response are determined for matched-frequency and matched-DC loads. The steady-state trajectory is a line or an ellipse depending on the load parameters.
- The global stability of the system response is determined by computing the separatrix trajectories and homoclinic path. Approximating the basin of attraction for an undamped-unforced system agrees with the damped-forced response.
- The cyclic-fold bifurcation points are obtained for various sets of parameters. The jump phenomena, the hysteresis, and the dynamic pull-in are characterized by long-time integration of the full system.

Chapter 6:

- The effects of mechanical-thermal (thermomechanical) noise on the beam-rigid body sensor are characterized.

- Two methods are used to characterize the mechanical-thermal noise effects and estimating the noise equivalent (angular) rotation rate: the linear analysis method and the nonlinear perturbation method.
- The noise equivalent rotation rate reduces with an increasing AC voltage.
- The higher the quality factor is the lower the noise equivalent rotation rate.
- Operating at higher DC voltages, increases the noise equivalent rotation rate.
- In all cases, the linear analysis results agree with the reduced-order nonlinear analysis results.

7.3 Recommendations for Future Work

As a result of this thesis, progress has been made toward the development of the new class of beam-based rotation rate sensors. At the same time, new questions have been raised. Some directions for further improvements of the system are provided here:

- The mathematical model is developed for a single-axis gyroscope. In practice more than one gyroscope are used to measure the rotation vector. The model should be extended to include all three rotation rate components.
- The axial and torsional deformations have been neglected in the current model. Additionally, the in-extensibility condition should be taken into consideration to develop a model including the geometric nonlinearities.
- The modal frequency split depends on the dimensions of the end rigid body as well as the beam. To operate the gyroscope in the frequency-modulation mode, the design should be optimized to maximize the frequency split and therefore increase the scale factor of the device.
- The sensitivity, mechanical scale factor, and shock resistance are other theoretical factors which need to be determined for the beam-rigid body gyroscope to design an optimum device. Therefore, it is recommended to characterize the aforementioned parameters using the linearized model following the same method as proposed for the mechanical-thermal noise in this thesis.
- One important damping mechanism in microsystems is the squeeze film damping. It is recommended to modify the design to reduce the effect of squeeze film damping. To this end, a hollow end rigid body could be used. The mathematical model remains unchanged except the mass and the rotary inertia matrix are adjusted.
- A finite element analysis of the structure may provide an insight to the performance and design of the micro/nano-sensor and result in a better design before going to the experimentation phase.

- The experimental verification of the results of this thesis would provide a basis for further improvement of the design and performance of the beam-based rotation rate sensors.

APPENDICES

Appendix A

List of Symbols

$(\mathbf{e}_\xi, \mathbf{e}_\eta, \mathbf{e}_\zeta)$	The unit vectors of the sectional coordinate system
$(\mathbf{e}_X, \mathbf{e}_Y, \mathbf{e}_Z)$	The unit vectors of the inertial coordinate system
$(\mathbf{e}_x, \mathbf{e}_y, \mathbf{e}_z)$	The unit vectors of the base-attached coordinate system
α	An aspect ratio constant $\alpha = \frac{b_B^2}{12L^2}$
Δ	The beam's cross sectional ratio, that is $\Delta = \frac{a_B}{b_B}$
δ	The internal detuning parameter: the difference between the two effective natural frequencies in the drive and sense directions, that is ω_q and ω_p
$\underset{B}{\mathcal{K}}$	The kinetic energy of the beam per unit length
$\underset{M}{\mathcal{K}}$	The kinetic energy of the end rigid body
$\underset{B}{\mathcal{P}}$	The elastic potential energy of the beam
$\underset{E}{\mathcal{P}}$	The electrostatic potential energy
$\underset{\mathfrak{F}_\mathfrak{a}}{\mathbf{R}_o}$	The position of the base frame relative to the inertial frame
$\underset{\mathfrak{F}_\mathfrak{b}}{\mathbf{R}_s}$	The position vector of the sectional frame relative to the base frame
$\underset{M}{J_{\eta\eta}}$	The mass moment of inertia of the end rigid body about the η axis
$\underset{M}{J_{\xi\xi}}$	The mass moment of inertia of the end rigid body about the ξ axis
$\underset{M}{J_{\zeta\zeta}}$	The mass moment of inertia of the end rigid body about the ζ axis

ϵ	The permittivity coefficient in units of Fm^{-1}
Γ	See equation (2.77) on page 28
Γ'	See equation (2.77) on page 28
Γ''	See equation (2.77) on page 28
κ	Time constant $\kappa = \sqrt{\frac{12\rho L^4}{E b^2}}$
Λ	See equation (2.77) on page 28
Λ'	See equation (2.77) on page 28
Λ''	See equation (2.77) on page 28
$\lambda_{1,1}$, $\lambda_{1,2}$	The fundamental modal frequencies of the gyroscope in the rotating frame
$\mathfrak{F}_\mathfrak{b}$	The base frame
$\mathfrak{F}_\mathfrak{s}$	The sectional frame
ν	The electrostatic constant $\nu = \frac{6\epsilon h L^4}{E b^4 g^3}$
Ω	The angular rotation rate about the x axis
ω_D	The natural frequency of the cantilever-rigid body in the drive direction ($V_w = 0$)
Ω_e	AC excitation frequency for the drive direction
ω_p	Effective natural frequency in the sense direction about the corresponding static equilibrium configuration
ω_q	Effective natural frequency in the drive direction about the corresponding static equilibrium configuration
ω_S	The natural frequency of the cantilever-rigid body in the sense direction ($V_v = 0$)
ω_v	The effective natural frequency, including the DC voltage, in the sense direction for uncoupled system ($\Omega = 0$)
ω_w	The effective natural frequency, including the DC voltage, in the drive direction for uncoupled system ($\Omega = 0$)
Ω_x	The angular rotation rate about the x axis
Ω_y	The angular rotation rate about the y axis
Ω_z	The angular rotation rate about the z axis

$\phi(\ell)$	The mode shape in the sense direction for a cantilever beam carrying an eccentric end rigid body ($V_v = 0$, $\Omega = 0$)
Π	See equation (2.77) on page 28
$\psi(\ell)$	The mode shape in the drive direction for a cantilever beam carrying an eccentric end rigid body ($V_w = 0$, $\Omega = 0$)
σ	The external detuning parameter: the difference between the excitation frequency and the effective natural frequency in the drive direction ω_q
a	The width of beam
a_M	The width of the end rigid body
A_v	The electrostatic forcing area for the sense electrode
A_w	The electrostatic forcing area for the drive electrode
b	The thickness of beam
b_M	The thickness of the end rigid body
BW	Bandwidth
E	Young's modulus
e	The eccentricity, that is the distance between the boundary of the cantilever beam and the center of mass of the end rigid body
g	The initial distance between the rigid body and each electrode ($g_w = g_v = g$)
g_v	The initial distance between the rigid body and the sense electrode
g_w	The initial distance between the rigid body and the drive electrode
h	The width of each electrode ($h_w = h_v = h$)
h_v	The width of the sense electrode
h_w	The width of the drive electrode
$I_{\eta\eta}$	Beam's cross sectional second moment of area about η
$I_{\zeta\zeta}$	Beam's cross sectional second moment of area about ζ
k_B	Boltzman constant
L	The length of beam

L_M	The length of the end rigid body
$p(t)$	Modal (generalized) coordinate for the sense direction
$p_d(t)$	Dynamic modal coordinate in sense direction ($p(t) = p_s + p_d(t)$)
p_s	Static modal coordinate in sense direction ($p(t) = p_s + p_d(t)$)
Q	Quality factor
$q(t)$	Modal (generalized) coordinate for the drive direction
Q_D	Quality factor for the drive direction
$q_d(t)$	Dynamic modal coordinate in drive direction ($q(t) = q_s + q_d(t)$)
Q_S	Quality factor for the sense direction
q_s	Static modal coordinate in drive direction ($q(t) = q_s + q_d(t)$)
T	Absolute temperature
$u(\ell, t)$	The axial displacement at an arbitrary section located at $x = \ell$ relative to the base frame in the x direction
$v(\ell, t)$	The flexural displacement at an arbitrary section located at $x = \ell$ relative to the base frame in the y
v_c	The nondimensional displacement at the center of rigid body in the sense direction ($v_c = v(1, t) + e\, v'(1, t)$)
$v_d(\ell, t)$	Dynamic flexural displacement in the sense direction about the static configuration ($v(\ell, t) = v_s(\ell) + v_d(\ell, t)$)
$v_s(1)$	Nondimensional static flexural displacement at beam's tip in the sense direction
$v_s(\ell)$	Static flexural displacement in the sense direction ($v(\ell, t) = v_s(\ell) + v_d(\ell, t)$)
V_v	DC voltage for the sense electrode
V_w	DC voltage for the drive electrode
V_{AC}	AC excitation amplitude for the drive direction
$w(\ell, t)$	The flexural displacement at an arbitrary section located at $x = \ell$ relative to the base frame in the z direction
w_c	The nondimensional displacement at the center of rigid body in the drive direction ($w_c = w(1, t) + e\, w'(1, t)$)

$w_d(\ell, t)$	Dynamic flexural displacement in the drive direction about the static configuration ($w(\ell, t) = w_s(\ell) + w_d(\ell, t)$)
$w_s(1)$	Nondimensional static flexural displacement at beam's tip in the drive direction
$w_s(\ell)$	Static flexural displacement in the drive direction ($w(\ell, t) = w_s(\ell) + w_d(\ell, t)$)
$J_{B^{\eta\eta}}$	The mass moment inertia of beam's cross section about η axis
$J_{B^{\xi\xi}}$	The mass moment inertia of beam's cross section about ξ axis
$J_{B^{\zeta\zeta}}$	The mass moment inertia of beam's cross section about ζ axis
MTNΩ (Ω_n)	Mechanical-thermal noise equivalent rotation rate

References

[1] Lanchester, F. W., 1903. "The pendulum accelerometer, an instrument for the direct measurement and recording of acceleration". *Proceedings of the Physical Society of London,* **19**(1), pp. 691–701.

[2] "Jean foucault". *Encyclopdia Britannica. Encyclopdia Britannica Online.* Retrieved 27 September, 2013, from http://www.britannica.com/EBchecked/topic/214675/Jean-Foucault.

[3] Reppich, A., and Willig, R., 1995. "Yaw rate sensor for vehicle dynamics control system". In Symposium Gyro Technology 1995, Stuttgart, Germany, pp. 67–76. SAE Paper 950537.

[4] Yazdi, N., Ayazi, F., and Najafi, K., 1998. "Micromachined inertial sensors". *Proceedings of the IEEE,* **86**(8), pp. 1640–1658.

[5] Groves, P. D., 2008. *Principles of GNSS, Inertial, and Multisensor Integrated Navigation Systems*. Artech House Remote Sensing Library. Artech House, Boston.

[6] Aszkler, C., 2005. "The principles of acceleration, shock, and vibration sensors". In *Sensor Technology Handbook*, J. S. Wilson, ed. Elsevier Inc., Oxford, pp. 137–159.

[7] Sethuramalingam, T. K., and Vimalajuliet, A., 2010. "Design of MEMS based capacitive accelerometer". In 2nd International Conference on Mechanical and Electrical Technology (ICMET), pp. 565–568. 10-12 September, Singapore.

[8] Bogue, R., 2013. "Recent developments in MEMS sensors: a review of applications, markets and technologies". *Sensor Review,* **33**(4), pp. 300–304.

[9] Ayazi, F., Faisal Zaman, M., and Sharma, A., 2008. "2.06 - vibrating gyroscopes". In *Comprehensive Microsystems*, Z. Hans, ed. Elsevier, Oxford, pp. 181–208.

[10] Armenise, M. N., Ciminelli, C., Dell'Olio, F., and Passaro, V. M. N., 2011. *Advances in Gyroscope Technologies*. Springer Berlin Heidelberg, Heidelberg.

[11] Allen, J. J., 2009. Micro-system inertial sensing technology overview. Tech. Rep. SAND2009-3080, Sandia National Laboratories.

[12] Tanaka, K., Mochida, Y., Sugimoto, M., Moriya, K., Hasegawa, T., Atsuchi, K., and Ohwada, K., 1995. "A micromachined vibrating gyroscope". *Sensors and Actuators A: Physical,* **50**(1-2), pp. 111–115.

[13] Mochida, Y., Tamura, M., and Ohwada, K., 2000. "A micromachined vibrating rate gyroscope with independent beams for the drive and detection modes". *Sensors and Actuators A: Physical,* **80**(2), pp. 170–178.

[14] Bernstein, J., Cho, S., King, A. T., Kourepenis, A., Maciel, P., and Weinberg, M., 1993. "A micromachined comb-drive tuning fork rate gyroscope". In Micro Electro Mechanical Systems, 1993, MEMS '93, Proceedings An Investigation of Micro Structures, Sensors, Actuators, Machines and Systems. IEEE., pp. 143–148. 7-10 February, Fort Lauderdale, FL.

[15] Hashimoto, M., Cabuz, C., Minami, K., and Esashi, M., 1995. "Silicon resonant angular rate sensor using electromagnetic excitation and capacitive detection". *Journal of Micromechanics and Microengineering,* **5**(3), p. 219.

[16] Ayazi, F., and Najafi, K., 2001. "A harpss polysilicon vibrating ring gyroscope". *Journal of Microelectromechanical Systems,* **10**(2), pp. 169–179.

[17] Yoon, S. W., Lee, S., and Najafi, K., 2011. "Vibration sensitivity analysis of mems vibratory ring gyroscopes". *Sensors and Actuators, A: Physical,* **171**(2), pp. 163–177.

[18] Antonello, R., and Oboe, R., 2011. "MEMS gyroscopes for consumer and industrial applications". In *Microsensors*, I. Minin, ed. InTech.

[19] O'Connor, J. M., and Shupe, D. M., 1983. Vibrating beam rotating sensor. U.S. Patent 4 381 672.

[20] Maenaka, K., Fujita, T., Konishi, Y., and Maeda, M., 1996. "Analysis of a highly sensitive silicon gyroscope with cantilever beam as vibrating mass". *Sensors and Actuators A: Physical,* **54**(1-3), pp. 568–573.

[21] Seok, J., and Scarton, H. A., 2006. "Dynamic characteristics of a beam angular-rate sensor". *International Journal of Mechanical Sciences,* **48**(1), pp. 11–20.

[22] Li, X., Bao, M., Yang, H., Shen, S., and Lu, D., 1999. "A micromachined piezoresistive angular rate sensor with a composite beam structure". *Sensors and Actuators A: Physical,* **72**(3), pp. 217–223.

[23] Esmaeili, M., Jalili, N., and Durali, M., 2007. "Dynamic modeling and performance evaluation of a vibrating beam microgyroscope under general support motion". *Journal of Sound and Vibration,* **301**(1-2), pp. 146–164.

[24] Bhadbhade, V., Jahli, N., and Mahmoodi, S. N., 2008. "A novel piezoelectrically actuated flexural/torsional vibrating beam gyroscope". *Journal of Sound and Vibration,* **311**(3-5), pp. 1305–1324.

[25] Mojahedi, M., Ahmadian, M. T., and Firoozbakhsh, K., 2013. "Static deflection and pull-in instability analysis of an electrostatically actuated mirocantilever gyroscope considering geometric nonlinearities". *Journal of Mechanical Science and Technology,* **27**(8), pp. 2425–2434.

[26] Rasekh, M., and Khadem, S. E., 2013. "Design and performance analysis of a nanogyroscope based on electrostatic actuation and capacitive sensing". *Journal of Sound and Vibration,* **332**(23), pp. 6155–6168.

[27] Lajimi, S. A. M., and Heppler, G. R., 2013. "Free vibration and buckling of cantilever beams under linearly varying axial load carrying an eccentric end rigid body". *Transactions of the Canadian Society for Mechanical Engineering,* **37**(1), pp. 89–109.

[28] Lajimi, S. A. M., and Heppler, G. R., 2012. "Eigenvalues of an axially loaded cantilever beam with an eccentric end rigid body". In International Conference on Mechanical Engineering and Mechatronics (ICMEM'12), pp. 135–1–135–8. 16-18 August, Ottawa, Canada.

[29] Lajimi, S. A. M., and Heppler, G. R., 2012. "Comments on "Natural frequencies of a uniform cantilever with a tip mass slender in the axial direction"". *Journal of Sound and Vibration,* **331**(12), pp. 2964–2968.

[30] Lajimi, A. M., Abdel-Rahman, E., and Heppler, G. R., 2009. "On natural frequencies and mode shapes of microbeams". In Proceedings of the International MultiConference of Engineers and Computer Scientists (IMECS), Vol. 2, pp. 2184–2188. 18-20 March, Hong Kong.

[31] Lajimi, S. A. M., Heppler, G. R., and Abdel-Rahman, E., 2013. "A new cantilever beam rigid-body MEMS gyroscope: mathematical model and linear dynamics". In 2nd International Conference on Mechanical Engineering and Mechatronics (ICMEM'13), pp. 177–1–177–6. 8-9 August, Toronto, Canada.

[32] Lajimi, S. A. M., 2013. "Analysis of nonlinear dynamics of a cantilever beam-rigid-body MEMS gyroscope using a continuation method". In 2nd International Conference on Mechanical Engineering and Mechatronics (ICMEM'13), pp. 179–1–179–5. 8-9 August, Toronto, Canada.

[33] Apostolyuk, V., 2006. "Theory and design of micromechanical vibratory gyroscopes". In *MEMS/NEMS Handbook Techniques and Applications*, C. T. Leondes, ed. Springer, New York, NY, pp. 173–195.

[34] Zaman, M. F., Sharma, A., Hao, Z., and Ayazi, F., 2008. "A mode-matched silicon-yaw tuning-fork gyroscope with subdegree-per-hour allan deviation bias instability". *Journal of Microelectromechanical Systems,* **17**(6), pp. 1526–1536.

[35] Friswell, M., Penny, J., Garvey, S., and Lees, A., 2010. *Dynamics of Rotating Machines*. Cambridge University Press, New York, NY, USA.

[36] Lajimi, S. A. M., Heppler, G. R., and Abdel-Rahman, E., 2013. "Eigenvalue analysis of a cantilever beam-rigid-body MEMS gyroscope". In 2nd International Conference on Mechanical Engineering and Mechatronics (ICMEM'13), pp. 178–1–178–5. 8-9 August, Toronto, Canada.

[37] Zotov, S. A., Prikhodko, I. P., Trusov, A. A., and Shkel, A. M., 2011. "Frequency modulation based angular rate sensor". In 2011 IEEE 24th International Conference on Micro Electro Mechanical Systems (MEMS), pp. 577–580. 23-27 January, Cancun.

[38] Zotov, S. A., Trusov, A. A., and Shkel, A. M., 2011. "Demonstration of a wide dynamic range angular rate sensor based on frequency modulation". In 2011 IEEE Sensors, pp. 149–152. 28-31 October, Limerick.

[39] Zotov, S. A., Trusov, A. A., and Shkel, A. M., 2012. "High-range angular rate sensor based on mechanical frequency modulation". *Journal of Microelectromechanical Systems,* **21**(2), pp. 398–405.

[40] Kline, M. H., Yeh, Y.-C., Eminoglu, B., Najar, H., Daneman, M., Horsley, D. A., and Boser, B. E., 2013. "Quadrature FM gyroscope". In 2013 IEEE 26th International Conference on Micro Electro Mechanical Systems (MEMS), IEEE, pp. 604–608. 20-24 January, Taipei.

[41] Prikhodko, I. P., Zotov, S. A., Trusov, A. A., and Shkel, A. M., 2012. "Foucault pendulum on a chip: Rate integrating silicon mems gyroscope". *Sensors and Actuators A: Physical,* **177**, pp. 67–78.

[42] Trusov, A. A., Prikhodko, I. P., Zotov, S. A., Schofield, A. R., and Shkel, A. M., 2010. "Ultra-high q silicon gyroscopes with interchangeable rate and whole angle modes of operation". In 2010 IEEE Sensors, IEEE, pp. 864–867.

[43] Trusov, A. A., Prikhodko, I. P., Zotov, S. A., and Shkel, A. M., 2012. "High-q and wide dynamic range inertial mems for north-finding and tracking applications". In 2012 IEEE/ION Position Location and Navigation Symposium (PLANS), IEEE, pp. 247–251. 23-26 April, Myrtle Beach, SC.

[44] Hofler, T. J., and Garrett, S. L., 1988. "Thermal noise in a fiber optic sensor". *The Journal of the Acoustical Society of America,* **84**, p. 471.

[45] Gabrielson, T. B., 1993. "Mechanical-thermal noise in micromachined acoustic and vibration sensors". *IEEE Transactions on Electron Devices,* **40**(5), pp. 903–909.

[46] Annovazzi-Lodi, V., and Merlo, S., 1999. "Mechanicalthermal noise in micromachined gyros". *Microelectronics Journal,* **30**(12), pp. 1227–1230.

[47] Senturia, S. D., 2001. *Microsystem Design*. Kluwer Academic Publishers, Boston.

[48] Bao, M.-H., 2000. *Micro mechanical transducers: pressure sensors, accelerometers and gyroscopes*, Vol. 8. Elsevier B. V., Amsterdam.

[49] Leland, R. P., 2005. "Mechanical-thermal noise in mems gyroscopes". *Sensors Journal, IEEE,* **5**(3), pp. 493–500.

[50] Lynch, D. "Vibratory gyro analysis by the method of averaging". In Proc. 2nd St. Petersburg Conf. on Gyroscopic Technology and Navigation, St. Petersburg, pp. 26–34. St. Petersburg.

[51] Meirovitch, L., 1997. *Principles and Techniques of Vibrations*. Prentice-Hall, Inc., Upper Saddle River, New Jersey.

[52] Meirovitch, L., 2001. *Fundamentals of Vibrations*. Waveland Press, Inc., Long Grove, IL.

[53] Meirovitch, L., 1980. *Computational Methods in Structural Dynamics*. Sijthoff & Noordhoff, Rockville, Maryland.

[54] Strogatz, S. H., 1994. *Nonlinear Dynamics And Chaos: With Applications To Physics, Biology, Chemistry, And Engineering*. Perseus Books Publishing, LLC, Cambridge, MA.

[55] Lamb, K., 2009. Course notes for AMATH 732: Asymptotic analysis and perturbation theory. University of Waterloo.

[56] Bender, C. M., and Orszag, S. A., 1978. *Advanced mathematical methods for scientists and engineers*. McGraw-Hill, Inc., New York.

[57] Jordan, D. W., and Smith, P., 2007. *Nonlinear Ordinary Differential Equations*, 4th ed. Oxford University Press, Inc., New York.

[58] Seydel, R., 1988. *From equilibrium to chaos: practical bifurcation and stability analysis*. Elsevier, New York.

[59] Parker, T. S., and Chua, L. O., 1989. *Practical numerical algorithms for chaotic systems*. Springer-Verlag New York, Inc., New York, NY.

[60] Sracic, M. W., and Allen, M. S., 2011. "Numerical continuation of periodic orbits for harmonically forced nonlinear systems". In *Civil Engineering Topics*, T. Proulx, ed., Vol. 4. Springer, New York, pp. 51–69.

[61] Butenin, N. V., 1965. *Elements of the Theory of Nonlinear Oscillations*. Blaisdell Publishing Company, A Division of Ginn and Company, New York, Toronto, London.

[62] Minorsky, N., 1962. *Nonlinear Oscillations*. D. Van Nostrand Company, Inc., Princeton, NJ.

[63] Mihajlovic, N., 2002. Literature study on periodic solutions in nonlinear dynamic systems. Tech. rep., Eindhoven University of Technology, Department of Mechanical Engineering. Report No. DCT 2002.59.